ABSTRACT

Title of dissertation: Low Temperature Scanning Tunneling Microscopy and Spectroscopy: A Study On Charge Density Waves and Vortex Dynamics

Hui Wang, Doctor of Philosophy, 2009

Dissertation directed by: Professor Ellen D. Williams
Department of Physics

In this thesis I describe the development of a low temperature scanning tunneling microscope system (LTSTM) and its application to the study of charge density waves and vortex dynamics. All the measurements are taken on different 2H-$NbSe_2$ samples with or without impurities to examine the interesting coexistence of the charge density wave (CDW) phase and superconductive phase in the sample at 4.2 K. After creating a structural defect using a voltage pulse, we observed a new type of CDW in the vicinity of the defect. With a $\sqrt{13} \times \sqrt{13}$ reconstruction , the new CDW differs in many ways from the naturally occurring 3×3 CDW in 2H-$NbSe_2$. This suggests a possible local phase transition induced by the tip-sample interaction. As a low-T_c type II superconductor, 2H-$NbSe_2$ is also well-known for the formation of a vortex phase in magnetic fields. Although it was intensely studied for decades, many questions concerning the vortex system still remain unanswered. One of the most important and intriguing questions is the response of the system to a driving force well below the critical value f_c. Due to an unexpected defect in our magnet, we

are able to utilize a slowly decaying magnetic field with a rate at $\sim$ nT/s to observe the dynamic creep motion of the vortex system which can be described as a Bragg glass. I will also present a study of the statics of this glass phase and demonstrate the use of LTSTM as a powerful imaging technique in the area of vortex physics.

LOW TEMPERATURE SCANNING TUNNELING MICROSCOPY AND SPECTROSCOPY: A STUDY ON CHARGE DENSITY WAVES AND VORTEX DYNAMICS

by

Hui Wang

Dissertation submitted to the Faculty of the Graduate School of the
University of Maryland, College Park in partial fulfillment
of the requirements for the degree of
Doctor of Philosophy
2009

Advisory Committee:
Professor Ellen D. Williams, Chair/Advisor
Dr. Barry I. Barker, Co-Advisor
Professor Christopher J. Lobb
Professor James R. Anderson
Professor Romel D. Gomez

Dedication

To Bo Wang, my brother,

Huiling Cao, my mother, & Fuqiang Wang, my father

Acknowledgments

First and foremost, I would like to thank my advisor, Barry Barker, for giving me such an invaluable opportunity to work on all these challenging and interesting projects over the past several years, especially to build the low temperature STM system from scratch. I learned almost everything about low temperature scanning tunneling microscopy from him. He has always made himself available for help and advice. It has been a great pleasure to work with and learn from such an extraordinary individual.

I would also like to thank my colleague Michael Dreyer for helping me with the PV-Wave programming and the operation of UHV systems as well as countless other questions. He also developed the software SXD based on PV-Wave which I used to analyze STM images and STS spectra. Some of them are included in this thesis. His exceptional expertise in software programming and experimental techniques always inspires me to learn more.

Thanks to Jonghee Lee who worked together with me for all these years in this two-men trench. He has been like a brother to me. I learned a lot from him through numerous discussions about physics as well as life experiences. He is an example of hard working physicists with great passion to make progress. All the beautiful data in this thesis were taken with the STM head assembled by him. He also went through with me all the tough times in testing and troubleshooting the system. Without him, this thesis would not have been possible. I sincerely thank him for his collaboration and friendship.

Many Thanks to members of the committee: Ellen Williams, Barry Barker, Chris Lobb, Bob Anderson, and Romel Gomez for agreeing on serving on my thesis committee and spending their precious time reviewing the manuscript. Special thanks to Chris Lobb for his constant help and inspirations in the effort to understand the vortex motion puzzle with us. Thanks to my co-advisor Ellen Williams for her kind support. I also want to thank Danilo Romero at LPS and Eva Andrei at Rutgers University for providing us the $NbSe_2$ samples and for their support to our project. Additionally, I want to acknowledge all the help from the LPS machine shop and electronic shop during the construction phase of our lab.

I am blessed with wonderful friends who enriched my life in graduate school. Thanks to Lixin Wang and Huaqiang Ma who are always supportive and sincere to me. Thanks to friends at LPS who shared their stories and laughters with me, among them are Luyan Sun, Lei He, Konrad Aschenbach, Taesoon Kwon, Jookyung Lee, Hanhee Paik, Dan Sullivan, Mark Gubrud and Anita Roychowdhury.

Finally I owe my deepest thanks to my family. My mother, father and my dear brother always stood by me and gave me all they can whenever I need it. Their love is the ultimate resource I rely on to pull through anything in life that seemed impossible initially. I dedicate this thesis to them.

Table of Contents

List of Figures

List of Abbreviations

α	alpha
β	beta
CDW	Charge Density Waves
STM	Scanning Tunneling Microscopy
LTSTM	Low Temperature Scanning Tunneling Microscopy
UHV	Ultra High Vacuum
LHe	Liquid Helium
DOS	Density of States
LPS	Laboratory for Physical Sciences
LDOS	Local Density of States
STS	Scanning Tunneling Spectroscopy
TSP	Titanium Sublimation Pump
IGP	Ion Getter Pump
OFHC	Oxygen Free High Conductivity
SC	Superconducting
FS	Fermi Surface
PSD	Periodic Structural Displacement
VL	Vortex Lattice
FLL	Flux Line Lattice
HTSC	Hight T_c Superconductor
LO	Larkin and Ovchinikov
TAFF	Thermally Assisted Flux Flow
ZFC	Zero Field Cooled
FC	Field Cooled

Chapter 1

Introduction

All the results presented in this thesis were obtained on 2H-$NbSe_2$ single crystals which were cleaved in high vacuum ($\sim 10^{-8}$ mbar) and subsequently studied in cryogenic ultrahigh vacuum (UHV) at 4.2 K using a scanning tunneling microscope (STM). Our home built STM system operates, with high spatial and energy resolution, at low temperatures (≤ 4.2 K) and in magnetic fields up to 9.1 T. The system consists of a compact and rigid STM head, mounted directly to a 4 K probe and a UHV preparation chamber. The probe was designed with minimum thermal mass so we are able to run the system continuously for 7 days without interruption by liquid helium (LHe) transfer. The system is equipped with a sample transport manipulator from room temperature and sample storage space in the preparation UHV chamber. This enables us to exchange samples between the room temperature UHV and the cryogenic UHV inside the probe and re-sharpen our tip when it's necessary. A superconducting magnet provides a field of up to 9.1 T at the sample along the STM tip direction. All the experiments described in this thesis used magnetic fields up to 1 T.

The thesis is organized as follows: In Chapter 2, I will present an introduction to the theoretical and experimental aspects of STM in general and the design and development of our ultra-high vacuum, low temperature STM system. In Chapter 3,

I will discuss the properties of the material we mainly used in this thesis, 2H-$NbSe_2$, along with the studies on it by our STM. This chapter serves as an example of the operating modes of our STM introduced in Chapter 2 as well as a preparation for the more specific topics in Chapter 4 and Chapter 5. Chapter 4 is a report on our observation of a new type of charge density waves in the vicinity of structural defects created by sending voltage pulses or jumps to the tip during scanning. The interesting features of the new CDW are compared with the natural, pre-existing one in the material and possible explanations are discussed. Instead of imaging atoms on the sample surface as in Chapter 4, Chapter 5 deals with a different kind of lattice structure, the vortex lattice. A unique property of the vortex lattice is that the lattice constant can change under the influence of external forces. Thus one would expect different physics in the vortex matter. Indeed, even after decades of study, there are still many open questions about the static and dynamic properties of it due to the complex nature of the interaction between the system and disorder [1, 2]. After introducing the background and the theoretical description of vortex matter, I will demonstrate the use of our STM as a powerful tool to investigate the statics and dynamics of the system. Advantages and limitations of this technique will be discussed. Due to an unexpected defect in our magnet, we were able to directly observe the dynamic creep motion of the system. To the best of my knowledge, the motion is the slowest ever detected and our observation is the longest. It is the first time the detailed nature of this motion has been directly revealed. Discussions of the results and comparison with theory will be presented.

Chapter 2

A Low Temperature Scanning Tunneling Microscope: Its Principles, Design and Operation

2.1 Background

STM has been one of the revolutionary innovations in the past century that left a profound impact on condensed matter physics especially in the area of surface science [3]. Since its the invention in 1981 by Binnig and Rohrer [4], several generations of STMs have been developed. In the last two decades, STM has become one of the most powerful and indispensable tools in the study of physics at nano-scale through constant improvement and sophistication of the technology. Many commercial products are available, but the best instruments are often built in house for the specific applications and performance requirements.

Our group is particularly interested in developing a microscope that can operate at low temperatures with high spatial resolution and high energy resolution as well as versatile sample preparation capabilities. Our purpose is to study nano-scale physics of semiconductors and superconductors on a variety of samples. At low temperatures, we gain automatically the benefits of low thermal noise, low thermal drift and cryogenic UHV conditions which are three crucial conditions for superb STM operations. Two additional important conditions are the quality of the sample

surface and the quality of tip. In practice, we spend a lot of time to achieve these two stringent requirements. Our system was designed to meet the challenge of high resolution for the study of microscopic structures of complex electronic systems.

The purpose of this chapter is to provide an introduction of the theoretical and experimental aspects of STM. After an overview of the whole system, I will present a full treatment of the theory of an equilibrium model which proved to be very effective in describing the tunneling physics in STM. The result will help understand the description of the operational modes of STM, the interpretation of the measurements we can make with it, and also the challenges we face in design and operation of the system. Later in this chapter, I will give a thorough description of our design and how we developed our system to meet these technical challenges.

2.2 Basic Principles of STM

The physical phenomenon behind scanning tunneling microscopy is quantum tunneling of electrons between two electrodes through a thin potential barrier. This phenomenon has been known since the early days of quantum mechanics and it was the topic of many textbooks of quantum mechanics to introduce the physics dictated by the Schödinger equations with simple boundary conditions. Many experiments were carried out with planar junctions that can be described by a simple one-dimensional (1D) model [5]. Apparently, no spatially resolved tunneling was possible in these rigid electrode configurations. In 1981, Binnig and Rohrer developed the scanning tunneling microscope. Their revolutionary idea was to have one

side of the electrodes movable and the gap between the two controllable so it's thin enough to allow measurable current to flow. Secondly, they used a sharp metallic tip as the movable electrode mounted on a three dimensional piezoelectric drive. By combining the effects of the atomically sharp tip and the picometer accuracy of the piezoelectric actuators, the spatial resolution was increased to the atomic level. This remarkable achievement won them the Nobel prize in 1986 [6].

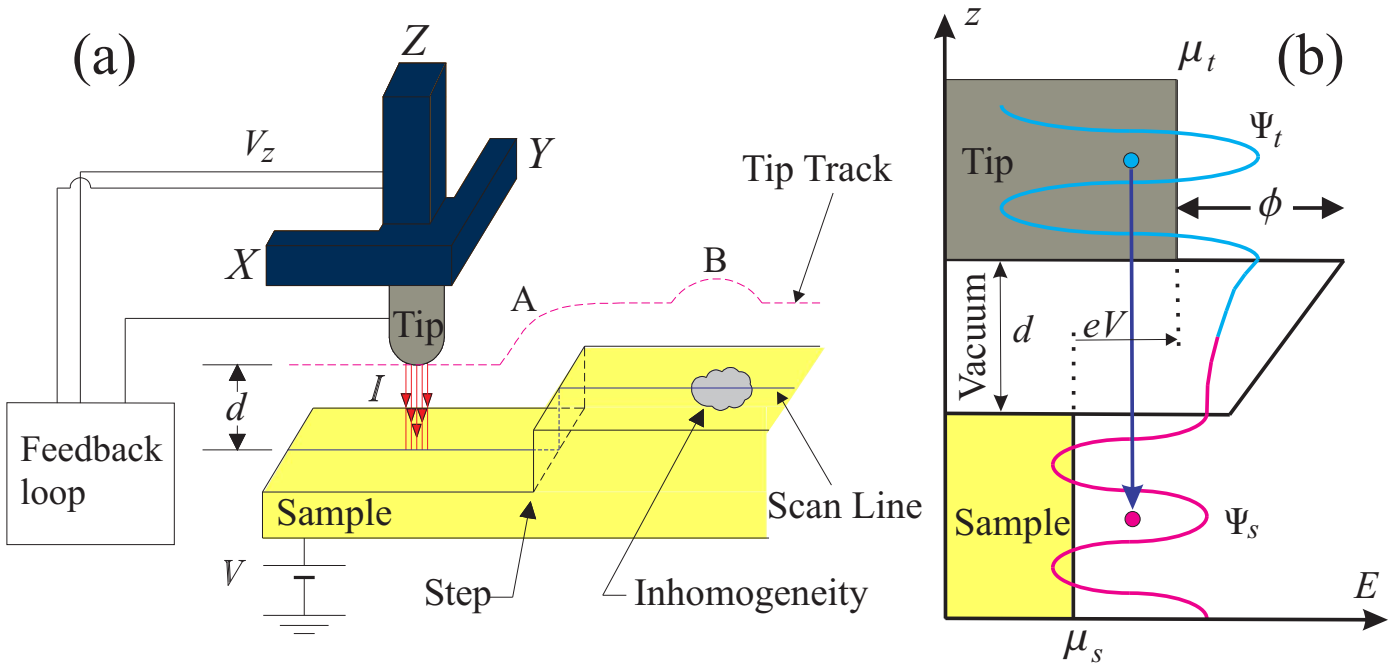

Figure 2.1: **Tunneling Physics in STM.** (a) A schematic model of STM. A bias voltage V on the sample results in a measurable current I across the vacuum junction between the tip end and the sample surface atoms with a distance d. (b) The tunneling process. As the bias voltage maintains a difference of Fermi energies μ_t and μ_s at eV, an electron from an occupied state in the tip tunnels to an empty state in the sample of the same energy. The theoretical calculations are described in Sec. 2.3.

Figure 2.1(a) shows a schematic model of a STM. The tip is scanned in the x-y plane above the sample using the X and Y actuators, while its height is controlled using the Z actuator. Applying a bias voltage, V, between the metallic tip and conducting sample and approaching the tip within a few angstroms of the sample surface results in a measurable tunneling current, I. An electronic feedback loop is used to maintain this current by continuously adjusting the tip height. The most striking feature of this instrument is the remarkable spatial resolution it can achieve. The key for reaching a vertical resolution of a few hundredths of an angstrom is the exponential dependence of the tunneling current I on the tip-to-sample distance d (in Å):

$$I \propto e^{-2\kappa d},\ \kappa = \frac{\sqrt{2m\phi}}{\hbar} \approx 0.513\sqrt{\phi}. \tag{2.1}$$

Here κ is the decay constant of the tunneling electrons in the barrier region and ϕ (in eV) is the work function of the sample. For a typical metal, $\phi \approx 5$ eV. From Eq. 2.1, the current I will decrease $e^{2.292} \approx 9.9$ times, *i.e.* an order of magnitude, for every increase of d by 1 Å. This high sensitivity of I vs. d enables a STM to resolve the atomic corrugation of the sample surface. The lateral resolution mainly depends on the apex geometry and electronic orbit of the scanning tip, which confine the tunneling electrons into a narrow channel, offering the unique opportunity to perform real-space imaging down to atomic length scales. Section 2.3 provides a more detailed discussion of the theoretical aspects of the tunneling physics in this model.

In practice, typical settings of tunneling parameters are: tunneling current

$I \sim 0.01 - 10$ nA, bias voltage $V \sim 0.001 - 10$ V. The tunneling resistance $R_t = V/I$ is usually set to be $\sim$ GΩ. The tip-to-sample spacing d is typically $5 - 10$ Å. The tunneling current is actually the convolution of the electron density of states of both the tip and the sample. This enables the use of STM to study the electronic properties of the sample. It's preferable to use tips with a featureless density of states (ideally constant) and a well-defined Fermi surface (ideally spherical). The metals most commonly used for the tip are Au, W, Ir and PtIr. In our lab, we used mechanically cut W tips, PtIr tips and chemically etched W tips. The tip preparation method will be discussed in Chapter 3.

2.3 Theory of STM

In this section, I provide a full treatment of the theory regarding the electron tunneling in the STM system. We are mainly interested in the connection between the measurable parameters and the meaningful physical properties of the sample.

2.3.1 Tunneling Theory of an Equilibrium Model

The tunneling Hamiltonian formalism was proposed by Bardeen [5]. It provides a framework to understand both single-particle and pair tunneling phenomena [7]. In this formalism, we consider a physical system consisting of two independent parts and a potential barrier in between as illustrated in Fig. 2.1. The electron tunnels from the tip to the sample under the influence of the bias voltage V across the gap. The state of the electron on the left is denoted as φ_μ and on the right

φ_ν. They are assumed to be the eigenstates of the Hamiltonian H_s and H_t for the sample and the tip, respectively. The real space states of the two sides are denoted as ψ_S and ψ_t in Fig. 2.1 (also see Eq. 2.5). The basic assumptions of this formalism are: 1) the tunneling process is an equilibrium process, 2) the correlation between the two parts can be neglected, 3) the elementary process involved is only single electron tunneling, 4) the tip and the sample have the same work function.

The assumptions 1)-3) can be justified in STM case because the magnitude of the current is so low that the time between two tunneling events ($\sim 10^{-10}$ s) is much longer than the relaxation time of the typical quasi-particles ($\sim 10^{-13}$ s) in both systems. 4) is assumed for the convenience of calculation. The phenomenological tunneling hamiltonian H_T can be written as:

$$H_T = \sum_{\mu\nu} T_{\mu\nu} a_\nu^\dagger b_\mu + c.c.. \tag{2.2}$$

Here $a_\nu^\dagger$ is the operator of creating one particle in the sample and b_μ is that for destroying one electron in the tip. From the assumptions of this model all the operators on the sample side commute with the ones on the tip side. $T_{\mu\nu}$ is the tunneling matrix for one electron from the tip to the sample. In our case, it's more convenient to work in real space. The full Hamiltonian of the system in the Schödinger picture:

$$H = H_s + H_t + H_T = H_0 + H_T. \tag{2.3}$$

Here H_s and H_t are the Hamiltonians of the sample and tip, respectively. In real

space, H_T can be rewritten as:

$$H_T = \chi + \chi^\dagger,\ \chi = \int d\mathbf{r}_1 d\mathbf{r}_2 T(\mathbf{r}_2, \mathbf{r}_1)\psi_s^\dagger(\mathbf{r}_1)\psi_t(\mathbf{r}_2). \tag{2.4}$$

$\psi_s^\dagger(\mathbf{r}_1)$ create an electron in the sample at $\mathbf{r}_1$ and $\psi_t(\mathbf{r}_2)$ destroys one electron in the tip at $\mathbf{r}_2$. $T(\mathbf{r}_2, \mathbf{r}_1)$ is the real space tunneling matrix element for an electron in the tip at $\mathbf{r}_2$ to tunnel to the sample at $\mathbf{r}_1$. They are related to the state space representation by:

$$\psi_s(\mathbf{r}_1) = \sum_\nu \varphi_\nu(\mathbf{r}_1)a_\nu,\ \psi_t(\mathbf{r}_2) = \sum_\mu \varphi_\mu(\mathbf{r}_2)b_\mu,\ T(\mathbf{r}_2, \mathbf{r}_1) = \sum_{\mu\nu} \varphi_\mu^*(\mathbf{r}_2)T_{\mu\nu}\varphi_\nu(\mathbf{r}_1). \tag{2.5}$$

Following Mahan [8], in the Heisenberg picture the tunneling current is given by the rate of change of number of electrons:

$$I = \mathbf{Tr}[\rho j] = \langle j \rangle = e\left\langle \dot{N}_s \right\rangle. \tag{2.6}$$

ρ is the full density matrix of the interacting system, e is the magnitude of the electron charge, N_s is the number operator of electrons. $j = e\dot{N}_s$ is the current operator. The current I is by convention positive when the electrons flow from the tip to the sample. By the assumption of the conservation of total number of particles in the sample system and the commutation rules, $i\dot{N}_s = [N_s, H] = [N_s, H_T] = [N_s, \chi] + [N_s, \chi^\dagger]$, where:

$$\begin{aligned}
[N_s, \chi] &= [\int d\mathbf{r}\psi_s^\dagger(\mathbf{r})\psi_s(\mathbf{r}), \int d\mathbf{r}_1 d\mathbf{r}_2 T(\mathbf{r}_2, \mathbf{r}_1)\psi_s^\dagger(\mathbf{r}_1)\psi_t(\mathbf{r}_2)] \\
&= \int d\mathbf{r}_1 d\mathbf{r}_2 d\mathbf{r} T(\mathbf{r}_2, \mathbf{r}_1)\psi_s^\dagger(\mathbf{r})[\psi_s(\mathbf{r}), \psi_s^\dagger(\mathbf{r}_1)]_+\psi_t(\mathbf{r}_2) \\
&= \int d\mathbf{r}_1 d\mathbf{r}_2 d\mathbf{r} T(\mathbf{r}_2, \mathbf{r}_1)\psi_s^\dagger(\mathbf{r})\delta^{(3)}(\mathbf{r} - \mathbf{r_1})\psi_t(\mathbf{r}_2) = \chi,
\end{aligned} \tag{2.7}$$

and similarly $[N_s, \chi^\dagger] = -\chi^\dagger$ (in units $\hbar = 1$, $[,]_+$ denotes the Fermi commutator). Thus $i\dot{N}_s = \chi - \chi^\dagger$. Now let's switch to the interaction picture to find out the thermal average of the current at time t. Following Mahan [8] (p214), considering only the linear response term:

$$I(t) = \langle j(t) \rangle = -i\mathbf{Tr}\left\{ \int_{-\infty}^{\mathbf{t}} dt' \rho_0 [j(t), H_T(t')] \right\} \tag{2.8}$$

$$= -i \int_{-\infty}^{t} dt' \left\langle [j(t), H_T(t')] \right\rangle_0 . \tag{2.9}$$

Here $\rho_0 = e^{\beta(\Omega - H_0 + \mu N)} = e^{\beta(\Omega - H_s - H_t + \mu_s N_s + \mu_t N_t)}$ is the density matrix of the non-interacting system, $j(t) = e^{iH_0 t}(e\dot{N}_s)e^{-iH_0 t}$, $H_T(t') = e^{iH_0 t'} H_T e^{-iH_0 t'}$, $\beta = 1/k_B T$. Using Eq. 2.4, 2.6 and 2.7, it follows that:

$$\begin{aligned}
I(t) &= -i \int_{-\infty}^{t} dt' e \left\langle [\dot{N}_s(t), H_T(t')] \right\rangle_0 = -ie \int_{-\infty}^{+\infty} dt' \theta(t - t') \left\langle [\dot{N}_s(t), H_T(t')] \right\rangle_0 \\
&= -e \int_{-\infty}^{+\infty} dt' \theta(t - t') \left\langle [\chi(t) - \chi^\dagger(t), \chi(t') + \chi^\dagger(t')] \right\rangle_0 \\
&= -e \int_{-\infty}^{+\infty} dt' \theta(t - t') 2iIm \left\langle [\chi(t), \chi^\dagger(t')] \right\rangle_0 \\
&\quad -e \int_{-\infty}^{+\infty} dt' \theta(t - t') 2iIm \left\langle [\chi(t), \chi(t')] \right\rangle_0 \\
&= I_s(t) + I_J(t),
\end{aligned} \tag{2.10}$$

with $I_s(t)$ being the single particle current and $I_J(t)$ the pair (Josephson) current. Here $\chi(t) = e^{iH_0 t}\chi e^{-iH_0 t}$. In calculating the correlation functions it is convenient to introduce the operator $K = H_0 - \mu N = H_s + H_t - \mu_s N_s - \mu_t N_t$ and the retarded Green's functions. Recalling $[N_s, \chi] = \chi$, $[N_s, \chi^\dagger] = -\chi^\dagger$ and similarly $[N_t, \chi] = -\chi$, $[N_t, \chi^\dagger] = +\chi^\dagger$, also noticing $[K, N_s] = [K, N_t] = 0$, we can write:

$$\begin{aligned}
\chi(t) &= e^{iH_0 t}\chi e^{-iH_0 t} = e^{i(K+\mu N)t}\chi e^{-i(K+\mu N)t} = e^{iKt}(e^{i\mu N t}\chi e^{-i\mu N t})e^{-iKt} \\
&= e^{iKt}[e^{i\mu_s N_s t}(e^{i\mu_t N_t t}\chi e^{-i\mu_t N_t t})e^{-i\mu_s N_s t}]e^{-iKt}
\end{aligned}$$

$$
\begin{aligned}
&= e^{iKt}[e^{i\mu_s N_s t}(\chi + i\mu_t t[N_t,\chi] + \frac{(i\mu_t t)^2}{2}[N_t,[N_t,\chi]] + ...)e^{-i\mu_s N_s t}]e^{-iKt} \\
&= e^{iKt}[e^{i\mu_s N_s t}(e^{-i\mu_t t}\chi)e^{-i\mu_s N_s t}]e^{-iKt} = e^{iKt}[e^{i\mu_s t}(e^{-i\mu_t t}\chi)]e^{-iKt} \\
&= e^{-ieVt}(e^{iKt}\chi e^{-iKt}) = e^{-ieVt}\chi_t. \qquad (2.11)
\end{aligned}
$$

Here $eV = \mu_t - \mu_s$, and V is the bias voltage. The retarded Green's function [8] for operator χ and its Fourier transform are defined as:

$$
\begin{aligned}
\overline{\chi}_{ret}(t-t') &= -i\theta(t-t')\left\langle[\chi_t, \chi^\dagger_{t'}]\right\rangle_0 \\
\overline{\chi}_{ret}(\omega) &= \int_{-\infty}^{+\infty} dt e^{i\omega t}\overline{\chi}_{ret}(t). \qquad (2.12)
\end{aligned}
$$

The current $I_s(t)$ can now be represented as:

$$
\begin{aligned}
I_s(t) &= 2e\mathrm{Im}\int_{-\infty}^{+\infty} \mathrm{dt'(-i)}\theta(\mathrm{t-t'})\mathrm{e}^{-\mathrm{ieV(t-t')}}\left\langle[\chi_\mathrm{t}, \chi^\dagger_{\mathrm{t'}}]\right\rangle_0 \\
&= 2e\mathrm{Im}\int_{-\infty}^{+\infty} \mathrm{dt'e}^{-\mathrm{ieV(t-t')}}\overline{\chi}_{\mathrm{ret}}(\mathrm{t-t'}) \\
&= 2e\mathrm{Im}\overline{\chi}_{\mathrm{ret}}(-\mathrm{eV}). \qquad (2.13)
\end{aligned}
$$

The Matsubara functions for χ are:

$$
\begin{aligned}
\chi^M(\tau) &= -\left\langle T_\tau \chi_\tau \chi^\dagger_0\right\rangle_0, \\
\chi^M(i\Omega_n) &= \int_0^\beta d\tau e^{i\Omega_n \tau}\chi^M(\tau). \qquad (2.14)
\end{aligned}
$$

χ_τ here is defined as $e^{K\tau}\chi e^{-K\tau}$, and $\chi^\dagger_\tau = e^{K\tau}\chi^\dagger_\tau e^{-K\tau}$. T_τ is the ordering operator. $\Omega_n = \frac{2n\pi}{\beta}$ since χ is a bosonic operator. The idea here is that it's much easier to calculate $\chi^M(i\Omega_n)$ and then take an analytic continuation:

$$
\chi^M(i\Omega_n \to \omega + i\delta) = \overline{\chi}_{ret}(\omega) \qquad (2.15)
$$

than to directly calculate $\overline{\chi}_{ret}(\omega)$. $\chi^M(i\Omega_n)$ can be related to the temperature Green's functions of the electrons from the sample and the tip:

$$\begin{aligned} G^M_{s,t}(\mathbf{r}_1,\mathbf{r}_2,\tau) &= -\left\langle T_\tau \psi_{s,t}(\mathbf{r}_1,\tau)\psi^\dagger_{s,t}(\mathbf{r}_2,0)]\right\rangle_0, \\ G^M_{s,t}(\mathbf{r}_1,\mathbf{r}_2,i\omega_n) &= \int_0^\beta d\tau e^{i\omega_n\tau} G^M_{s,t}(\mathbf{r}_1,\mathbf{r}_2,\tau), \\ G^M_{s,t}(\mathbf{r}_1,\mathbf{r}_2,\tau) &= \frac{1}{\beta}\sum_n e^{-i\omega_n\tau} G^M_{s,t}(\mathbf{r}_1,\mathbf{r}_2,i\omega_n) \end{aligned} \tag{2.16}$$

and their Lehmann representations by the spectral functions (see [9] p297):

$$G^M_{s,t}(\mathbf{r}_1,\mathbf{r}_2,i\omega_n) = \int_{-\infty}^{+\infty} d\omega \frac{A_{s,t}(\mathbf{r}_1,\mathbf{r}_2,\omega)}{i\omega_n-\omega}. \tag{2.17}$$

$\omega_n = \frac{(2n+1)\pi}{\beta}$ since electrons are fermions. In the definition operators $\psi_{s,t}(\mathbf{r},\tau) = e^{K\tau}\psi_{s,t}(\mathbf{r})e^{-K\tau}$, $\psi^\dagger_{s,t}(\mathbf{r},\tau) = e^{K\tau}\psi^\dagger_{s,t}(\mathbf{r})e^{-K\tau}$. Noticing:

$$\begin{aligned} & \left\langle T_\tau \psi^\dagger_s(\mathbf{r}_1,\tau)\psi_t(\mathbf{r}_2,\tau)\psi^\dagger_t(\mathbf{r}'_2,0)\psi_s(\mathbf{r}'_1,0)]\right\rangle_0 \\ = \;& \mathbf{Tr}\{e^{\beta(\Omega-H_s-H_t+\mu_sN_s+\mu_tN_t)} T_\tau \psi^\dagger_s(\mathbf{r}_1,\tau)\psi_t(\mathbf{r}_2,\tau)\psi^\dagger_t(\mathbf{r}'_2,0)\psi_s(\mathbf{r}'_1,0)\} \\ = \;& \mathbf{Tr}\{e^{\beta(\Omega-H_s-H_t+\mu_sN_s+\mu_tN_t)} T_\tau \psi_t(\mathbf{r}_2,\tau)\psi^\dagger_t(\mathbf{r}'_2,0)\psi^\dagger_s(\mathbf{r}_1,\tau)\psi_s(\mathbf{r}'_1,0)\} \\ = \;& \mathbf{Tr}\{e^{\beta(\Omega_t-H_t+\mu_tN_t)} T_\tau \psi_t(\mathbf{r}_2,\tau)\psi^\dagger_t(\mathbf{r}'_2,0)\}(-1)\mathbf{Tr}\{e^{\beta(\Omega_s-H_s+\mu_sN_s)} T_\tau \psi_s(\mathbf{r}'_1,0)\psi^\dagger_s(\mathbf{r}_1,\tau)\} \\ = \;& -\left\langle T_\tau \psi_t(\mathbf{r}_2,\tau)\psi^\dagger_t(\mathbf{r}'_2,0)\right\rangle_0 \left\langle T_\tau \psi_s(\mathbf{r}'_1,0)\psi^\dagger_s(\mathbf{r}_1,\tau)\right\rangle_0 \\ = \;& -G^M_t(\mathbf{r}_2,\mathbf{r}'_2,\tau)G^M_s(\mathbf{r}'_1,\mathbf{r}_1,-\tau) \end{aligned} \tag{2.18}$$

where $e^{\beta\Omega_{s,t}} = e^{\beta(H_{s,t}-\mu_{s,t}N_{s,t})}$, it is straightforward to write:

$$\begin{aligned} \chi^M(i\Omega_n) &= -\int_0^\beta d\tau e^{i\Omega_n\tau}\left\langle T_\tau \chi_\tau \chi^\dagger_0\right\rangle_0 \\ &= -\int_0^\beta d\tau e^{i\Omega_n\tau}\left\langle T_\tau \int d\mathbf{r}_1 d\mathbf{r}_2 T(\mathbf{r}_2,\mathbf{r}_1)\psi^\dagger_s(\mathbf{r}_1,\tau)\psi_t(\mathbf{r}_2,\tau)\times \right. \\ &\qquad \left. \int d\mathbf{r}'_1 d\mathbf{r}'_2 T^*(\mathbf{r}'_2,\mathbf{r}'_1)\psi^\dagger_t(\mathbf{r}'_2,0)\psi_s(\mathbf{r}'_1,0)]_0\right\rangle \end{aligned}$$

$$
\begin{aligned}
&= \int d\mathbf{r}_1 d\mathbf{r}_2 d\mathbf{r}'_1 d\mathbf{r}'_2 T(\mathbf{r}_2,\mathbf{r}_1)T^*(\mathbf{r}'_2,\mathbf{r}'_1) \times \\
&\quad \int_0^\beta d\tau e^{i\Omega_n\tau} G_t^M(\mathbf{r}_2,\mathbf{r}'_2,\tau) G_s^M(\mathbf{r}'_1,\mathbf{r}_1,-\tau) \\
&= \int d\mathbf{r}_1 d\mathbf{r}_2 d\mathbf{r}'_1 d\mathbf{r}'_2 T(\mathbf{r}_2,\mathbf{r}_1)T^*(\mathbf{r}'_2,\mathbf{r}'_1) \times \\
&\quad \int_0^\beta d\tau e^{i\Omega_n\tau} \frac{1}{\beta}\sum_l e^{-i\omega_l\tau} G_t^M(\mathbf{r}_2,\mathbf{r}'_2,i\omega_l) \frac{1}{\beta}\sum_k e^{i\omega_k\tau} G_s^M(\mathbf{r}'_1,\mathbf{r}_1,i\omega_k) \\
&= \int d\mathbf{r}_1 d\mathbf{r}_2 d\mathbf{r}'_1 d\mathbf{r}'_2 T(\mathbf{r}_2,\mathbf{r}_1)T^*(\mathbf{r}'_2,\mathbf{r}'_1) \times \\
&\quad \frac{1}{\beta}\sum_l G_t^M(\mathbf{r}_2,\mathbf{r}'_2,i\omega_l) G_s^M(\mathbf{r}'_1,\mathbf{r}_1,i\omega_l - i\Omega_n) \\
&= \int d\mathbf{r}_1 d\mathbf{r}_2 d\mathbf{r}'_1 d\mathbf{r}'_2 T(\mathbf{r}_2,\mathbf{r}_1)T^*(\mathbf{r}'_2,\mathbf{r}'_1) \times \\
&\quad \frac{1}{\beta}\sum_l \int_{-\infty}^{+\infty} d\omega_2 \frac{A_t(\mathbf{r}_2,\mathbf{r}'_2,\omega_2)}{i\omega_l - \omega_2} \int_{-\infty}^{+\infty} d\omega_1 \frac{A_s(\mathbf{r}'_1,\mathbf{r}_1,\omega_1)}{i\omega_l - i\Omega_n - \omega_1} \\
&= \int d\mathbf{r}_1 d\mathbf{r}_2 d\mathbf{r}'_1 d\mathbf{r}'_2 T(\mathbf{r}_2,\mathbf{r}_1)T^*(\mathbf{r}'_2,\mathbf{r}'_1) \times \\
&\quad \int d\omega_1 d\omega_2 \frac{A_s(\mathbf{r}'_1,\mathbf{r}_1,\omega_1)A_t(\mathbf{r}_2,\mathbf{r}'_2,\omega_2)}{\omega_2 - \omega_1 - i\Omega_n}(f(\omega_2) - f(\omega_1)). \qquad (2.19)
\end{aligned}
$$

We used identity:

$$
\frac{1}{\beta}\sum_{l=-\infty}^{+\infty} \frac{1}{(i\omega_l - \omega_2)(i\omega_l - i\Omega_n - \omega_1)} = \frac{f(\omega_2)}{\omega_2 - i\Omega_n - \omega_1} + \frac{f(\omega_1 + i\Omega_n)}{\omega_1 + i\Omega_n - \omega_2}. \qquad (2.20)
$$

$f(\omega) = \frac{1}{e^{\beta\omega}+1}$ is the Fermi function and $f(\omega_1 + i\Omega_n) = f(\omega_1)$ for $\Omega_n = \frac{2n\pi}{\beta}$. Following Eq. 2.13, 2.15 and 2.19, the single particle current:

$$
\begin{aligned}
I_s &= 2e\mathrm{Im}\chi^{\mathrm{M}}(\mathrm{i}\Omega_\mathrm{n} \to -\mathrm{eV} + \mathrm{i}\delta) \\
&= 2e\mathrm{Im}\int \mathrm{d}\mathbf{r}_1\mathrm{d}\mathbf{r}_2\mathrm{d}\mathbf{r}'_1\mathrm{d}\mathbf{r}'_2\mathrm{T}(\mathbf{r}_2,\mathbf{r}_1)\mathrm{T}^*(\mathbf{r}'_2,\mathbf{r}'_1) \times \\
&\quad \int d\omega_1 d\omega_2 \frac{A_s(\mathbf{r}'_1,\mathbf{r}_1,\omega_1)A_t(\mathbf{r}_2,\mathbf{r}'_2,\omega_2)}{\omega_2 - \omega_1 + eV - i\delta}(f(\omega_2) - f(\omega_1)) \\
&= 2e\int d\mathbf{r}_1 d\mathbf{r}_2 d\mathbf{r}'_1 d\mathbf{r}'_2 T(\mathbf{r}_2,\mathbf{r}_1)T^*(\mathbf{r}'_2,\mathbf{r}'_1) \times \\
&\quad \int d\omega_1 d\omega_2 A_s(\mathbf{r}'_1,\mathbf{r}_1,\omega_1)A_t(\mathbf{r}_2,\mathbf{r}'_2,\omega_2)(f(\omega_2) - f(\omega_1))\pi\delta(\omega_2 - \omega_1 + eV) \\
&= 2\pi e\int d\omega_1 (f(\omega_1 - eV) - f(\omega_1)) \times
\end{aligned}
$$

$$\int d\mathbf{r}_1 d\mathbf{r}_2 d\mathbf{r}'_1 d\mathbf{r}'_2 T(\mathbf{r}_2, \mathbf{r}_1) T^*(\mathbf{r}'_2, \mathbf{r}'_1) A_s(\mathbf{r}'_1, \mathbf{r}_1, \omega_1) A_t(\mathbf{r}_2, \mathbf{r}'_2, \omega_1 - eV). \quad (2.21)$$

Now we can choose the representation of the tunneling matrix 2.5 so that the spectral functions are diagonalized:

$$\begin{aligned} \int d\mathbf{r}_1 d\mathbf{r}'_1 \varphi^*_{\nu'}(\mathbf{r}'_1) \varphi_\nu(\mathbf{r}_1) A_s(\mathbf{r}'_1, \mathbf{r}_1, \omega) &= \delta_{\nu\nu'} A_{s,\nu}(\omega), \\ \int d\mathbf{r}_2 d\mathbf{r}'_2 \varphi^*_{\mu}(\mathbf{r}_2) \varphi_{\mu'}(\mathbf{r}'_2) A_t(\mathbf{r}_2, \mathbf{r}'_2, \omega) &= \delta_{\mu\mu'} A_{t,\mu}(\omega). \end{aligned}$$

After inserting back the $\hbar^{-1}$ dimensional factor, the current can be written as:

$$I_s = \frac{2\pi e}{\hbar} \int d\omega (f(\omega - eV) - f(\omega)) \sum_{\mu\nu} |T_{\mu\nu}|^2 A_{s,\nu}(\omega) A_{t,\mu}(\omega - eV). \quad (2.22)$$

This result can be applied to any tunneling experiment. In the STM case we are more interested in the real space result.

2.3.2 Tersoff-Hamann Model

The essential problem is now to calculate the tunneling matrix element $T_{\mu\nu}$. In Bardeen theory [5] the tunneling matrix element is the expectation value of the single particle current in the direction z normal to the plane of the junction, through a surface S lying entirely in the barrier region:

$$T_{\mu\nu} = -\frac{\hbar^2}{2m} \int_s dS \left(\varphi^*_\nu \frac{\partial \varphi_\mu}{\partial z} - \varphi_\mu \frac{\partial \varphi^*_\nu}{\partial z} \right). \quad (2.23)$$

Tersoff and Hamann [10, 11] were the first to treat the STM tunneling case. In their model the tip was represented as a locally spherical potential well. The tip wave functions in the region of interest were taken to have the asymptotic spherical (s-wave) form. This approximation enabled them to calculate the tunneling matrix

element:

$$T_{\mu\nu} \propto \varphi^*_\nu(\mathbf{r}_0).$$

$\varphi_\nu(\mathbf{r}_0)$ is the wave function of the sample at $\mathbf{r}_0$, the center of curvature of the tip [11]. Using Eq. 2.5 and the completion properties of φ_ν, we have:

$$\begin{aligned} T(\mathbf{r}_2, \mathbf{r}_1) &= \sum_{\mu\nu} \varphi^*_\mu(\mathbf{r}_2) T_{\mu\nu} \varphi_\nu(\mathbf{r}_1) \propto \sum_{\mu\nu} \varphi^*_\mu(\mathbf{r}_2) \varphi^*_\nu(\mathbf{r}_0) \varphi_\nu(\mathbf{r}_1) \\ &\propto \delta(\mathbf{r}_1 - \mathbf{r}_0) \sum_\mu \varphi^*_\mu(\mathbf{r}_2). \end{aligned}$$

Another important assumption here is that the tip is made of simple metal. The spectral function of the tip then can be written as [12]:

$$A_t(\mathbf{r}, \mathbf{r}', \omega) = \sum_\mu \varphi_\mu(\mathbf{r}) \varphi^*_\mu(\mathbf{r}') \delta(\omega - \epsilon_\mu).$$

The single particle current in Eq. 2.21 is now:

$$\begin{aligned} I_s \propto\ & \frac{2\pi e}{\hbar} \int d\omega_1 (f(\omega_1 - eV) - f(\omega_1)) \times \\ & \int d\mathbf{r}_1 d\mathbf{r}_2 d\mathbf{r}'_1 d\mathbf{r}'_2 \delta(\mathbf{r}_1 - \mathbf{r}_0) \sum_\mu \varphi^*_\mu(\mathbf{r}_2) \delta(\mathbf{r}'_1 - \mathbf{r}_0) \sum_{\mu'} \varphi_{\mu'}(\mathbf{r}'_2) A_s(\mathbf{r}'_1, \mathbf{r}_1, \omega_1) \times \\ & \sum_{\mu"} \varphi_{\mu"}(\mathbf{r}_2) \varphi^*_{\mu"}(\mathbf{r}'_2) \delta(\omega_1 - eV - \epsilon_{\mu"}) \\ =\ & \frac{2\pi e}{\hbar} \int d\omega (f(\omega - eV) - f(\omega)) A_s(\mathbf{r}_0, \mathbf{r}_0, \omega) \times \\ & \sum_{\mu\mu'\mu"} \int d\mathbf{r}_2 \varphi^*_\mu(\mathbf{r}_2) \varphi_{\mu"}(\mathbf{r}_2) \int d\mathbf{r}'_2 \varphi^*_{\mu"}(\mathbf{r}'_2) \varphi_{\mu'}(\mathbf{r}'_2) \delta(\omega - eV - \epsilon_{\mu"}) \\ =\ & \frac{2\pi e}{\hbar} \int d\omega (f(\omega - eV) - f(\omega)) A_s(\mathbf{r}_0, \mathbf{r}_0, \omega) \sum_{\mu\mu'\mu"} \delta_{\mu\mu"} \delta_{\mu'\mu"} \delta(\omega - eV - \epsilon_{\mu"}) \\ =\ & \frac{2\pi e}{\hbar} \int d\omega (f(\omega - eV) - f(\omega)) A_s(\mathbf{r}_0, \mathbf{r}_0, \omega) \sum_{\mu"} \delta(\omega - eV - \epsilon_{\mu"}). \end{aligned}$$

The local density of states (LDOS) of the sample can be related to the spectral function [12] through $N_s(\mathbf{r}, \omega) = A_s(\mathbf{r}, \mathbf{r}, \omega)$. Since the tip material is a simple

metal, the density of states of the tip, $N_t(\omega) = \sum_\mu \delta(\omega - \epsilon_\mu)$. Finally we have the relation between the single particle tunneling current and the LDOS of the sample:

$$I_s \propto \int d\omega (f(\omega - eV) - f(\omega)) N_s(\mathbf{r}_0, \omega) N_t(\omega - eV) \tag{2.24}$$

The second term of the current in Eq. 2.10, $I_J(t)$, describes the pair tunneling current or Josephson current. It was discussed by Josephson thoroughly [13]. In our work we didn't use superconducting tips. Therefore, the contribution from this term to our results can be neglected.

2.3.3 Tunneling Conductance and Density of States

In tunneling experiments, the connection between the measurable value, the tunneling conductance, and the density of states of the sample can be derived from the general tunneling result Eq. 2.22. For simplicity we set temperature to zero and assume here a constant tunneling matrix $T_{\mu\nu} = T$. Thus from Eq. 2.22 now the tunneling conductance can be written as:

$$\sigma(V) = \frac{dI_s}{dV} = \frac{2\pi e^2}{\hbar} |T|^2 N_t(0) N_s(eV). \tag{2.25}$$

Here the energy is measured from the Fermi energy. This general relation reveals the essence of tunneling spectroscopy: we can directly probe the DOS of the system versus the energy by measuring the differential conductance versus the bias voltage. Also here $|T|^2 \propto e^{-2\kappa d}$ as can be seen from Eq. 2.23 and the exponential decaying property of the wave functions in the barrier. This relation accounts for the current-distance relationship as described in Sec. 2.2.

From Eq. 2.24, assuming a structureless tip DOS ($N_t(\omega - eV) = \text{const.}$), we have:

$$\sigma(\mathbf{r}_0, V) = \frac{dI_s}{dV} \propto \int d\omega(-f'(\omega - eV))N_s(\mathbf{r}_0, \omega). \tag{2.26}$$

The derivative of the Fermi function $f'(\omega - eV)$ in the equation can be viewed as a thermally broadened $\delta(\omega - eV)$ function. Thus the STM tunneling spectroscopy (or scanning tunneling spectroscopy, in short STS) at finite temperatures measures the thermally smeared LDOS of the sample at the position of tunneling.

These remarkably simple and direct relations between the measurable conductance and the LDOS of the sample is the reason why STM and STS are so powerful tools to study complex electronic systems. In the next section I will review four frequently used operation modes of STM and how the actual measurements are carried out in our experiments.

2.4 Operation Modes of STM

In experiments, generally two types of data are acquired by a STM system: topography and spectroscopy. In the topography mode, current data is correlated with the height information at the tip position. The bias voltage is usually set to be constant. In the spectroscopy mode, the conductance versus bias voltage relation is measured to reveal the LDOS at the position of tunneling. Combining them with atomic resolution, our STM can perform different tasks with respect to different physical parameters of the system under study. Here we introduce some of the operation modes that can be realized and are useful in our research.

2.4.1 Constant Current Topography Mode

This is the most commonly used mode of our system. In this mode the tunneling current I is set to a constant (typically 0.1 nA) as well as the bias voltage (typical value 0.1 V). In our system the bias voltage is applied on the sample and the tip is virtually grounded. With the feedback on (typical PID value of the feedback for our system: P = 0, I = 0.5, D = 0), we set the raster motion of the tip at a certain speed (typical value 5 to 100 nm/s). When the tip moves from one pixel to the next in the image (an image is typically 256×256 pixels), the feedback loop keeps the current constant by moving the tip toward or away from the surface depending on the measured value. This motion of the tip in the z direction was realized by applying different V_z voltages on the scanner which is recorded as a measurement of relative height difference of the tip at positions of the two pixels. At the same time the (x, y) position of the tip is given by the voltages V_x, V_y on the scanner. In essence, we measure $z(x, y)$ of the tip while keeping $I(x, y)$ and V_{bias} constant. If the LDOS of the sample is homogeneous in the field of view, according to the discussion in Sec. 2.2, a constant tunneling current will imply a constant distance between the tip and sample. The moving tip during scanning is following the height profile of the sample surface. The recorded height information $z(x, y)$ of the tip at each point reproduces the topographic profile of the sample in the field of view.

In reality, the feedback loop is not perfect and the output $I(x, y)$ is not constant everywhere. We record both $z(x, y)$ and $I(x, y)$ and refer to them as the topographic image and the current image respectively. When inhomogeneities are

present, *i.e.*, the LDOS varies in a certain area due to impurity, surface state or other reasons, it will be recorded as surface corrugations in the topographic image because the feedback mechanism will balance the current loss or gain due to Eq. 2.24 by decreasing or increasing the distance between the tip and sample.

2.4.2 Current vs. Distance Mode

While in the constant current mode, we use the feedback to keep the distance between the tip and sample constant, in the current vs. distance mode we turn off the feedback at the position of study and vary the distance as we record the current. Following the relations between the current and the tunneling distance (Eq. 2.1), we can derive the work function by:

$$\phi = \frac{\hbar^2}{8m}\left(\left.\frac{\partial \ln I}{\partial d}\right|_V\right)^2 \approx 0.95\left(\left.\frac{\partial \ln I}{\partial d}\right|_V\right)^2$$

where ϕ is in eV, I in A, and d in Å. In the experiment, after establishing feedback at the position of study with a tunneling distance d_0, we withdraw the tip by Δd from the surface each step for N steps ($N \sim 10-30$, total distance $\sim$ several Å). The slope of the log-linear plot of $I(d_0 - n\Delta d)$ against $d_0 - n\Delta d$ with $0 \leq n \leq N$ gives the convoluted work function of the tip-sample system [14, 15]. We always use this process to check the tip status after tip cleaning and before scanning to make sure the metallic tip end is exposed by the cleaning or there is no dangling oxide material in between the tip and sample. The typical value of measured ϕ in our system for a W tip against Au crystal is about 1.5 to 3 V.

2.4.3 Differential Conductance Spectroscopy Mode

Similar to the current vs. distance mode, the differential conductance spectroscopy mode is also a local or point mode. As discussed in Sec. 2.3, the local tunneling conductance $\sigma(\mathbf{r}_0, V) = \frac{dI_s}{dV}$ measures directly the LDOS of the sample through Eq. 2.26. In the experiment we use a lock-in amplifier to add a small ac signal $(dV)\sin(\omega t)$ to the bias voltage V, and measure the corresponding modulation in the tunneling current. Taylor expansion of the total current gives:

$$I(V + dV\sin(\omega t)) = I(V) + \left.\frac{dI}{dV}\right|_V dV\sin(\omega t) + O((dV)^2). \tag{2.27}$$

The lock-in amplifier is able to select a signal component at a given sampling frequency and phase. In this case the amplitude equals $\left.\frac{dI}{dV}\right|_V dV = \sigma(\mathbf{r}_0, V)dV$. Dividing that by the sampling amplitude dV, we extract the local differential conductance $\sigma(\mathbf{r}_0, V)$ which is proportional to the LDOS of the sample at energy eV measured from the Fermi energy E_F. To obtain the spectrum at the point of study, the feedback is turned off once the tunneling distance d is established as we did in the previous mode, then the bias voltage is swept from V_a to V_b with an even interval of $\Delta V = \frac{V_b - V_a}{N}$ and the corresponding differential conductances $\sigma(\mathbf{r}_0, V_n)$ are recorded. Here $0 \leq n \leq N$, $V_n = V_a + n\Delta V$. Thus the spectrum we obtained is the LDOS $N_s(\mathbf{r}_0, [eV_a, eV_b])$ at $N + 1$ energies. Note in this mode we fix the distance d and change the bias voltages while in the previous one we did the opposite. The criteria on choosing ΔV (or N) and dV to optimize the energy resolution of the spectroscopy with respect to thermal broadening is that $k_B T \leq dV \leq \Delta V$. Typical values of dV are in the range of 0.1 mV to 10 mV. The advantage of using a lock-in amplifier is

that by choosing the sampling frequency $f_{mod} = \frac{\omega}{2\pi}$ outside the typical frequency domain of mechanical vibrations or electronic noise the sensitivity of measurement can be remarkably enhanced. Typical sampling frequencies can be from several hundred hertz to several thousand hertz. The averaging time of acquisition at each voltage is usually set to be more than 3 times the lock-in averaging time (the time constant). Since this experiment is very sensitive to the environment, the best settings have to be determined by trial and error to maximize the signal to noise ratio every time we run a new spectrum.

2.4.4 Differential Conductance Mapping Mode

The differential conductance mapping mode is a natural extension of the technique described in the previous section. At the end of the process described above, if we turn on the feedback and move the tip to the next position to repeat it with the same settings, we will have another series of $\sigma(\mathbf{r}'_0, V_n)$ and so forth another spectrum of $N_s(\mathbf{r}'_0, [eV_a, eV_b])$ at the new position $\mathbf{r}'_0$. Continuing this until the spectra at all the positions of pixels of an image in the field of view are obtained, and putting them together we acquire the differential conductance map $\sigma(\mathbf{r}_{ij}, V_n) = \sigma(x_i, y_j, V_n)$. The map is then organized in a series of layers of conductance images $\sigma(\mathbf{r}_{ij}, V_n)$ with each layer corresponding to one voltage value V_n. In this way, the spatial variation of LDOS at a certain energy as well as the evolution of it with energy can be easily visualized. This direct manifestation of the LDOS features of complex electronic systems is the main power of the LTSTM system.

2.4.5 Single Conductance Imaging Mode

This is a simplified version of the differential conductance map method. In this mode we are only interested in the imaging of one particular layer of the map with a fixed energy eV. One way of doing it is using the mapping method, turning the feedback off while at the position and recording the conductance and then moving the tip with the feedback turned back on. It is very time-consuming to turn the feedback and the lock-in signal on and off at each pixel point of the image. When we are especially concerned with the speed of the imaging we choose another method: we leave the feedback and the lock-in amplifier on and record the differential conductance $\sigma(x_i, y_j, V)$ and $z(x_i, y_j)$ at the same time through different channels. We choose a short time constant of the lock-in amplifier so the averaging can be done in the time of acquiring the topographic data. The sampling frequency is set high enough so the feedback loop can not keep up with the oscillation of the current. This fast imaging technique proved very useful when we imaged moving vortices, to be described in Chapter 5.

2.5 Experimental Setup

Our STM project started in 2002 led by Dr. Barry Barker in association with the Quantum Computing group here at LPS (Laboratory for Physical Sciences). The purpose of the low temperature STM (LTSTM) is to investigate fine electronic structures on the surfaces of a variety of samples at low temperatures and in high magnetic fields. The quality of the STM operation depends on three conditions. The

first one is a flat sample surface with no unnecessary contamination. The second one is a stable sharp tip that can both give us atomic resolution and survive long spectroscopic measurements. The third one is the stable environment with minimum amount of thermal and vibrational noise. To meet all the challenges, we chose to focus on the following 4 aspects of the system in our design: 1) a UHV stage to take care of the sample surface preparation, 2) a compact STM design, which will allow it to be used in a bore of a superconducting magnet despite the limited space, 3) a 4 K environment with the thermal mass minimized, and 4) an optimal vibration isolation system.

In what follows, I will describe the system by dividing it to two stages: the room temperature (RT) stage and the low temperature (LT) stage. Figure 2.2 shows the 3D schematic of the design of the whole system. The real system constructed as of today is illustrated in Fig. 2.3. The RT stage is above the optical table (7) which consists of the UHV system (2, 5, 6), the sample transfer system (3, 4) and the vibration isolation system (7). Below the table is the LT stage. A 4 K probe (8) is attached to the RT stage through a gate valve that separates the two vacua. The STM (10) is rigidly attached to the 4 K probe at the bottom with the 4 K probe vacuum chamber immersed in liquid Helium contained in a superconducting magnet dewar (9). The electronics include the magnet and UHV control units (13) and the STM electronic control unit (14).

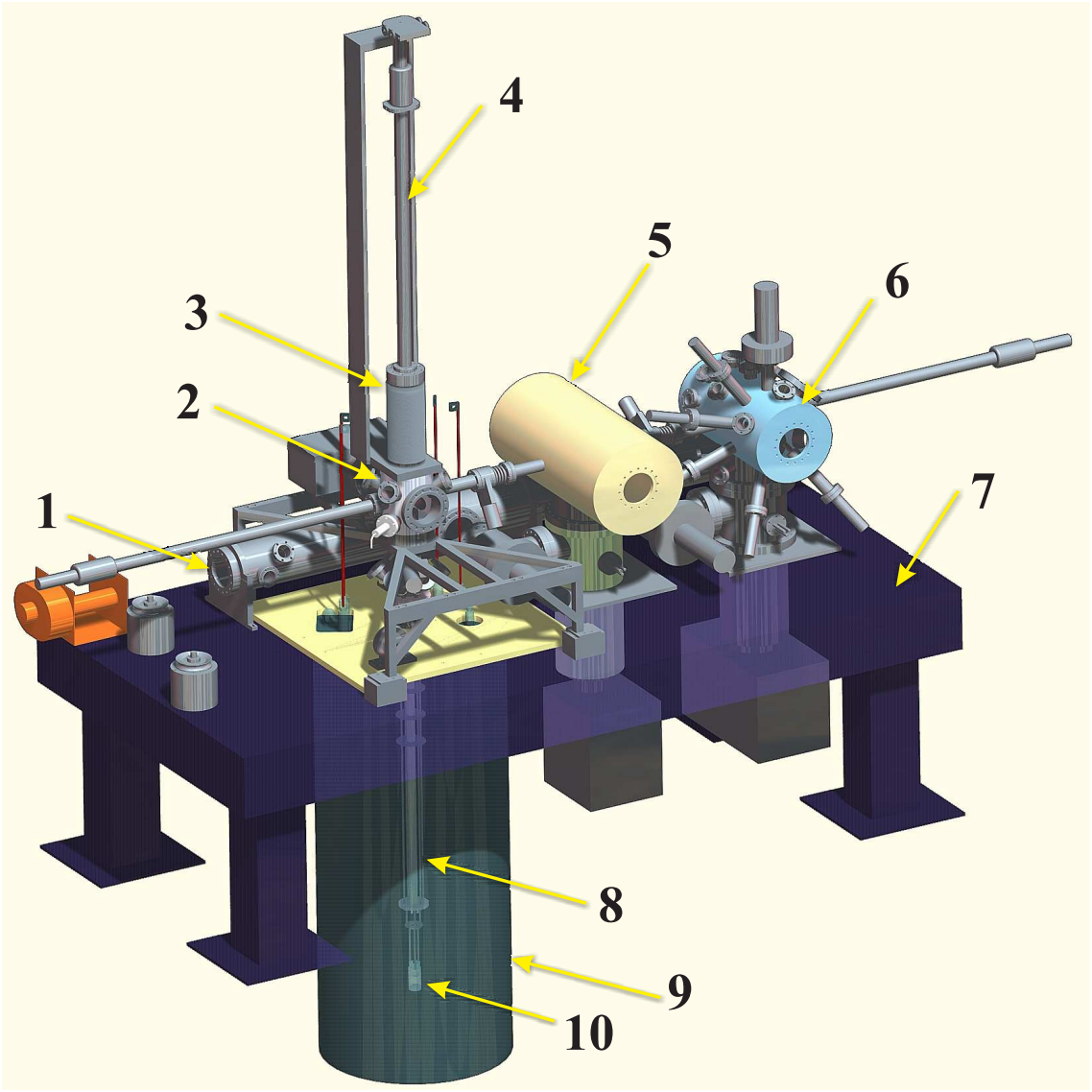

Figure 2.2: **3D System Design Schematic.** 1) The major pumping port. 2) The sample transfer chamber. 3) The compressible bellow. 4) The magnetic transfer rod in z direction. 5) The analysis chamber. 6) The preparation chamber. 7) The vibration isolation system. 8) The 4 K probe. 9) The superconducting magnet dewar. 10) The STM.

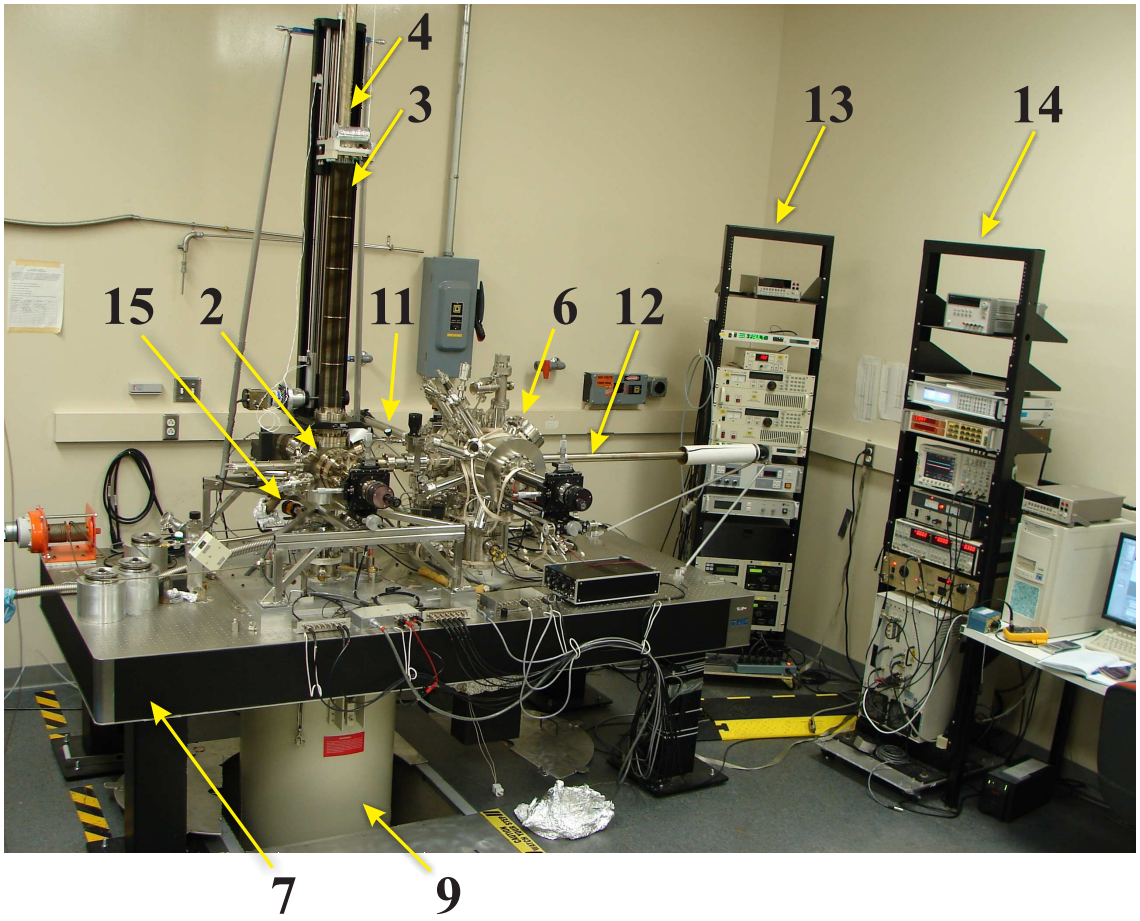

Figure 2.3: **Real System as of August 28, 2008.** The part numbers are shared with Fig. 2.2 2) Transfer chamber. 3) UHV compressible bellow. 4) Magnetic transfer rod in Z direction. 6) The preparation chamber. 7) The optical table. 9)The superconducting magnet dewar. 11) Magnetic transfer rod in Y direction. 12) Magnetic transfer rod in X direction. 13) Magnet control unit and UHV control unit. 14) Data acquisition and STM electronic control unit.

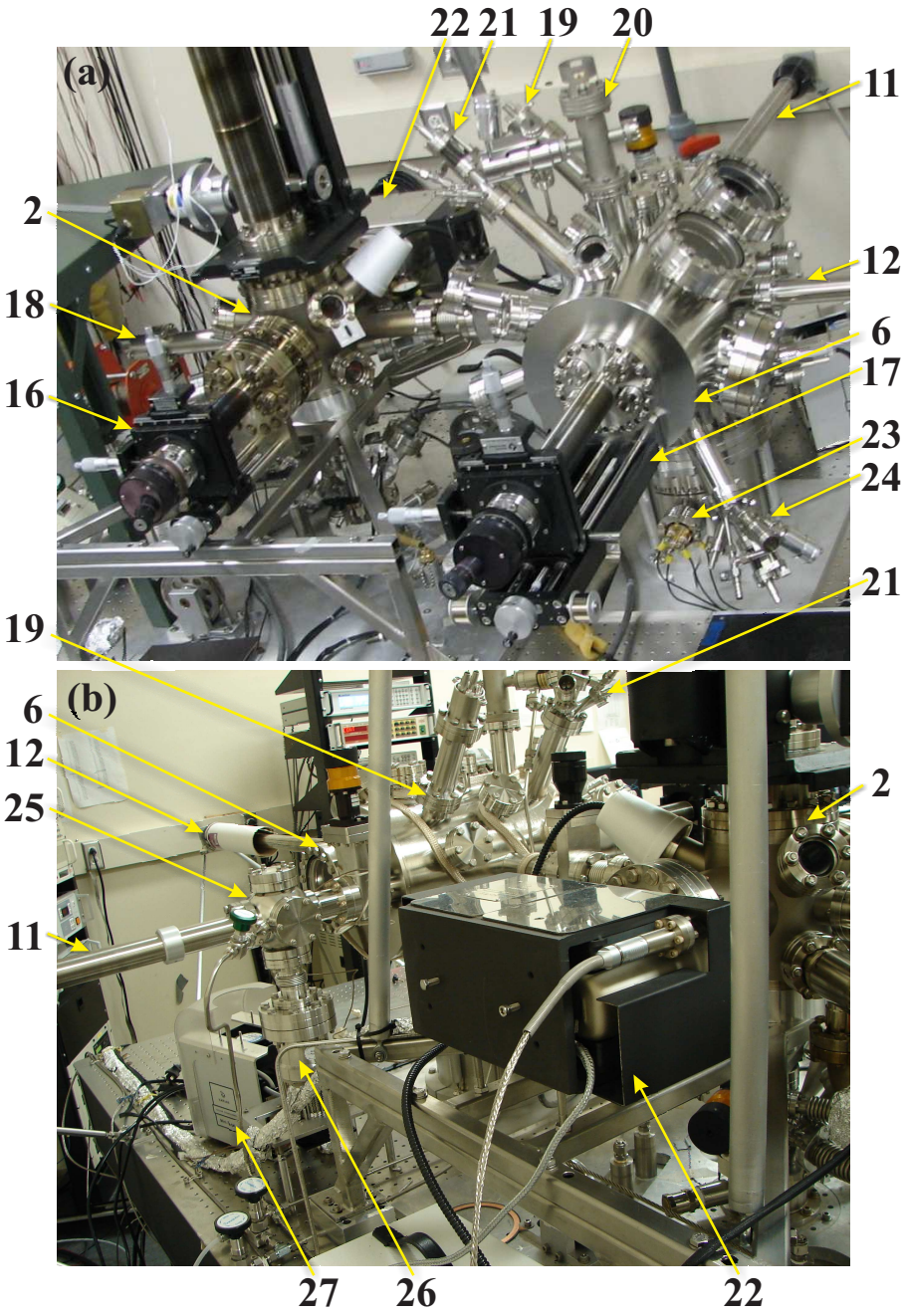

Figure 2.4: **The Ultra-high Vacuum System.** The front (a) and back side (b). 2) Transfer chamber. 6) The preparation chamber. 11) Magnetic transfer rod in Y direction. 12) Magnetic transfer rod in X direction. 16) 17) XYZ stage. 18) 19) Residual gas analyzer 20) Ar^+ sputter gun. 21) 24) Evaporator. 22) Ion getter pump. 23) Titanium sublimation pump. 25) Fast entry lock. 26) 27) Table turbo pump system.

2.5.1 RT stage

As shown in Fig. 2.3 the RT stage above the table (7) is kept at room temperature during STM operation. It contains two UHV chambers: the preparation chamber (6) and the transfer chamber (2). Both are equipped with an ion getter pump (IGP) and a titanium sublimation pump (TSP). The UHV condition in each chamber is obtained through the following process: first it was pumped from atmospheric pressure to about 10^{-5} mbar by a turbo-molecular pump with a rotary forepump through a gate valve. At the same time we heat the chamber to above 100°C to outgas. When the outgassing decreases we stop the heating and turn on the TSP. This will bring the pressure down to about 10^{-8} mbar, and finally the vacuum will reach 10^{-11} mbar by turning on the IGP. Usually the vacuum is kept at 10^{-11} mbar by regularly firing the TSP. When our STM is operating, the TSP has to be turned off but the vacuum can still be kept at $\leq 5 \times 10^{-10}$ mbar.

Fig. 2.4 shows the front and back sides of the chambers. In the preparation chamber (6), we installed an Ar^+ sputter gun (20), an ion gauge, a quadrupole residual gas analyzer (19), two thermal evaporators (21, 24), 5 viewports and many other ports for further development. As illustrated in Fig. 2.4(b), a fast entry lock subchamber (25) is connected to the preparation chamber (6) through a 2.75" gate valve. The subchamber is connected to a turbo-molecular pump (Mini-task 600i from Varian Inc.) (26) at the bottom with a prepump (27). It can pump the subchamber from atmospheric pressure down to $\sim 1 \times 10^{-8}$ mbar in ~ 20 minutes. The transfer chamber (2) is equipped with a quadrupole residual gas analyzer, an

ion gauge and 5 view ports. Another analysis chamber (5 in Fig. 2.2) will be added to the left of the preparation chamber in the near future.

In experiment, the sample is carried on a sample stud (1 in Fig. 2.6), a metal piece with a fixed shape to fit the STM. The freshly prepared sample is loaded into the fast entry lock with the sample stud locked in a sample transfer plate. The subchamber is then pumped down to $\sim 1 \times 10^{-8}$ mbar. A cleaving device is housed in the subchamber for cleaving layered samples such as 2H-$NbSe_2$ or graphite. The gate valve is opened and the sample is then transferred to the preparation chamber by the X direction sample manipulator (12). The sample holder can be taken out from the head of manipulator (12) by the Y direction sample manipulator (11). Then the X manipulator (12) is retracted and the gate valve closed. In the preparation chamber, the sample can be directly transferred to the transfer chamber by the Y manipulator (11). It can also be stored in a storage place built into the sample stage that is housed in the preparation chamber and can be manipulated by the XYZ stage (17) outside the chamber. Or it can be treated by seating it on the sample holder at the stage center which is the focal point of all the preparation apparatus (an Ar^+ sputter gun (20), evaporators (21), (24) and a heater built underneath the sample holder). The finished sample is then transferred through a 2.75" gate valve to the sample stage housed in the transfer chamber (2) which is also equipped with a XYZ stage (16). In the transfer chamber, the sample manipulator can take the sample stud directly out of the sample holder which is locked in the XYZ stage (16). The XYZ stage (16) is then retracted to ensure clearance for the Z manipulator (4 in Fig. 2.3) to transfer the sample stud to the LT stage and eventually lock it into the STM.

This long translational motion is made possible by incorporating a UHV-compatible compressible bellow (3 in Fig. 2.3) and a motorized-screw system and a magnetic transfer rod. The viewports in both chambers help monitor the manipulation and the preparation process. A camera connected to a monitor is set up outside the transfer chamber to assist us in the Z translation by showing the sample stud in the stage to us while we move the magnetic transfer rod.

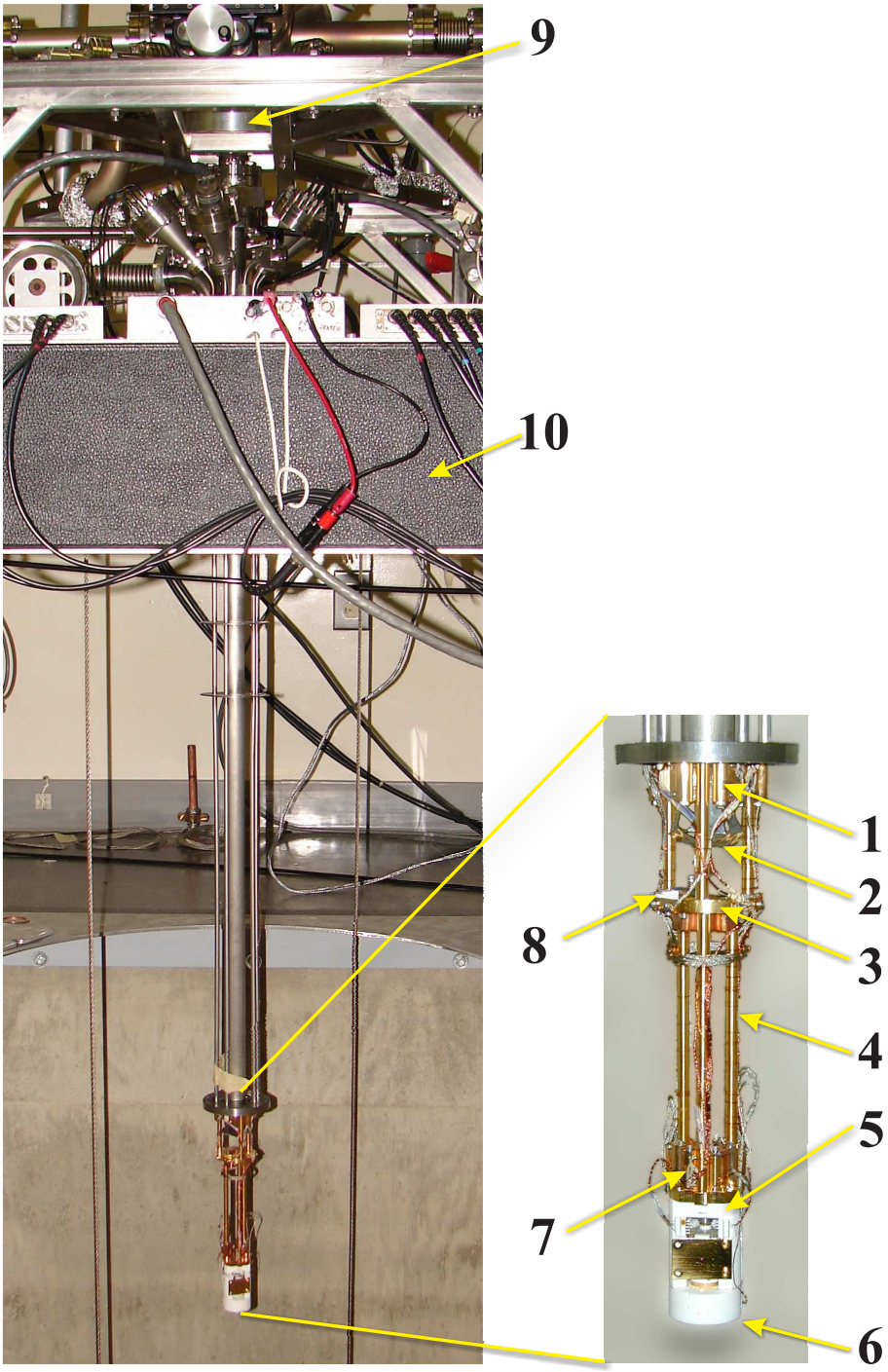

Figure 2.5: **The Low Temperature Stage.** 1) 7) Heat sinks. 2) Heat shield. 3) Precooling stage. 4) Gold Plated OFHC copper rod. 5) STM. 6) Thermometer at the bottom of STM. 8) Thermometer. 9) Gate valve to RT stage. 10) Optical table.

2.5.2 LT stage

The LT stage below the table is connected to the RT stage through a 2.75" gate valve (9) as illustrated in Fig. 2.5. It consists of a 4 K probe, a STM and a superconducting magnet dewar.

The 4 K probe was manufactured here at LPS. The neck plate of the probe is bolted to the table top (10). The basic structure of the probe consists of a 1" center tube as the path for sample transferring which is surrounded by five 0.25" thin wall tubes housing the wiring. On top of the neck plate the center tube is connected to the gate valve with 5 feed-through ports for the wiring and one venting port pointing outward. The venting port enables low temperature vacuum space to be vented and pumped without affecting the UHV in the RT stage. The feed-through ports carry connectors to the control electronics. The portion of the probe below the neck plate is enclosed in the superconducting magnet dewar [1] when the LTSTM is working. Wires run within the 5 thin walled tubes continued from the top feed-throughs down to the top of the vacuum can. Those wires are then thermally anchored (1 in Fig. 2.5) to the top of the vacuum can which will contact directly with the LHe. 2 stages of gold plated oxygen free high conductivity (OFHC) copper rods (3 rods per stage, 4 in Fig. 2.5) serve as support structure and heat sinking for the wires and the STM connected at the bottom. Before going to the STM, the wires are heat sunk again at (7). Heat sinking at (1, 7) is achieved by wrapping wires around the short OFHC copper posts (6 heat sinks for each stage) tightly and then fastening the wires with

[1] Manufactured by the Kadel Engineering Co. (Danville, Indiana, USA). The superconducting magnet was built by the American Magnetics Inc. (Oak Ridge, Tennessee,USA).

copper spring clips. The details of the wiring process can be found in my colleague Jonghee Lee's thesis [16]. This procedure maximized the heat removal, thereby minimizing the heat load on the STM stage. A precooling stage (3) made of OFHC copper joining the 2 stages of OFHC copper rods is used to cool the sample stud coming from room temperature before it is inserted to the STM. The stud can sit in the keyhole through the stage and the metal-metal contact between the stud and stage can cool it down very quickly since the stage is at 4.2 K. Another heat source is the thermal radiation from the center tube directed at the center of the STM. We installed a heat shield (2) to block it that automatically closes the shield after the transfer is finished. The shield is made of stainless steel shims. Three pieces are hinged at the end of the center tube. When the Z transfer rod brings down the sample, an aluminum cylinder slides down the rod and presses on the ends of the 3 leaves in the tube and force the shield to open and the transfer can proceed. Once the transfer rod is brought back the slider will move off the shield, and the spring force at the hinge will bring the leaves together to form a closed shield. This shield proved to be very effective in our system. Two thermometers (6, 8) [2] are installed to monitor the temperatures at the precooling stage and the STM.

The ^{4}He dewar can be raised from the pit below the floor to enclose the 4 K probe and then be bolted to the optical table. A winch-pulley system is installed on the table to assist the lifting. A 2-axis magnet is installed in the bottom of the dewar. The bore size of superconducting solenoid with a maximum field of 9.1 T in Z direction is 2.5" at 4.2 K. The vacuum can of the probe surrounded by the

[2] Cernox HD, Lakeshore Cryogenics.

solenoid has a diameter of 2.35". The maximum field in the horizontal direction is 2 T at 4.2 K. The current leads can be detached from the magnet to reduce the ^{4}He boil-off after the magnetic field is stabilized at the desired field strength and set in persistent mode. The static loss rate of LHe of the dewar is 0.27 L/Hr. With the probe inside the dewar, the holding time of LHe is $\sim$ 7 days ($\sim$ 3 days with the current leads attached). Pumping the LHe bath in the dewar can lower the temperature of the STM to $\sim$ 2.1 K, but the holding time is reduced to $\sim$ 2 days.

To prepare the LT stage, when we are changing tips, for example, we first lower the dewar to the pit below the floor. The 4 K probe is warmed up to room temperature with the gate valve to UHV closed. We then open the vacuum can and work on the STM. After we finish any modifications, we close the vacuum can and pump the probe through the venting port to $\sim 5 \times 10^{-6}$ mbar. Then we cool the probe down to 77 K with liquid nitrogen and to 4.2 K by raising the dewar from the pit with a winching system. The whole turnaround process takes about 20 hours [3] and the system is back to 4.2 K immersed in the LHe bath. The STM will then work in a cryogenic UHV which is estimated to be $\sim 1 \times 10^{-15}$ mbar.

The vibration isolation is all external in our system. Our STM is firmly bolted to the probe. The probe and the dewar are then firmly bolted to the optical table during the operation of the system. The table carrying both the LT stage and the RT stage is floated by air springs installed in the four legs. The weight of the whole system to be floated is about 1500 lbs. The natural frequencies are measured to be

[3] 12 hours to pump the vacuum can, 6 hours to cool down to 77 K and 2 hours again to cool down to 4 K.

$0.8 - 1.7$ Hz for the vertical vibration and $1 - 1.9$ Hz for the horizontal vibration [16].

2.5.3 STM design

The assembled STM with the cross section view is illustrated in Fig. 2.6. Fig. 2.7 shows the schematic of our Pan-style [17] STM and the real manufactured components. The size of the STM is 1.5" in diameter and 2" in height. Such a compact design is necessary for the system to work inside the small bore of the magnet. Non-magnetic materials are chosen for all the components to allow the STM to be used in high magnetic fields. For example, Macor (machinable ceramic) was used for the main body, gold-coated naval brass was used for the screws, and gold-plated copper was used for the capacitor plates.

As illustrated in Fig. 2.7, this STM employs a two-stage tip approach and a top sample loading design. A coarse approach system and a scanner system are integrated in the main body (13). The coarse approach system includes six shear-piezo stacks with Al_2O_3 ceramic contact pads glued on top (7), a sapphire prism (6) with a hole in the center, and a spring press-plate (8) with a ruby ball (16) as the contact. The scanner system consists of a piezo-tube scanner (5) with a tip receptacle (4) glued on the top, a scanner holder (9) with the inner capacitor plate (10) glued at the bottom and a tip cup (3) gripping the metalic tip tightly held in the receptacle by friction. The sample stud (1) can be loaded from the top with the sample glued or clamped onto it facing down.

With both the tip cup and sample stud loaded, the coarse approach starts

first to move the tip toward the sample from the bottom up. The scanner system is bolted to the sapphire shaft and they move as a unit by the "walker", *i.e.*, the six shear-piezo stacks. The major force involved in the motion is the friction force between the contact pads on the stacks and the sapphire prism.

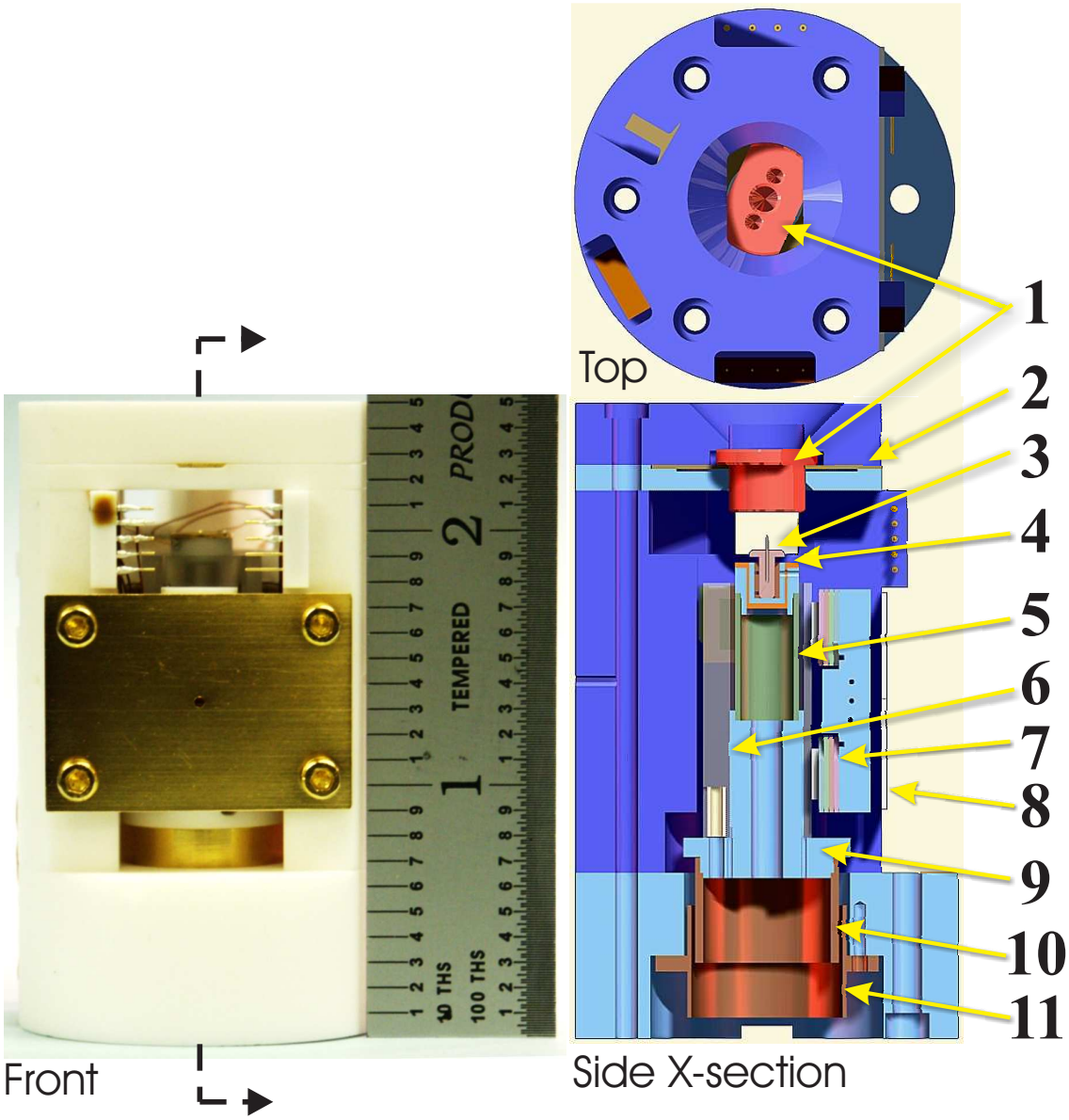

Figure 2.6: **STM Assembled.** The dissembled parts are shown in Fig. 2.7. 1) Sample stud. 2) BeCu spring plate. 3) Tip. 4) Tip holder. 5) Tube scanner. 6) Sapphire prism. 7) Walker. 8) Front spring plate. 9) Scanner holder. 10) Inner capacitance plate. 11) Outer capacitance plate.

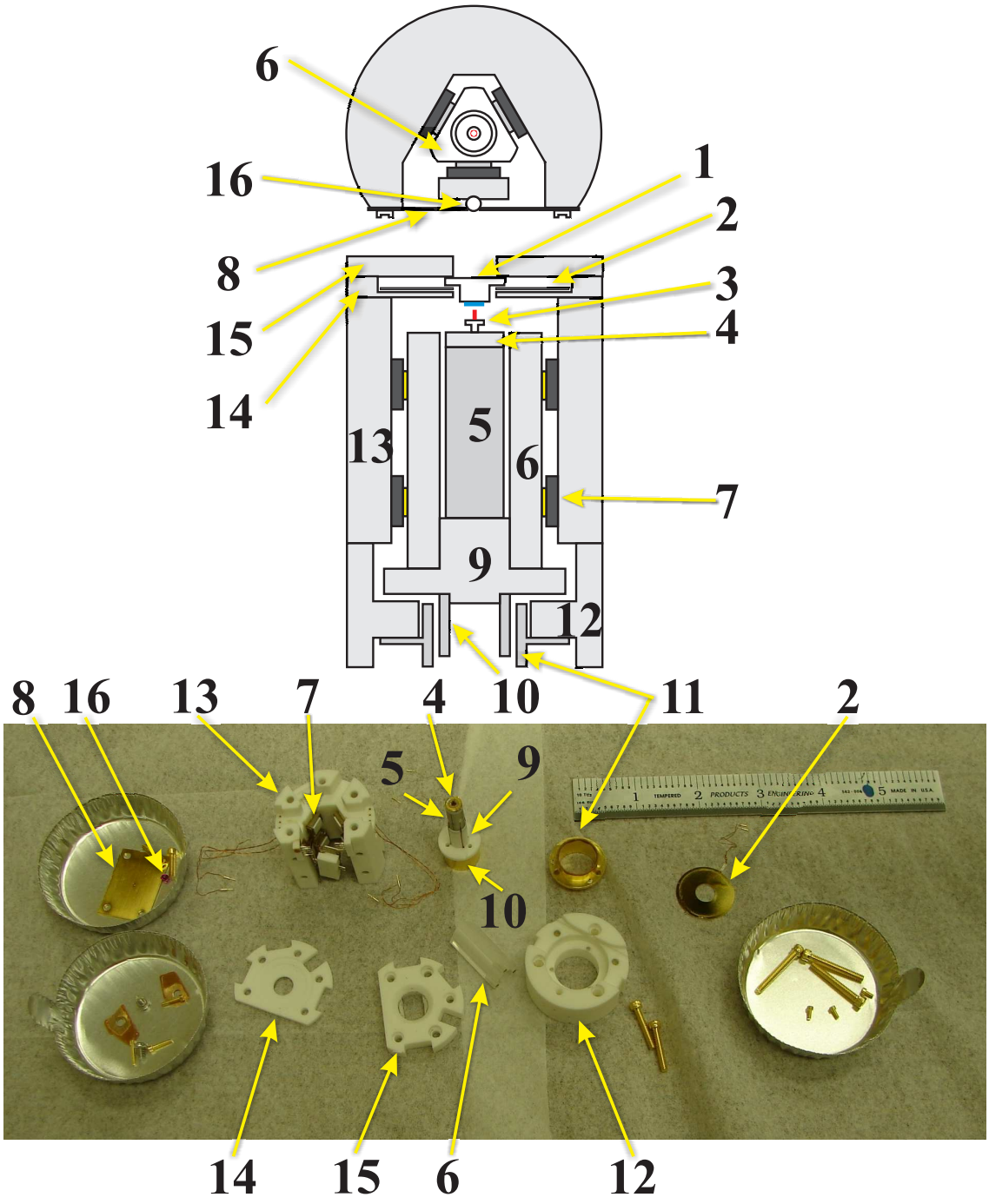

Figure 2.7: **STM Parts.** Part numbers are shared with Fig. 2.6. Additional parts (not visible in Fig. 2.6) include: 12). Macor base. 13) Macor body piece. 14) Spring plate holder. 15) Macor top piece. 16) Ruby ball.

This coarse approach motor using the walker was described in detail by Pan [17]. The coarse approach mechanism is briefly illustrated in Fig. 2.8. The prism is held in position by the static friction between the contact pads of the stacks and the prism surfaces. To "walk" a step, first a voltage is applied to one stack, causing it to deflect and slide downward along the surface of the shaft but the prism stays still because the static friction provided the other five stacks is larger than the kinetic friction provided by the motion. After an appropriate delay, the same voltage is applied to another stack, causing it to deflect and slide down while the other five stacks including the one just deflected keep the shaft in position. After all the stacks have been sequentially and independently deflected and slid downwards, the voltages on all stacks are ramped down simultaneously, as shown in the drawing. As a result, all the stacks relax to their normal shape together, thereby lifting the prism one step upward. Typical peak voltages and step sizes of our STM at 4.2 K are ~ 350 V and ~ 80 nm, respectively.

For each step, the sapphire prism will carry the scanner system with the tip at the top a step closer to the sample. At the same time, the capacitance of the capacitor will change since the inner capacitor plate (10) at the bottom of the scanner system will displace a step upward while the outer plate (11) bolted to the Macor base (12) remains still. By measuring the capacitance change, we are able to monitor the tip approach while the system is at 4.2 K enclosed in the dewar. See [16] for detailed calibration of the walker with capacitance.

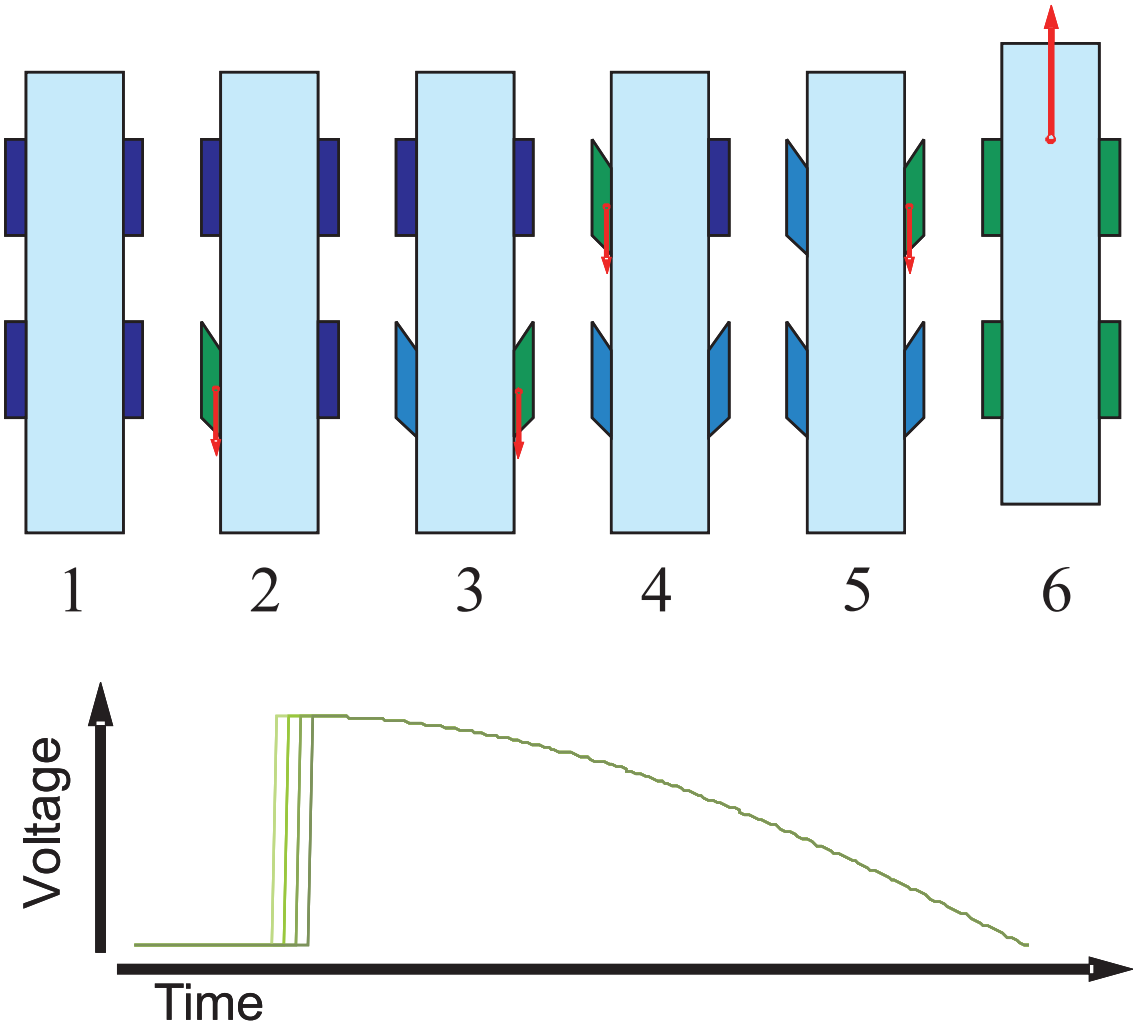

Figure 2.8: **The Walking Mechanism.** Six walkers are applied high voltages at different times by the designed voltage sequence. Each walker will side down the surface of the sapphire prism one by one. In the end all the voltages are ramped down to zero simultaneously causing the walks to push up the prism one step. The whole process is then repeated to move the tip which is attached to the prism toward the sample surface.

During the approach, the voltage on the piezo-tube scanner is set to retract it to the shortest position. Before each step is taken by the walker, the tunneling current is measured to check the distance between the tip end and the sample to make sure an additional step is safe. A voltage is applied to the scanner to elongate it and to extend the tip toward the sample by a distance that is larger than one step size. Meanwhile, the tunneling current is monitored with the bias voltage on. If the set point current (usually 0.1 nA) is reached during the elongation, the walking will be stopped, the scanner withdrawn and we have finished the coarse approach to the surface. Otherwise, another step would be taken. After the tip approaches, the capacitance is recorded as the capacitance at approach for reference. To start tunneling measurements we only need to approach with the scanner and render the control of the scanner voltage to the feedback loop.

The principle and calibration of the piezo-tube scanner used in our STM are well documented in [16]. It has a Z range at 4.2 K of 270 nm (much larger than the step size) with an applied V_z from -220 to 220 V. The scan range is $\sim 1.0 \times 1.0$ μm^2 in XY plane at 4.2 K.

Chapter 3

General properties of 2H-$NbSe_2$: a LTSTM study

In this chapter I will give an introduction to the material I used in this thesis work. The work in this chapter will provide examples of the operation modes of our STM.

3.1 Introduction

2H-$NbSe_2$ is a well-studied sample in STM experiments [18]. It is a layered material with rich physics. By simply cleaving off the top layers using, for example, a piece of scotch tape an atomically flat surface is immediately exposed and ready to be studied. This makes it an ideal sample for the testing and calibration of STM. Figure 3.1 shows a schematic diagram of the unit cell of 2H-$NbSe_2$. The exposed triangular lattice of the Se layer can be measured using a STM.

Other than the convenience, this material is also well-known for the coexistence of two interesting phases at low temperatures: charge density waves (CDW) and superconductivity. The transition temperature for the CDW, $T_c^{\mathrm{CDW}} = 32$ K, is higher than the transition temperature of superconductivity, $T_c^{\mathrm{SC}} = 7.2$ K. Since our LTSTM system usually operates at 4.2 K we are able to study both of them.

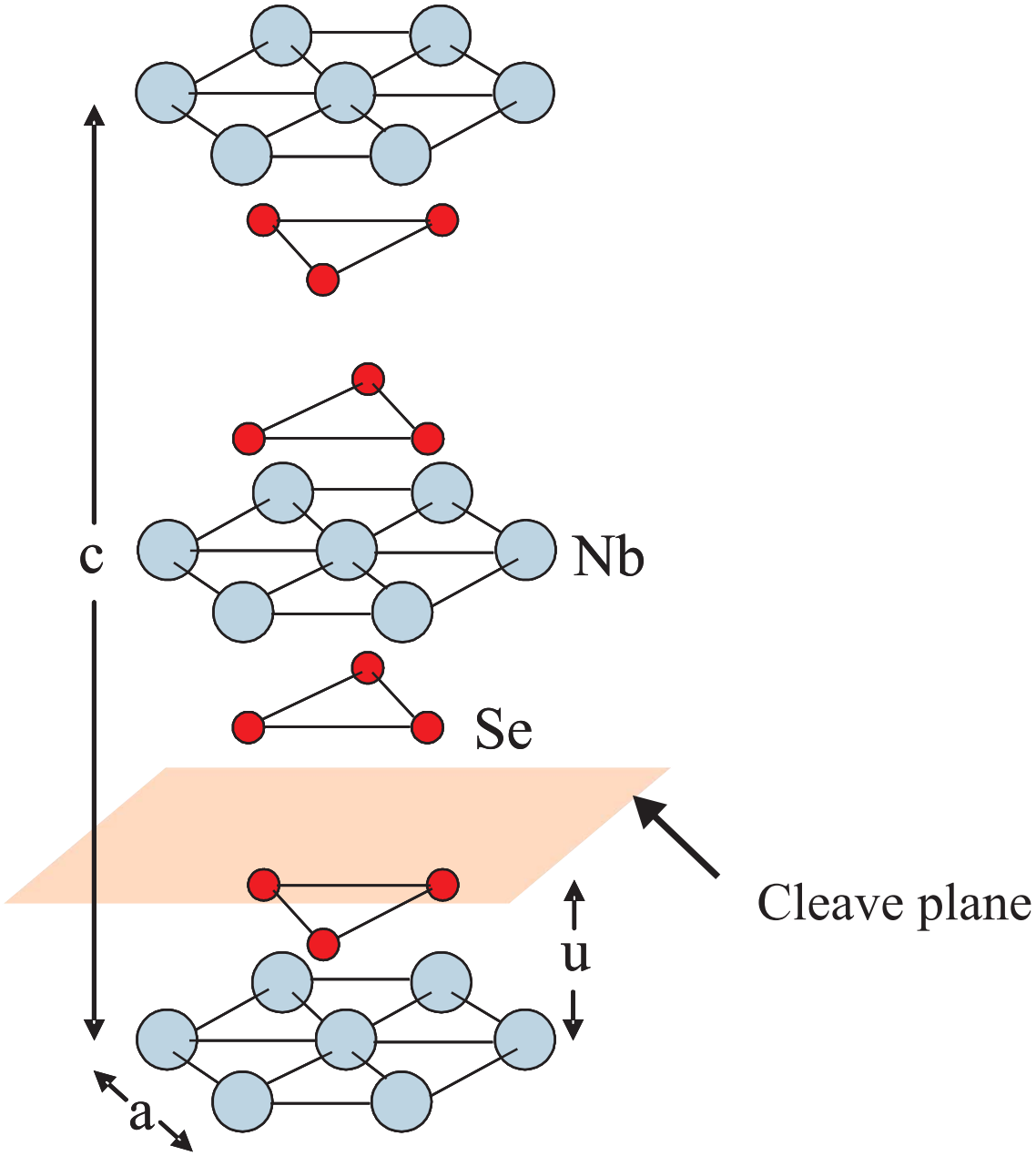

Figure 3.1: **Unit Cell of 2H-$NbSe_2$.** a=3.45 Å, c=12.54 Å, u=1.68 Å. The material easily cleaves between the two Se layers as indicated in the diagram, exposing an atomically flat surface. The triangular lattice of Se atoms on the surface can be detected by STM.

In the constant current topography mode, STM can clearly show the surface corrugation due to the CDW. As a type II superconductor, 2H-$NbSe_2$ in a magnetic field will manifest its superconducting vortex state in spectroscopic images. I will discuss all these observations made in our system in the following sections.

3.2 Topography Mode and Charge Density Waves

Figure 3.2 shows a 5 nm $\times$ 5 nm image on the cleaved surface of 2H-$NbSe_2$ as measured by STM in the constant current topography mode. Along the line cut, the height information is displayed in the panel below it. Clearly our STM has resolved the atomic corrugation on the surface. The lattice constant agrees well with the theoretical value. A charge density modulation is superimposed on the atomic profile. In the image, every third atom is brighter than the rest. This is usually explained as the evidence of the CDW present in this material.

Despite the 2D nature of the CDW as imaged, for simplicity here I will use a 1D model by Peierls [19] to explain the formation of the CDW. Details about the general theory and experimental evidence can be found in [20]. A periodic 1D atomic chain with its dispersion relation is schematically depicted in Fig. 3.3 (a). Assuming a linear dispersion around the Fermi energy E_F, in 1D electron gas theory it can be shown that the Lindhard response function [19], which controls the rearrangement of the electron charge density, will be divergent at $2k_F$:

$$\chi(q) \propto \ln \left| \frac{q + 2k_F}{q - 2k_F} \right|. \tag{3.1}$$

This divergence suggests the ground state of the electron gas is unstable at low

temperatures. It is important to notice that this so-called Peierls instability is related to the particular topology of the Fermi surface since the pairs of states in the electron-hole channel with the same energy and momenta differing by $q = 2k_F$ contribute most to the divergence. The existence of this topology is called Fermi surface (FS) nesting. Interestingly, another instability in the electron-electron channel with $q = 0$, *i.e.*, the famous Cooper instability would lead to a superconducting (SC) ground state at low temperatures. An energy gap is then opened up in the single particle excitation spectrum close to the Fermi level. By the very same argument, as shown in Fig. 3.3 (b) this gap-opening also applies to the CDW state due to the Peierls instability at low temperatures. Both novel ground states are consequences of the electron-phonon interactions between the electrons and the underlying atomic lattice. In the SC state, Cooper pairs are formed. In the CDW state, a spatial modulation of the charge density with a wavelength of $\lambda_{CDW} = \pi/k_F$ would occur. Also the reduction of the renormalized phonon frequency at $q = 2k_F$ to zero indicates a "frozen-in" periodical distortion in the underlying atomic lattice occurs below the transition temperature [20] as illustrated in Fig. 3.3(b).

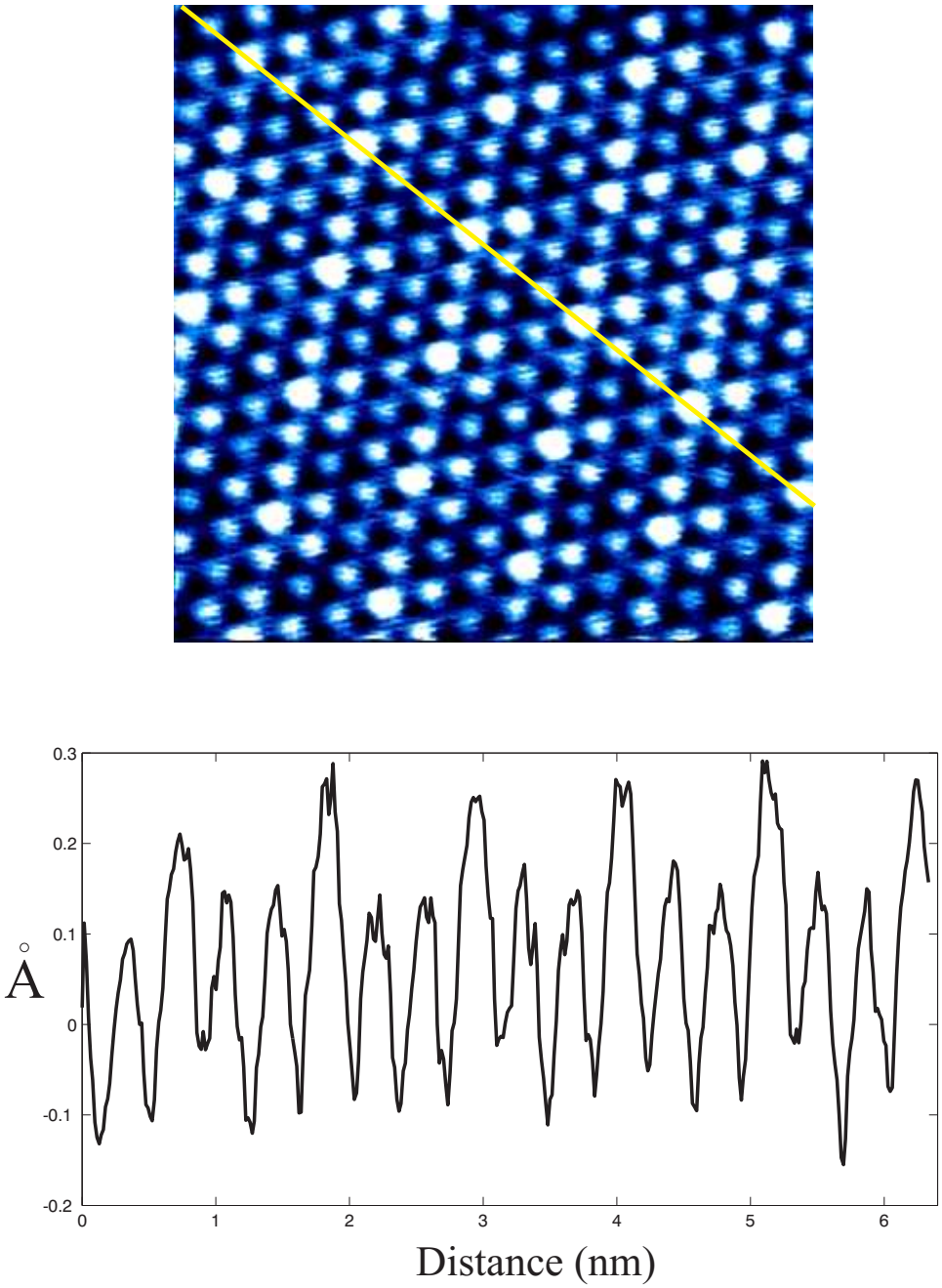

Figure 3.2: **STM Image of 2H-$NbSe_2$ in the Topography Mode.** ($I = 0.1$ nA, $V = 50$ mV, scan range 5 nm). Taken at 4.2 K, the image shows the profile of the atomic lattice with a clear 3×3 CDW signature. The panel below shows a height profile on a line cut in the image which quantitatively demonstrates the atomic corrugation and the CDW modulation.

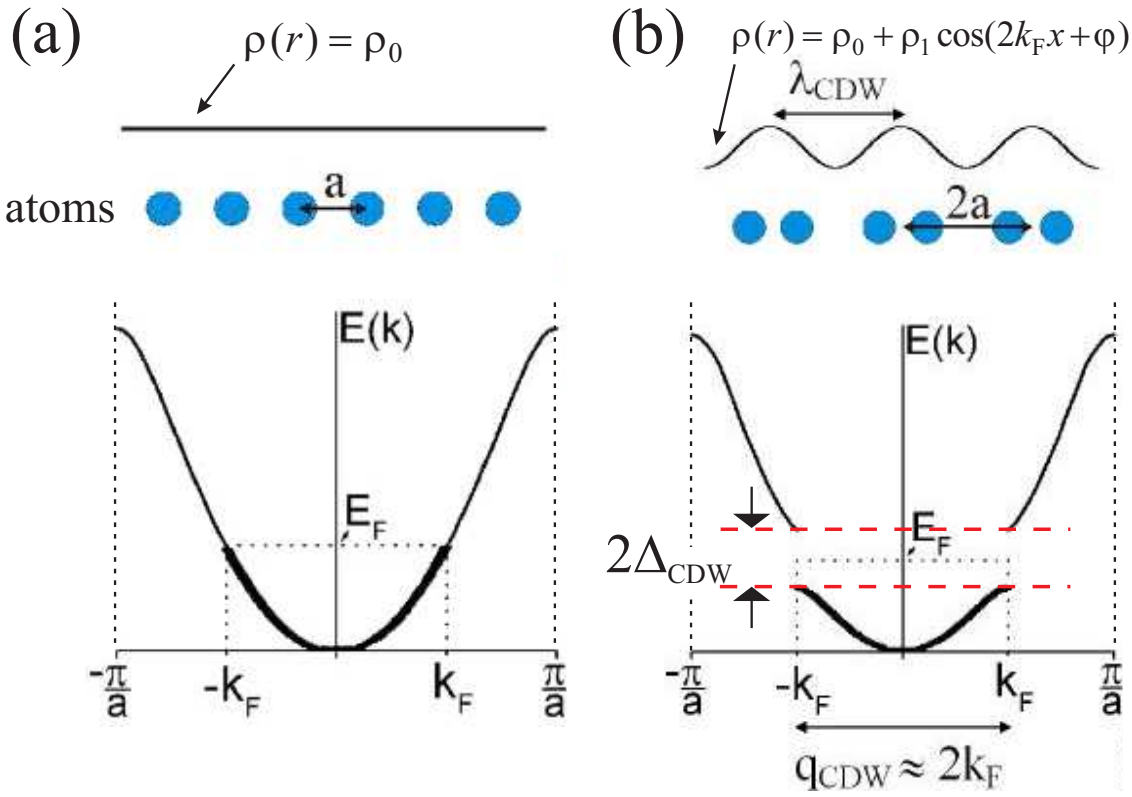

Figure 3.3: **Peierls Model of 1D CDW.** (a) is a 1D chain of metal atoms with uniformly distributed charge density in which the ground state of the electron gas is not stable at $T = 0$. A phase transition occurs at low temperature as shown in (b). An energy gap opens up in the excitation spectrum to lower the total energy of the ground state.The new ground state has a periodically modulated charge density and a distorted atomic lattice.

In real materials, the details of the electron-phonon and electron-electron interactions determine the specific thermal stability of the various phases in the system. Interestingly, in 2H-$NbSe_2$ the two phases coexist at our operating temperature, 4.2 K. The charge density waves are detected in the topography mode shown in Fig. 3.2. In general the CDW wavelength $\lambda_{CDW} = \pi/k_F$ will be incommensurate with the atomic lattice constant a. However, for 2H-$NbSe_2$ $\lambda_{CDW} \approx 3.03\ a$ and this is why we see a 3×3 pattern in the image. For weak CDW states like this one in 2H-$NbSe_2$, the underlying lattice distortion is too small for STM to detect. We will revisit this issue in Chapter 4.

3.3 Spectroscopy Mode and the Coexisting States

Another signature of the CDW and SC states is the energy gap in the excitation spectrum which is well manifested in the DOS measured by STM in the differential conductance spectroscopy mode. Shown in Fig. 3.4 is an averaged spectra over all the points in one image, enveloped by lower and upper bounds calculated from the standard deviation. The two gaps are marked and compared with theoretical values. For transition temperatures $T_c^{\mathrm{CDW}} = 32$ K and $T_c^{\mathrm{SC}} = 7.2$ K, the BCS relation [20] which is applicable to both cases leads to zero temperature gap values: $\Delta_{CDW} = 35$ mV and $\Delta_{SC} = 1.2$ mV. Within thermal broadening, our result agrees well with the theory. It's worth mentioning here that the peaks at the edges of the SC energy gap are well manifested in the spectrum and are a signature of the superconducting state.

Although the experimental results [21] agreed well with the theoretical picture of the CDW phenomenon in quasi-2D materials like 2H-$NbSe_2$, there are heated debates about the source of this novel collective state [22]. Since the possible nesting area of the FS in 2H-$NbSe_2$ is very small, the FS nesting being the major reason behind this phenomenon becomes disputable. On the other hand, the SC state is well studied for low-T_c, type II superconductors. The most striking feature of this state is the vortex phase which, very fortunately, can also be measured by a STM when the sample is in a moderate magnetic field.

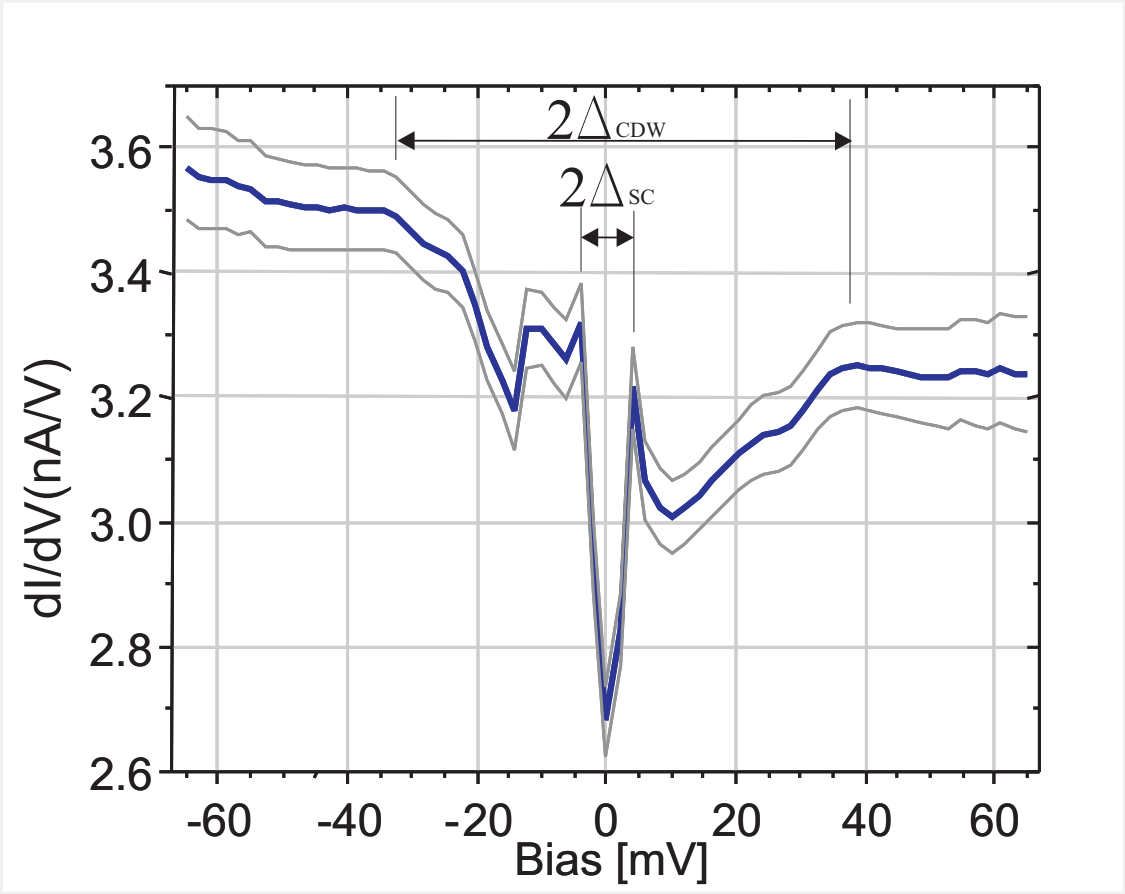

Figure 3.4: **Differential Conductance Tunneling Spectroscopy on 2H-$NbSe_2$.** A tunneling spectroscopy measured at 4.2 K shows the SC and CDW gaps near the Fermi energy. The result is averaged over an image. The center blue curve shows the averaged result and the two gray guiding curves shows the standard deviation. The modulation amplitude used by the lock-in amplifier is 2 mV. Tunneling condition $I = 0.4$ nA and $V = 35$ mV.

3.4 STS imaging and the Vortex State

I will introduce later in Chapter 5 the details of the vortex states in type II superconductors. In this section I will focus on the techniques we used to image the vortices. A type II superconductor, when subjected to a magnetic field H with a value between its lower critical field H_{c_1} and its upper critical field H_{c_2}, will allow the magnetic induction to penetrate in forms of flux lines each carrying a magnetic flux quantum $\Phi_0 = 2.07 \times 10^{-15}$ Wb as depicted in Fig. 3.5(a). These flux lines will modify the order parameter in the superconductor. The typical shape of the order parameter across the center of the flux line $|\Psi(r)|$ is shown in Fig. 3.5 (b). Also shown is the magnetic profile $B(r)$ which indicates that supercurrent circulates the center of the line. Due to this, these flux lines are also referred to as vortices. Note that at the core $|\Psi(r)| \rightarrow 0$, the superconductivity is destroyed and the material turns normal. As a result, the local density of states (LDOS) loses the signature of the superconducting state: the superconducting peaks at the edge of the energy gap. This enables the STM to detect the vortex state.

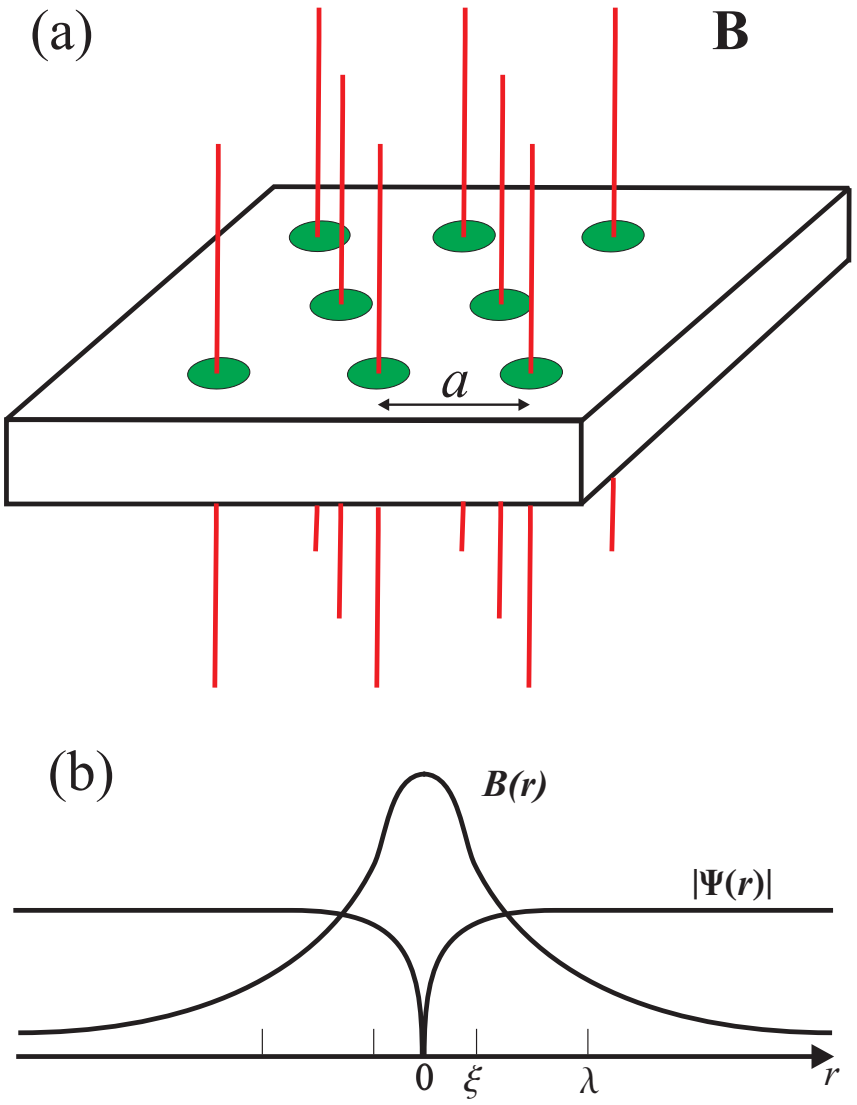

Figure 3.5: **Schematics of Vortex Lattice and Vortex Structure.** (a) Magnetic inductance penetrates into the superconductor in the form of flux lines each carrying a flux quantum $\Phi_0 = 2.07 \times 10^{-15}$ Wb . They organize as a flux line lattice at certain fields. The lattice constant is a function of the induction $a = \left(2/\sqrt{3}\right)^{1/2} (\Phi_0/B)^{1/2}$. (b) characterizes the structure of a single vortex. The superconducting order parameter $\Psi(r)$ is compared to the magnetic profile $B(r)$. It changes over a length scale of the coherence length ξ. Thus the diameter of the vortex core is defined as ξ. STM images the vortex core since it detects the variations of the DOS across the surface. In comparison, all other vortex imaging techniques measure $B(r)$ which has a length scale of the penetration depth λ.

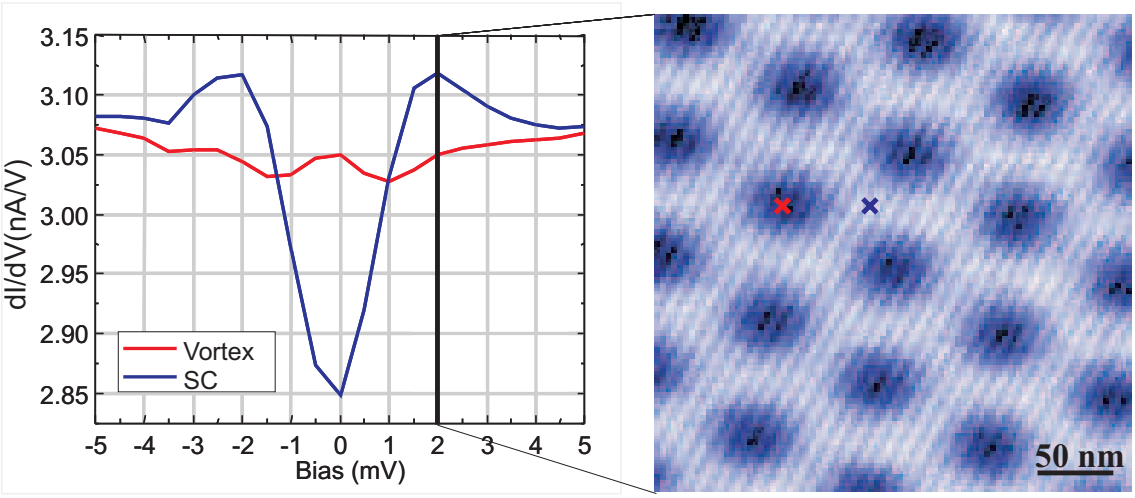

Figure 3.6: **Imaging Vortices by STM.** The STS imaging technique applied to the vortex system. STM detects different differential conductance spectra in the vortex area than in the superconducting area in the sample. In the plot on the left, the red (blue) curve is from the vortex area (superconducting area) as marked by a red (blue) cross on the image on the right. In STS imaging, the bias voltage is fixed at a value where the difference can be reflected in the contrast of the gray scale image on the left. The dark round-shaped disks are thus the cores of vortices in the sample. $V = 3$ mV and $I = 0.1$ nA for the image on the right. All data taken at 4.2 K.

On the left of Fig. 3.6 I show the two spectra taken by STM at different locations in the spectroscopy mode. The LDOS at the core of the vortex (red) is compared to the LDOS in the superconducting area (blue). It's obvious that the gap disappeared in the normal core area and the spectra differ very much across the gap. By fixing the bias voltage at 2 mV, the spatial variation of the LDOS at $E = E_F + 2$ meV can be mapped out using the single conductance imaging (or the STS imaging) mode. The gray scale image of vortices is shown on the right of Fig. 3.6. The contrast indicates the normal region has lower density of states than the SC region at this particular energy which is consistent with the values shown on the left. The profile of each imaged vortex portrays the distribution of the order parameter $|\Psi(r)|$ since the change of the $|\Psi(r)|$ at any location leads to the change of the DOS at the energies near the gap. Away from the center where it is destructed, $|\Psi(r)|$ recovers over a length scale ξ, the coherence length of the superconductor. Thus the vortex core is defined by the region around the center with a diameter 2ξ. For 2H-$NbSe_2$, $\xi \approx 12$ nm [23]. The vortex core profile is shown in the section A to B of the line cut in Fig. 3.7. The capability of imaging the vortex core gives the STM the advantage of higher resolution and higher applicable field over other imaging techniques such as bitter decoration [24], Lorentz microscopy [25], mageto-optical imaging [26] that all measure the magnetic field profile $B(r)$ with a length scale λ [27], the penetration depth which is usually $\gg \xi$ (for 2H-$NbSe_2$, $\lambda \approx 200$ nm [23]).

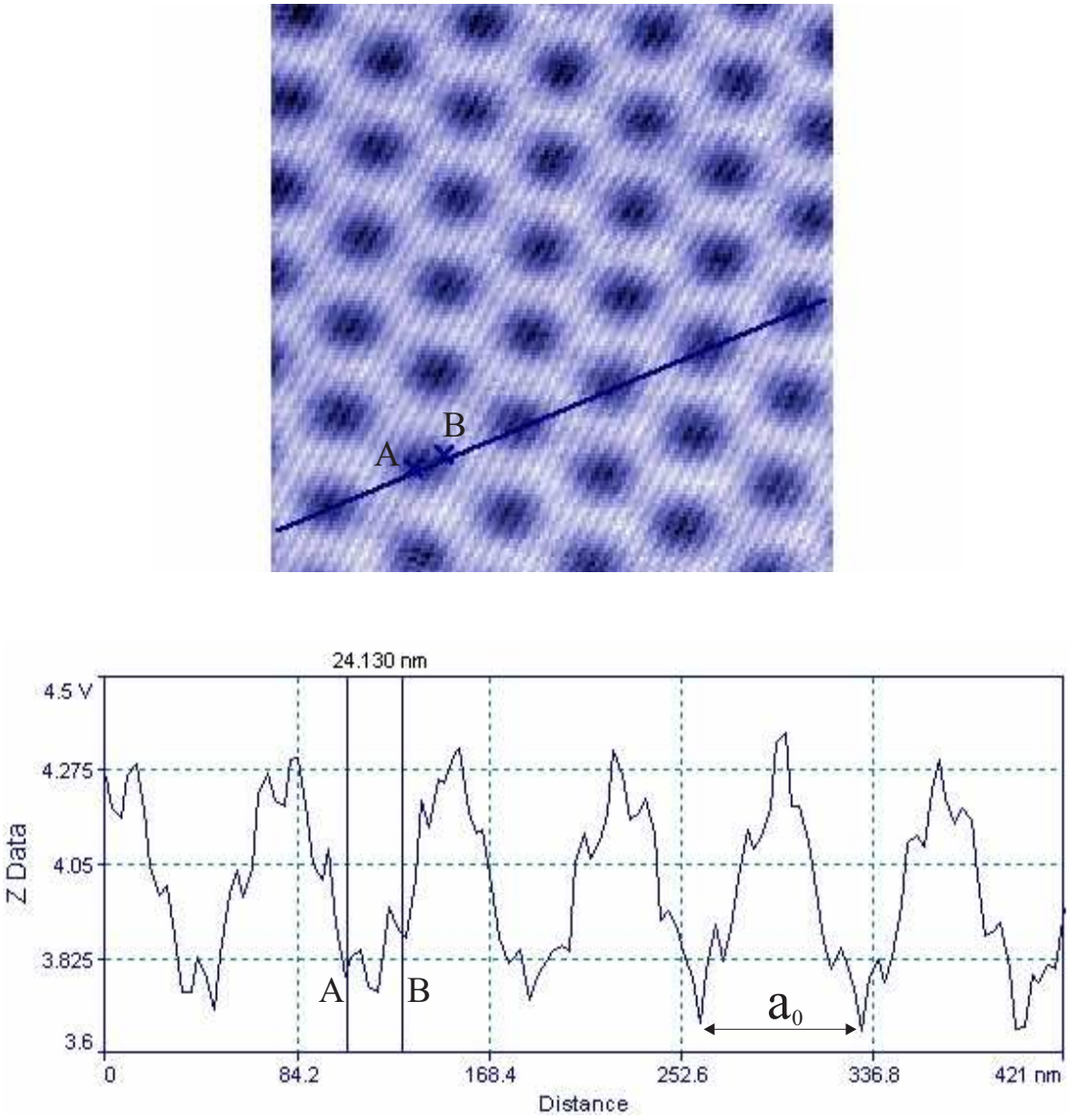

Figure 3.7: **Vortex Image Example.** Vortices imaged at $B = 0.5$ T. Image size 400 nm $\times$ 400 nm. Tunneling condition $I = 0.1$ nA, $V = 3$ mV, lock-in modulation amplitude $V_{mod} = 1$ mV, T = 4.2 K. The line cut below shows the DOS differences along the black line marked in the image along one lattice axis. A and B cut the core of a vortex. The measured core diameter 24.1 nm, is very close to $2\xi = 24$ nm. The lattice constant a_0 is measured to be ~ 68 nm comparing to the theoretical value $\left(2/\sqrt{3}\right)^{1/2} (\Phi_0/B)^{1/2} = 69.3$ nm.

Chapter 4

Observing a New CDW Around Defects Induced by Voltage Pulses and Steps

In this chapter I report the observation of a new CDW superstructure with $\sqrt{13} \times \sqrt{13}$ reconstruction as compared to the well-known 3×3 CDW superstructure in 2H-$NbSe_2$ which I described in Chapter 3. The observation was made around structural defects on the surface introduced by applying bias voltage jumps and pulses at 4.2 K. Multiple atomic layers inside the defects were also exposed and showed the new modulation of the CDW. This indicates a 2H to 1T phase transition locally for the $NbSe_2$ crystal structure. Two other interesting observations are also included: the disordered phase of this structure near the atomic steps and an anomalous distortion in the underlying atomic lattice revealed by STM images.

4.1 Introduction

Charge density wave (CDW) states in quasi-2D system such as transition-metal dichalcogenides continue to attract great interest [21, 28] especially with scanning tunneling microscopy (STM) techniques [3, 29]. 2H-$NbSe_2$ is a well studied example of this class of materials. As I reported in Chapter 3, clear 3×3 atomic modulation on the surface revealed by STM in the topography image and the energy gap in the differential conductance spectroscopy agree well with theories of CDW in quasi-2D

systems. This type of CDW is what is generally observed on the surface of the 2H (trigonal prismatic coordination) phase of dichalcogenides [29]. It was reported that there exists another type of surface modulation in Ag-doped 2H-$NbSe_2$ at room temperature [30]. A localized version of this modulation also exists in pure samples at room temperature [31] and 4 K [32]. This new CDW modulation exhibits a $\sqrt{13}\times\sqrt{13}$ structure which is instead only natural to the 1T (octahedral coordination) phase of dichalcogenides [33]. The mechanism of the formation of this new CDW in 2H material remains unresolved. Since there is no detailed data available for accurate characterization, a better understanding of this transition calls for a closer look at the modulation.

In this chapter I will show that we can create this new type of modulation by a controlled tip-sample interaction at 4.2 K and examine the atomic structure of the modulation in detail by STM. By applying a sudden change in the bias voltage, or using a short period voltage pulse superimposed on the bias voltage, we can create a "pit", a local structural defect, on the atomically flat surface of 2H-$NbSe_2$. The size of the defect is on the order of 100 nm in diameter and 10 nm in depth. A clean $\sqrt{13}\times\sqrt{13}$ superstructure is found around the edge and inside of the defect. This method is reproducible and the new structure is stable during scanning at 4.2 K in our system. We are able to characterize it both on large and atomic scales. The voltage jump method was used to generate similar surface modulation in 2H-$TaSe_2$ [34] and it was proposed that only the top Se layer had shifted. Here by exposing the layers lower than the top one, we clearly observed a 3D structural transformation instead of only a top layer shift.

Other than those that are common to the CDW state in 1T systems, we observed two novel features that are unique to this local modulation. The first one is the order/disorder phase separation of the new modulation. This disordered phase was first seen in the silver doped case [30]. But it hasn't been reported in the local case as well as in the 1T system. This new phase suggests a localized CDW state. The second feature is the anomalously large atomic lattice distortion revealed by examining the atomically resolved images in the ordered region. The distortion in the unit cell of the $\sqrt{13} \times \sqrt{13}$ superstructure found is much larger than in the 1T case. This is the first time, to the best of my knowledge, that the detailed periodic structural displacement (PSD) of the CDW created locally is revealed by STM. We propose that local heating generates this new modulation. It is a similar process to spot welding [35] where the probe is brought close to the metal so the resistance is small and the heating is localized. We argue that a short pulse can generate enough heat locally to raise the temperature to induce a phase transition. In Sec. 4.2, I will describe the experimental method and the general results. The two observations mentioned above will be discussed in Sec. 4.3 and Sec. 4.4. I will summarize in Sec. 4.5.

4.2 Defect Structure and the New Modulation

A pristine single crystal of 2H-$NbSe_2$ was cleaved at room temperature in a high vacuum of about 10^{-7} mbar. Then it was transferred to the STM in the LT chamber at 4.2 K within a few minutes. We prepared the chemically etched

tungsten tip in the STM before transferring the sample by field emission against a single crystal of gold. The 2H phase of the crystal was confirmed by the observation of the 3×3 modulation on the atomically resolved surface. We used two different methods to generate the structural defect on the surface. In the first method, with the feedback on, we generated a short bias voltage pulse with a duration of 100 μs and an amplitude of 3-5 V. The bias voltage was set to 50 to 100 mV with a tunneling current of 0.1 nA before the pulsing. We also used another method in which we simply stepped the bias voltage from 3-10 mV to 5-10 V while scanning with the feedback on. This sudden change of bias voltage proved to be a more reliable method. We find that the critical voltage depends on the initial tunneling voltage. For an initial voltage of 3 mV, the critical voltage is ~ 5 V. We also tried the method of mechanical contact. We turned off the feedback after scanning and pushed the tip into the surface by increasing the voltage on the piezo-tube scanner. No $\sqrt{13} \times \sqrt{13}$ modulation was found in the vicinity of the the defect created by this method. This excludes mechanical contact as a reason for the formation of the new CDW. All the images shown in this chapter were taken with a tunneling current of 0.1 nA and with bias voltages in the range of 100 mV to 300 mV.

Figure 4.1(a) shows the image of a defect with a diameter of 120 ± 10 nm and a depth of ~ 13 nm which was observed after a voltage jump. This is a typical example of the defects made by either method. In the figure we can see that the layered structure is exposed. In contrast to the flat region on the left, the new modulation appears corrugated around the edge and the inside of the defect. Figure 4.1(b) shows the side of another defect. The new modulation with lattice constant

and corrugation larger than the usual 3×3 modulation is clearly present in this image. It appears on all the atomic steps which were exposed by the the tip-sample interaction. In Fig. 4.1(c), taken at the center of a defect, the modulation is also exhibited at the bottom layer. Plotted in (d) is the value of heights along a line cut in (c) marked by the black line. The heights of layers are measured to be 0.65 ± 0.05 nm. This indicates that they are all Se layers, for the distance between the two Se layers in the 2H-$NbSe_2$ crystal where it can be easily cleaved, is $\frac{1}{2} \times c = 0.636$ nm. Here c is the lattice constant of the crystal in the z direction. 2H-$NbSe_2$ crystal is composed of stacks of sandwich structures with two Se layers on the outside and one Nb layer on the inside (see Fig. 3.1 for details). The bonding between the Se-Nb layers within the sandwich is covalent while the bonding between the stacks is of van de Waals type. The crystal is cleaved between the stacks where the bonding is weak and the Se layers are exposed as the top surface. Our data show that the top Se layer of each stack is exposed in the defect. Height measurements in (a) and (b) also confirm this result. They are integer number times of $\frac{1}{2}c$. A simple calculation shows the typical depth of these pits is about 20 stacks. I believe this method is also applicable to other layered materials such as some of the cuprate high T_c superconductors and graphene samples to create a localized anomaly or expose the lower layers.

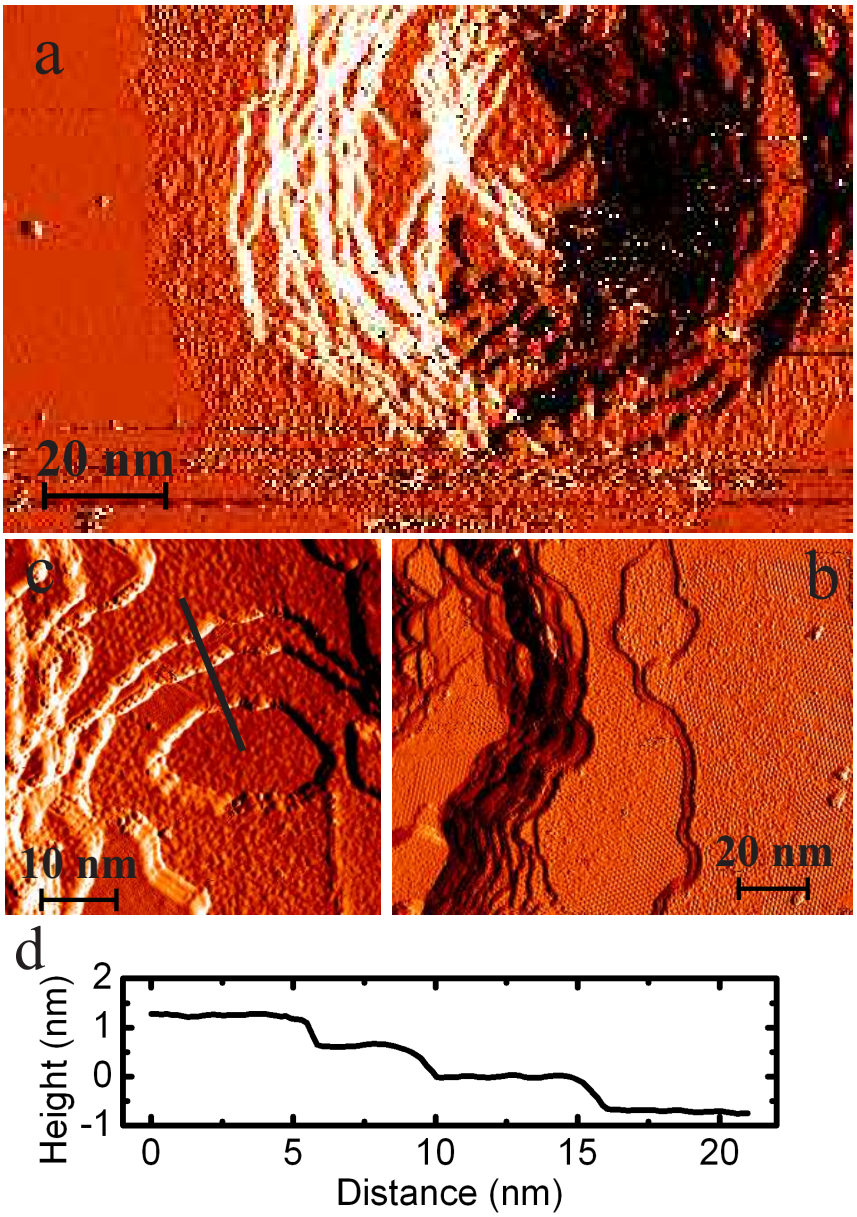

Figure 4.1: **The Defect and Its Vicinity.** The defect created by bias voltage jump. The electrons were moving from the tip to the sample. All images were acquired in the topographic mode. $I = 0.1$ nA and $V = 100$ mV. (a) The topographic image of the defect. The rough areas in the image are filled with the new CDW modulations, the flat and smooth area surrounding the defect has the regular 3 CDW superstructure on it. An interface image of these two areas are shown in Fig. 4.2. (b) is a current image shows the topographic profile of the side of a defect. CDW superstructures in form of triangular lattices are observed on each sandwich layer exposed. (c) The current image shows bottom of a defect with the new modulation. (d) shows the line cut made in (c). The heights of layers indicate that the new CDW exists on each Se layer exposed.

To examine the differences between the two CDWs, in Fig. 4.2(a) we zoom in to the interface area. On the left we observed the regular triangular lattice of Se atoms with the signature 3×3 CDW. On the right, the new modulation forms a triangular lattice with a lattice constant of 1.25 nm ($=\sqrt{13}a$, $a = 3.46$ Å) and a rotation of 13.9° relative to the atomic lattice. As shown in Fig. 4.2(b) the z deflection from the deep minima to the maxima of the new modulation is much larger (2.1 ± 0.2 Å) than the regular 3×3 structure (0.3 ± 0.1 Å) on the left. This large deflection is similar to what was observed on 1T-$TaSe_2$ [29]. This indicates a large charge transfer to the center atoms caused by the new CDW. In contrast to the small charge transfer and z deflection in the 3×3 area, this provides evidence that this new modulation is generated by a different source. Also similar to 1T-$TaSe_2$ and 1T-TaS_2, the underlying atomic corrugation is difficult to image in this area due to the large $\sqrt{13} \times \sqrt{13}$ corrugation. The atoms at the interface form a rectangular structure as indicated by the connected line on atoms in Fig. 4.2(a). As emphasized by Zhang *et al.* [34] the rectangular structure is a natural interface between the 2H and local 1T stack. Note that the interface of the two CDWs is usually straight and along the atomic lines, but the edges of the defects as illustrated in Fig. 4.1 are not. This difference indicates that the transformation is 3D. The new modulations on the lower layers extend to the area underneath the layer on top of it, not just on the area exposed. The features mentioned above are similar to the observation made on 2H-$TaSe_2$ [34]. The difference here is that a pure 1T crystal of $NbSe_2$ does not exist so there is no experimental data on the electronic and lattice structure of that crystal to compare.

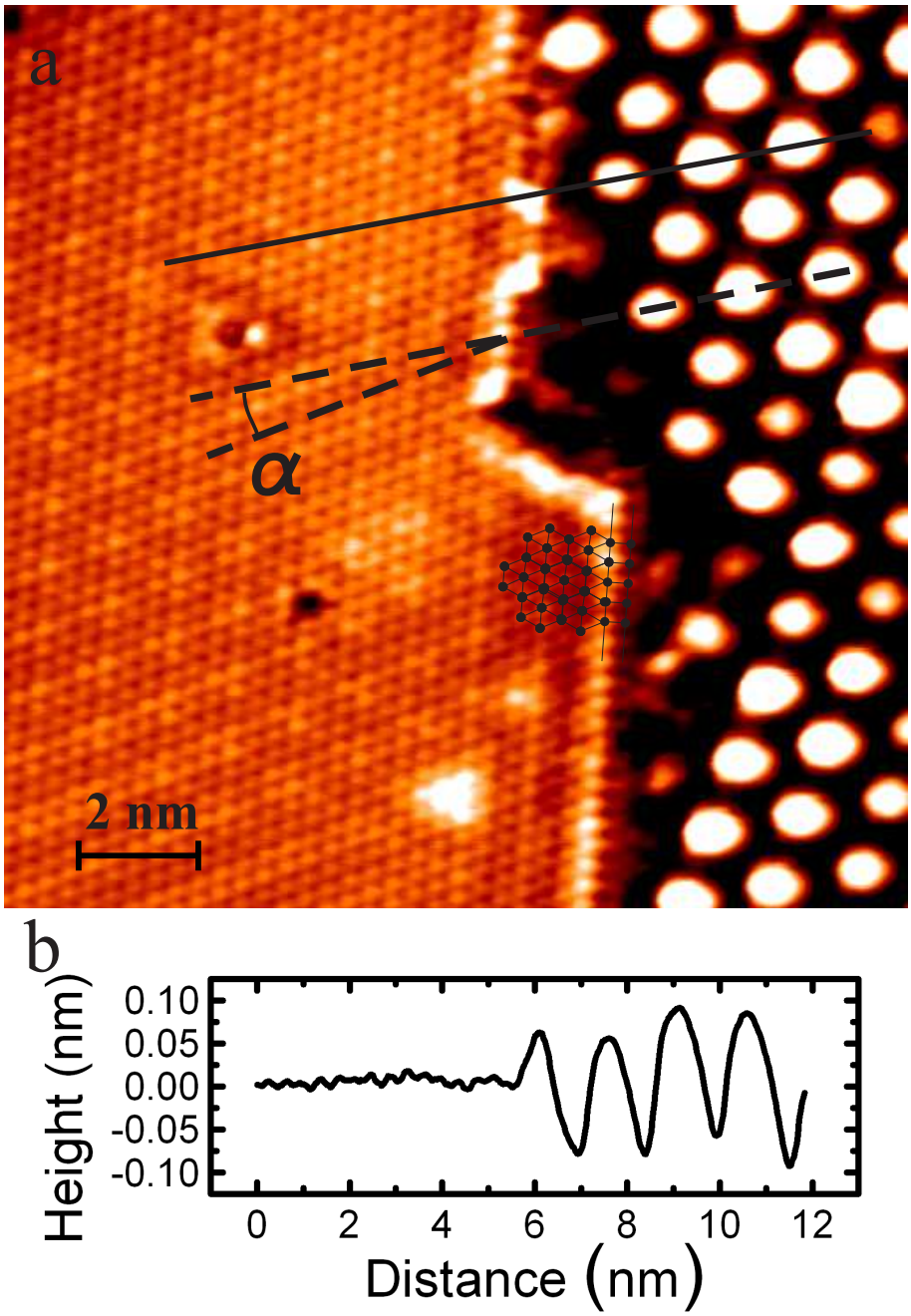

Figure 4.2: **The Interface of the Two CDWs.** The interface between the 3×3 CDW and the $\sqrt{13} \times \sqrt{13}$ CDW exposed. In (a), on the left shows the typical atomic lattice of the Se layer and the 3×3 CDW signature. On the right the big bubbles are the new modulation with a $\sqrt{13} \times \sqrt{13}$ construction. The lattice of the new CDW is rotated at an angle α with respect to the underlying atomic lattice. α was measured to be 13.9°. The atomic structure at the interface is illustrated by the lattice lines drawn upon the bright atom signals. It shows a rectangular interface lattice. (b) is the height measurement on the line cut across the interface in (a). Image was captured in the topographic mode at 4.2 K with $I = 0.1$ nA and $V = 100$ mV.

These observations demonstrate that the impact of the voltage jump or pulse can affect many layers from the surface and probably to the regions even lower than the bottom layer that is exposed. This new evidence contradicts the top-layer shifting scheme proposed by Zhang *et al.* [34]. Also the new CDW appearing on each Se layer suggests this is a 1T phase of the $NbSe_2$ instead of the 4Hb phase as proposed by Komori *et al.* [32]. This is consistent with theoretical calculations [36]. Here I propose a 3D structural transition from 2H to 1T in the area affected by the tip-sample interaction. Figure 4.3 shows the structural difference between these two phases. During the transition, the top and bottom Se layer of the 2H lattice both shifted as illustrated in the figure. Here I used the common notations in the description of close packing structures of an atomic lattice [37]. The top layer shifted from position B to C and bottom from C to B. The interface of the two lattices with CDWs is visualized in Fig. 4.2(a). In what follows I will refer to the nano-size affected 3D area as the nanocrystal [34].

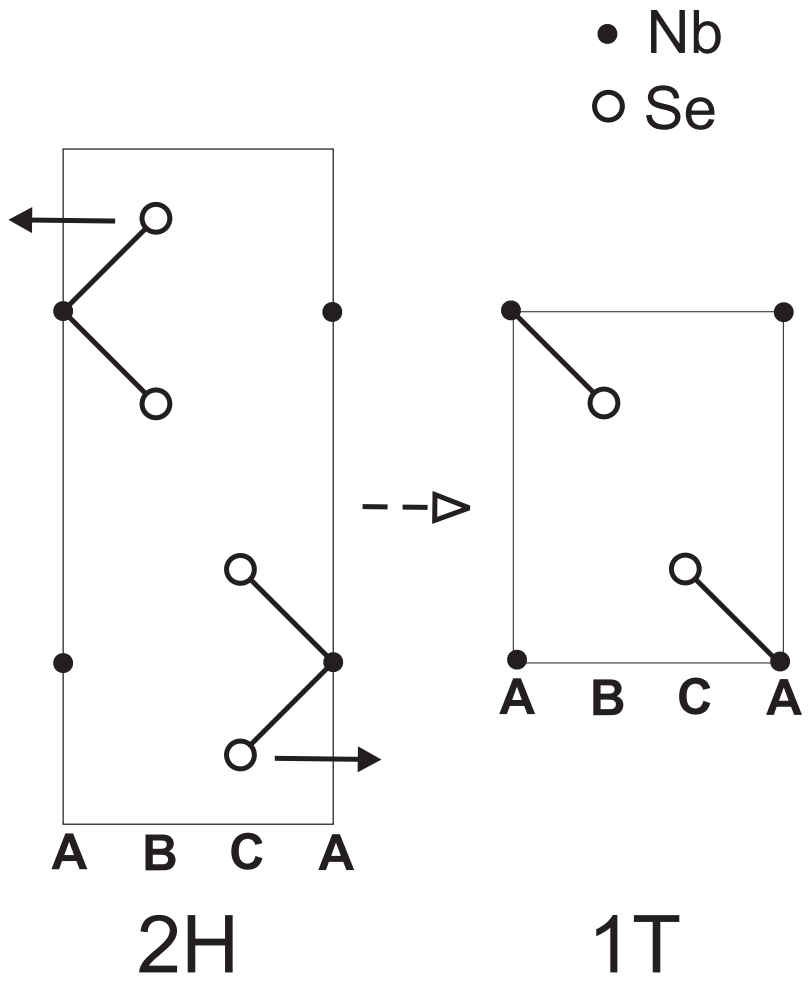

Figure 4.3: **The Lattice Transition from 2H Phase to 1T Phase.** Section $(11\bar{2}0)$ of the unit cells of 2H and 1T lattice are shown. The transition happens when the top and bottom Se layers both shift.

I speculate that the pulse generated heating locally transformed the nanocrystal to 1T and the size of the crystal is a result of the heat diffusion. It is known that 2H-$NbSe_2$ transforms to 1T phase at 980 K [38]. Several models have dealt with the steady state temperature of the local heating problem of STM on metal surfaces [39, 40]. Following Flores *et al.* [40], I calculate the steady state temperature $T \sim \frac{W_{e-h}}{2\pi r K_s} = 750$ K when $V = 5$ V and $T \sim 1555$ K ($T \propto V^4$ in the model [40]) when $V = 6$ V with tunneling resistance $R = 3 \times 10^7\ \Omega$ ($V_{bias} = 3$ mV, $I = 0.1$ nA before voltage jump). Here W_{e-h} is the power dissipated through electron-hole pair generation, K_s is the reduced surface thermal conductivity. While this model might not be completely accurate for this situation, it shows that the heating is in the right range. This scheme can also explain the small size effect of the experiment of Zhang *et al.* [34] since the temperature is dependent on V^4 and the size definitely depends on the center temperature of the diffusion process. A more sophisticated model like that for spot welding [35] and the direct measurement of the junction temperature are desirable to understand fully the process of heat generation and clarify the reason behind the creation of the defect. Similar to the spot welding process, the nanocrystal was created by the heating and then it was quickly quenched in the 4.2 K environment so the transition became permanent locally. There are also several other possible explanations, however. Mechanical contact was ruled out as I mentioned before. Electron assisted surface atom sublimation [41] is also not likely because the threshold voltage does depend on the resistance in this case. Sublimation could be part of the process creating the "pit" structure but not the nanocrystal.

4.3 Disordered Phase of the New CDW

One of the observations is the order/disorder phase separation of the modulation as illustrated in Fig. 4.4(a). It is a 97 nm by 97 nm topographic image taken in an area surrounded by 3 defects made by voltage pulses. The top defect is partially shown in the image and the left and right defects are out of the field of view. Regions of the modulation that show different orderings are marked by capital letters A to E in Fig. 4.4(a) and also in the Fourier transformed image Fig. 4.4(b). E is the region where the top layer remains intact and has the atomic and 3×3 CDW signature. It is very easy to identify the ordered regions A, B and C of the $\sqrt{13} \times \sqrt{13}$ modulation in (a) where triangular lattices with different rotations were formed. This is also a well-known feature of the commensurate phase of the CDW state in 1T systems [33, 42]. The different rotations are clearly shown in (b). We used select-filtering method to identify the real space counterparts of the 3 groups of 6 symmetric points in (b). B and C correspond to the α-rotated and β-rotated area where the CDW lattice rotated 13.9° counter-clockwise and clockwise respectively relative to the atomic lattice. The rotation of the A phase is 30° more clockwise. It has never been identified in a 1T system. It is not the satellite spot of the incommensurate phase of CDW in 1T [33] since it has the same wavelength as B and C. Further work is needed to understand the formation of A phase.

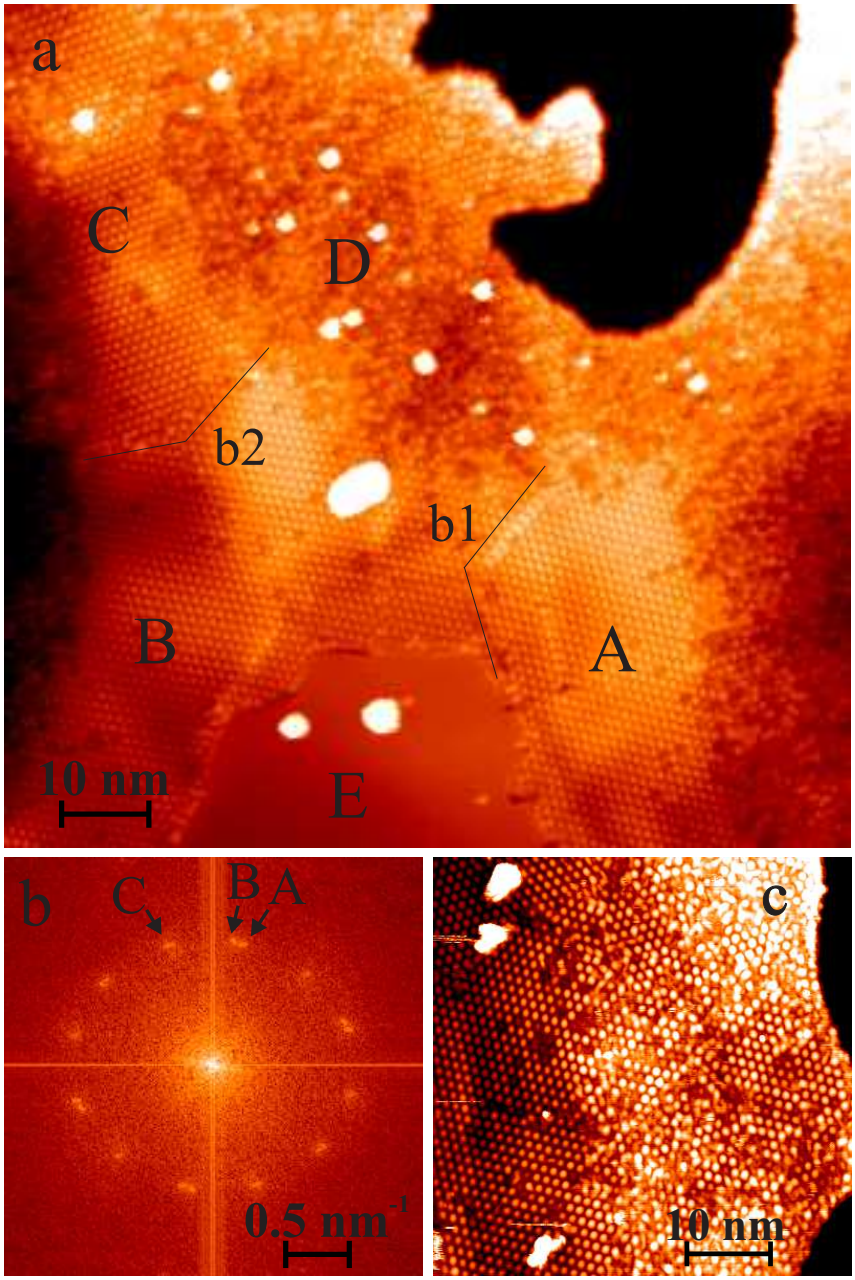

Figure 4.4: **Ordered and Disordered Phase of the New Modulation.** ((a) shows a 97 nm × 97 nm scan with different regions identified as different phases of the new modulation. The regions are indicated by A, B, C, D, E respectively (see text). b1 and b2 are two domain boundaries that can be easily identified by checking the mismatch of the lattice structures. The image was taken in an area on the surface surrounded by 3 defects, on the left, right and the top. Only the irregularly shaped defect on the top is partially shown (dark area). (b) is the Fourier transformed image of (a) showing peaks (bright spots) for different ordered regions corresponding to those indicated in (a). (c) is another example of the disordered phase (right) and the ordered phase (left). (a) and (c) were captured in the topographic mode at 4.2 K with $I = 0.1$ nA and $V = 100$ mV.

The domain sizes of the three phases are on the order of 50 nm^2 which are much smaller than those observed in 1T systems [42]. Due to their small size, I was able to image them all and their boundaries as indicated by lines b1 and b2 in Fig. 4.4(b). The defect or missing sites of the CDW are also frequently observed as we can see from Fig. 4.4(a).

As illustrated in Fig. 4.4(a), a disordered region D lies between the ordered regions and the defect. In this region, the wave feature of the modulation is destroyed. The corrugation still has the same amplitude as in the ordered regions, but the "bubbles" are not periodic as in the ordered regions. In some areas the distribution is rather random. The random feature of area D is also captured in Fig. 4.4(c) where a 50 nm by 50 nm topographic image of an area close to a pit shows the order/disorder interface. In (c), the disordered region consists of randomly distributed locally ordered plaquettes compared to D in (a) which has more single "bubbles" randomly distributed. I believe this could be additional evidence of local heating by the voltage pulse. The radial arrangement of the defect, the disordered phase and ordered phase is an effect of the diffusion of the heating process. The temperature at the center is the highest and enough to remove the material. The next is the disordered phase where the temperature is high enough to melt the CDW phase. The third is the ordered phase where the temperature is above the structural transition temperature but below the melting temperature of CDW. The last circle is the normal 2H region where the temperature is below the structural transition temperature. Since the pulse heating happens very fast and the environment is at 4.2 K, a quenching process similar to the spot welding of metals [35] happened and

left us the irreversible result of the nanocrystal.

The disorder and the CDW defects suggest the CDW state in this system can be localized. The localization of the CDW was predicted by McMillan on 2H-$TaSe_2$ [43]. In his theory the coherence length of the localized CDW could be as small as the lattice constant so that the unit cells of the CDW superlattice can be treated as independent local modes with intercell interactions. Long range order can be broken down at the phase transition. This physical picture at the transition is similar to what happened in area D in Fig. 4.4(a) and (c). It is unlikely to be caused by the impurities or vacancies in the layered lattice because they are expected to be evenly distributed so the separation of the ordered and disorder region would not be clear. One could argue that the lattice structure near the defect is completely destroyed, but this fails to explain why there still exists local CDWs, *i.e.*, the randomly distributed "bubbles". Apparently, more theory and further experiments are needed to study this interesting phase.

4.4 Periodic Structural Displacement of the New Modulation Revealed

The second feature in our observation is the atomic structure of this modulation. As in the 1T case, it is also difficult to obtain atomically resolved images of the new modulation [33]. Figure 4.5 shows one of the best we have acquired. The tunneling current and bias voltage we used are 0.1 nA and 100 mV, respectively. The reason we were able to obtain atomic resolution in this image (as compared

to Fig. 4.2 in which similar parameters were used) is due to the tip state as explained in [33]. Fig. 4.5(a) is a 20 nm by 20 nm topographic image taken at the interface which shows the regular 3×3 part on the left and the atomically resolved $\sqrt{13} \times \sqrt{13}$ part on the right. The insert is the Fourier transformed image to illustrate the symmetry of the atomic order (the outside hexagon) and the order of the new modulation (the inside hexagon). Note that the 3×3 modulation is very weak compared to the other two so there is no apparent bright spot for it in the Fourier transformed image. From the geometry we can confirm that the new modulation follows the typical symmetry of the CDW in the 1T material [33], a Star-of-David reconstruction and in this case an α rotated phase. A closer look at the real space image of the new modulation in Fig. 4.5(b) reveals the actual construction of this modulation which is quite different from the usual 1T case despite all the similarities we have discussed.

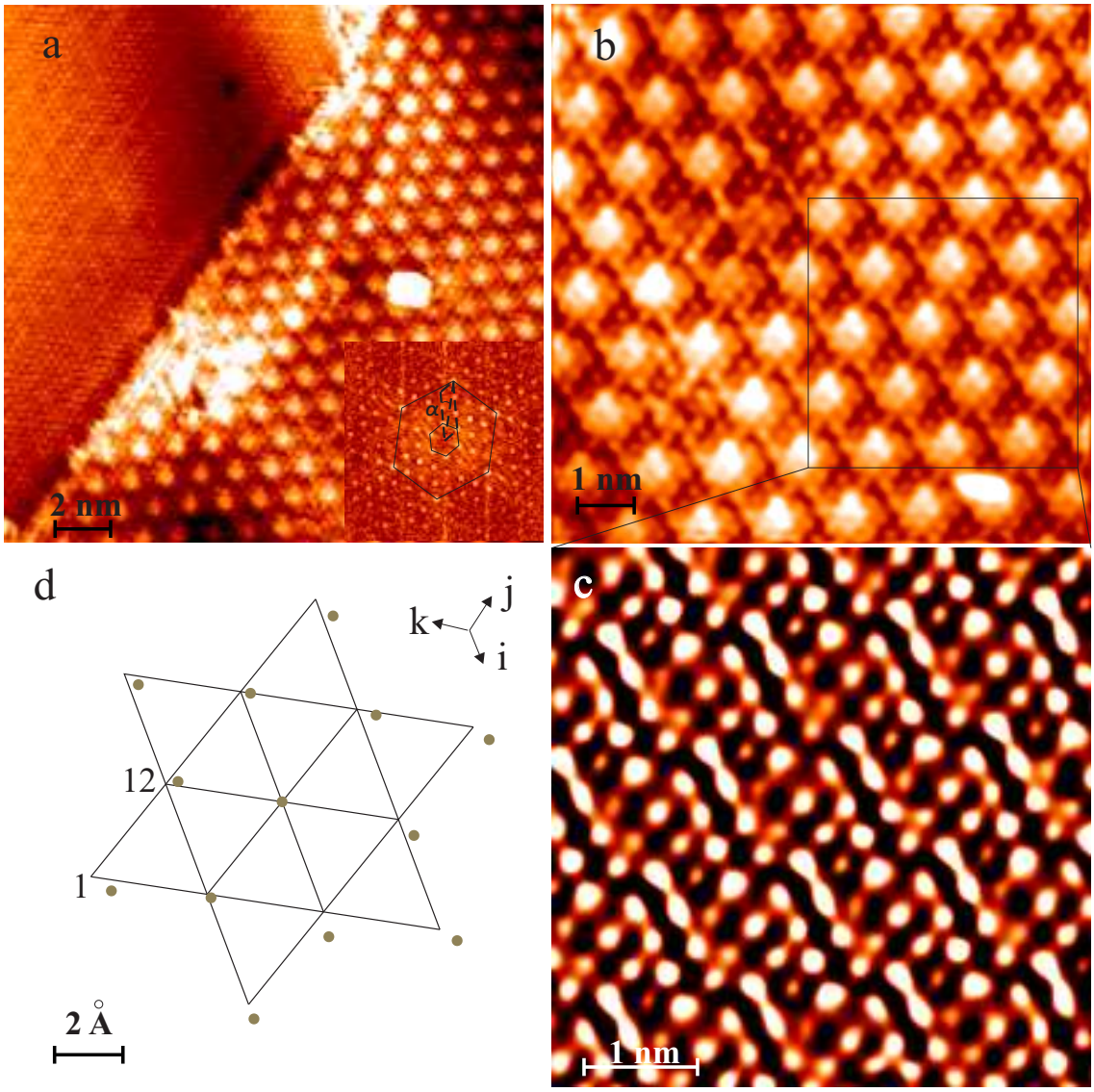

Figure 4.5: **Atomically Resolved Images.** (a) shows the interface of the 3×3 CDW and the $\sqrt{13} \times \sqrt{13}$ CDW. Insert is the Fourier transformed image. (b) zoomed in on the new modulation part and shows the details of the modulation structure. (c) shows the underlying atomic lattice by filtering out the CDW ordering in (b). (d) is the measured distortion in a Star-of-David unit cell. We kept the same orientation as in (c). i, j, k are directions of the three CDW vectors. (a) and (b) were captured in the topographic mode at 4.2 K with $I = 0.1$ nA and $V = 100$ mV.

In order to reveal the atomic construction of the new modulation, I zoomed in to the marked area in (b) where there is no defect and removed the Fourier component of the $\sqrt{13} \times \sqrt{13}$ order by Fourier filtering. The real space image after the process is illustrated in Fig. 4.5(c). One feature we can immediately notice is the asymmetry of the distortion of the atomic lattice. To measure the distortion I first processed the image by center of mass method [44] to find the position of each atom. Then I took the atom with highest corrugation (or "maximum point") of the $\sqrt{13} \times \sqrt{13}$ modulation as the center of the modulation and treated the closest 12 atoms to each center as the other members of the unit cell of the Star-of-David reconstruction. After this I constructed the regular lattice with no distortion of all the atoms in the image by fixing the positions of the center points. The distortion is calculated as the difference between the measured position of each atom and the corresponding one on the regular lattice. So each unit cell has 12 distortion vectors for the 12 members except the center. I plotted the averaged results in Fig. 4.5(d). The connected lines show the constructed regular lattice and the round dots are the average positions of the other 12 atoms in the unit cell. The atoms are numbered counter-clockwise with the first and last one indicated in the plot. The distortions are not symmetric around the center of the cell. The atoms near the interface of the two CDWs are pulled closer, and the atoms near the defect are further apart. This is different from what was observed for CDWs in 1T systems where the distortions are usually symmetric [21]. The asymmetry of the distortion is obviously exposed in the plot.

	1	2	3	4	5	6
d_i ($\AA$)	0.62	0.14	0.47	0.77	0.50	0.62
d_j ($\AA$)	0.03	-0.01	-0.25	-0.50	0.05	-0.10
d_k ($\AA$)	0.65	-0.13	-0.22	-0.27	-0.54	-0.51
	7	8	9	10	11	12
d_i ($\AA$)	0.53	0.36	0.66	0.15	0.45	0.05
d_j ($\AA$)	-0.02	0.21	-0.09	0.14	0	0.28
d_k ($\AA$)	-0.51	-0.57	-0.57	-0.29	-0.45	-0.34

Table 4.1: The distortion vectors of the unit cell in Fig. 4.5 (d). The error bar is 0.08 angstroms.

Table 4.1 shows the 12 distortion vectors projected on the three CDW wave vectors $\overrightarrow{i}$, $\overrightarrow{j}$, $\overrightarrow{k}$ ($d_i = \overrightarrow{d} \cdot \overrightarrow{i}$). The periodic structure displacement (PSD) of the CDW unit cell can be constructed from the 12 distortion vectors around the CDW maxima. Band structure and phase transition calculation could be carried out with the measured PSD of the CDW [45, 46]. The result could be compared with further studies of the spectroscopy of the new CDW. From Table 4.1 the largest displacement is 0.8 ± 0.1 Å (24% of the lattice constant) which is anomalous compared with the distortion observed in usual 1T systems where the maximum displacement $\leq$ 0.2 Å and in 2H systems ($\leq$ 0.05 Å) [47]. The distorted lattice shows the quasi-ribbon like structure along direction $\overrightarrow{j}$, which is very similar to what happened in $TaTe_2$ and $NbTe_2$ [21] where large distortions and the ribbon-like structure were observed. I speculate that a single $\overrightarrow{q}$ CDW was truncated by the defect in $\overrightarrow{i}$ direction and this caused the asymmetry of the distortion. It also shows that when there is asymmetry, the distortion tends to be large as observed in the cases of $TaTe_2$ and $NbTe_2$. More data on atomically resolved microscopy on other nanocrystals and theoretical modeling are needed to explore this interesting correlation between asymmetry and large distortion of CDW.

4.5 Summary

Our scanning tunneling microscopy work at 4.2 K on 2H-$NbSe_2$ shows two distinctive features that have never been reported even in similar or related systems. The first is the disordered phase of the new $\sqrt{13} \times \sqrt{13}$ modulation. It

shows the CDW can be localized and viewed as individual cells interacting with each other. The second is the atomic distortion in the new modulation. Rather large displacements were observed in this case. I believe it is due to the asymmetry of the nanocrystal. I also proposed that local heating was the source for nanocrystal creation and the disordered phase was formed by the quenching process. Further experimental and theoretical studies are necessary to better understand all the phenomena presented in this report.

Chapter 5

Imaging Vortex Matter by STM: Statics and Dynamics

In this chapter, I introduce the novel role of STM in the study of static and dynamic properties of vortex matter system in type II superconductors. Extensive theories and experiments over the last two decades contributed to our understanding of this complex system. However, many crucial questions remain unanswered, and the detailed understanding of some of the phase space is still unclear.

After introducing background knowledge of the Bragg glass phase of vortex matter and experimental methods in Sec. 5.1 and 5.2 and 5.3, I will demonstrate the use of our LTSTM as a new imaging technique to study the static properties of the Bragg glass phase of vortex matter in Sec. 5.4.1. In Sec. 5.4.2, I will discuss our most important result on the dynamic creep motion of the system. The last section will be devoted to the direct imaging of the interaction between the vortex system and a variety of impurities followed by a conclusion and subsections for future work.

5.1 Background and Motivation

In this section I will give a brief introduction to the development of the field of vortex matter. A more extensive review can be found in [2]. In 1957, Abrikosov presented the vortex solution of the Ginzburg-Landau equations and predicted the behavior of type II superconductors in his famous paper [48]. The mean-field phase

diagram of conventional low temperature type II superconductors was constructed then and proved to be very accurate later [2].

The $H - T$ diagram (Fig. 5.1) consists of three phases, a Meissner phase ($H < H_{c_1}(T)$) with complete magnetic expulsion, a novel mixed phase ($H_{c_1}(T) < H < H_{c_2}(T)$) and a normal metal phase ($H > H_{c_2}(T)$). In the mixed phase the magnetic induction $\mathbf{B}$ can penetrate the superconductor in the form of vortex lines each carrying a quantum of magnetic flux $\Phi_0 = hc/2e \approx 2 \times 10^{-15}$ Wb. As illustrated in Fig. 3.5, a vortex consists of a region with a radius ξ (the coherence length) away from the center of each line where the superconducting order parameter Ψ is suppressed and a region with a radius λ (the penetration depth) in which supercurrents screen the external field.

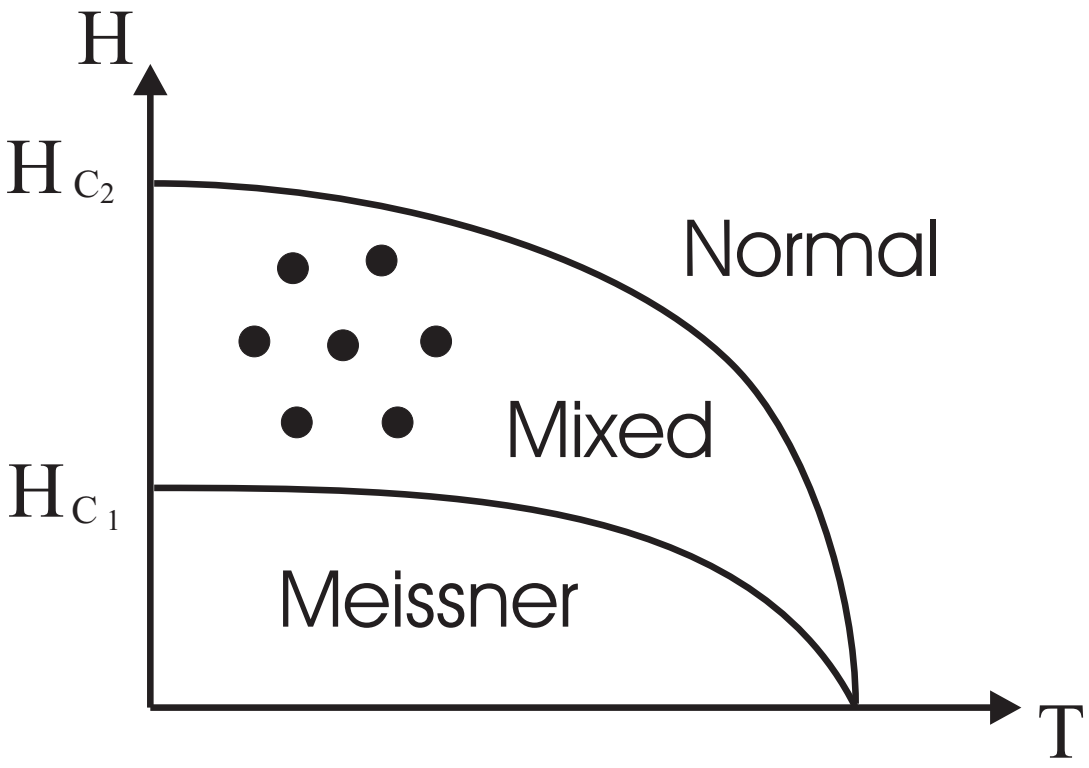

Figure 5.1: **Mean Field Phase Diagram of Type II Superconductors.** Typical phase diagram of type II superconductors such as 2H-$NbSe_2$. For 2H-$NbSe_2$ at 4.2 K, $\mu_0 H_{c_2} \sim 2.1$ T, $\mu_0 H_{c_1} \sim 20$ mT [23, 49].

As a result of minimizing the Ginzburg-Landau free energy, Abrikosov predicted the vortex lines organize as a perfect lattice structure in the mixed phase, later observed in [24]. The lattice is triangular for standard systems and it is called the Abrikosov lattice, vortex lattice (VL) or flux line lattice (FLL) in the literature. Figure 3.5 and Fig. 3.7 show the diagram and an example image from our STM measurement of the lattice. The lattice constant a is a function of induction $\mathbf{B}$, $a = \sqrt{2\Phi_0/\sqrt{3}B} \approx 1.075\sqrt{\Phi_0/B}$. The vortex lines interact with each other with an effective potential energy $E = 2\epsilon_0 K_0\left(\frac{d}{\lambda}\right)$ per unit length along the line, d is the distance between two vortices, K_0 is the zeroth order Hankel function and $\epsilon_0 = (\Phi_0/4\pi\lambda)^2$ is the energy scale per unit length. This repulsive energy increases with field and rapidly vanishes when temperature T goes to T_c since $\lambda(T) \approx \lambda(0)/\sqrt{1-(T/T_c)^4}$ diverges at T_c. Due to this interaction, the lattice can also be described by an elasticity theory. The temperature and magnetic evolution of the elastic moduli of the lattice can be derived from this interaction energy [50].

Now let's shift focus to the interesting dynamic properties of the vortex system. In this picture [51], when an external current $\mathbf{j}$ is applied, the vortices will start to move under the influence of the Lorentz force per unit length $\mathbf{F}_L = \mathbf{j} \times \mathbf{B}/c$ (for each vortex, the force per unit length is $\mathbf{f}_L = (\Phi_0/c)\mathbf{j} \times \mathbf{n}$, $\mathbf{n}$ is the unit vector along the vortex). If the system is perfectly homogeneous, the only counter balance to this force is the friction force, $\mathbf{F}_\eta = -\eta\mathbf{v}$. Here η is the friction coefficient and $\mathbf{v}$ is the velocity of the vortex. At balance, we have the steady state $\mathbf{v} = \mathbf{j} \times \mathbf{B}/(c\eta)$. The dissipation comes about because when the vortex system moves, an emf voltage drop develops across the system along the same direction of $\mathbf{j}$ due to Faraday's

Law. The induced electric field can be written as $\mathbf{E} = \mathbf{B} \times \mathbf{v}/c$. The power of dissipation is thus $P = (\mathbf{j} \times \mathbf{B})^2/(c^2\eta)$ where $\eta \approx BH_{c_2}/(c^2\rho_N)$ (ρ_N being the normal state resistivity) can be calculated by analyzing the dissipation process [51]. As a result, the material is not a perfect conductor, with $\rho_{eff} = \rho_N B/H_{c_2}$ for $\mathbf{j} \perp \mathbf{B}$. In order to make the material a better conductor, we have to paradoxically drop the homogeneity assumption and introduce quenched disorder to be sources of another force to counter balance $\mathbf{F}_L$. In real materials, quenched disorder (eg., atomic vacancies, interstitials, impurities, lattice dislocations, twin boundaries, grain boundaries, second-phase precipitates, *etc.*) always exists in the underlying atomic crystal and is crucial for maintaining high conductivity of the material in the presence of a magnetic field. The quenched disorder will exert a pinning force with a density $\mathbf{F}_{pin}$ on the vortex system. It will counter balance $\mathbf{F}_L$ and hold the vortex lattice still. The current can then remain dissipation-free until it reaches a critical value $j_c = F_{pin}c/B$ (for $\mathbf{j} \perp \mathbf{B}$) and breaks the balance.

The current density j_c is the critical depinning current density. Understanding this limit is necessary for development of various technological applications. Since type I superconductors all have small H_c's, the applicable current and sustainable external field are very limited, as they are in the Meissner phase for type II superconductors. The critical current density j_c and upper critical field H_{c_2} of type II superconductors in the mixed phase are usually very high. Most of the superconductors used in commercial magnets or other applications are type II and operate in the mixed phase. It is therefore desirable to optimize the pinning in the system and maximize j_c. Various methods have been used to increase the pinning strength

of the disorder, including using Fe impurities in $NbSe_2$ samples, which will be our focus of interest.

The central problem of the statistical mechanics and dynamics of a quantum disordered system is still incompletely understood. This is because of the extreme complexity of the problem which involves quenched disorder, thermal fluctuations, and quantum fluctuations in the system [2]. Even introducing only the quenched disorder to the elastic vortex system causes a drastic change of the statics and dynamics of the system and thus the phase diagram [2]. In Sec. 5.2 we will introduce the efforts from theorists to address this complicated issue.

The interest in this problem was revived since the discovery of high T_c superconductors (HTSC) [52]. Many experiments has been carried out and theories constructed [53]. Notable experiments include the transport measurements, the Bitter decoration and magneto optical measurements. These probe measurements are all microscopic measurements that directly image the vortex system. But all of them can only work at low fields up to 500 G at best. In STM experiments the applicable magnetic field can be much higher (usually more than 0.1 T). This makes the STM system an indispensable new technique to image the system in a vast region of the phase space which is untouchable by other techniques.

5.2 Theoretical Description of Vortex Matter

Since a real vortex system usually consists of hundreds or thousands of vortex lines, the microscopic description of the vortex system by the Ginzburg-Landau

theory becomes inappropriate to handle the interactions and dynamics that are essential to the problem. A better way is to treat the vortex lines as individual elastic objects. The core of the vortex can be viewed as a string and the elastic forces are provided by the supercurrent. This simplified description has advantages in including the effects of weak disorder and dealing with the macroscopic physics such as phase diagram, imaging results, and transport measurements. It also connects to other interesting problems in classic and quantum systems: magnetic domain walls, wetting contact lines, colloids, magnetic bubbles, liquid crystals, charge density waves, and Wigner crystals [1, 2].

In this description, the perfect lattice points are viewed as the equilibrium positions, $\mathbf{r}_i^0$, of the objects. The elastic Hamiltonian is defined on the displacement, $\mathbf{u}(\mathbf{r}_i, z) = \mathbf{r}_i - \mathbf{r}_i^0$, with $\mathbf{r}_i$ the position of the object in 2D:

$$H = \frac{1}{2}\sum_{\alpha,\beta}\int d^d q u_\alpha(\mathbf{q}) c_{\alpha\beta}(\mathbf{q}) u_\beta(-\mathbf{q}) \tag{5.1}$$

($d = 3$ in our system, I keep it here for the convenience of discussion). Here $c_{\alpha\beta}(\mathbf{q})$ is the elastic matrix which can be calculated from the interaction forces, $\mathbf{q}$ is the corresponding vector in Fourier space for (r,z). $c_{\alpha\beta}(\mathbf{q}) = cq^2$ for standard elasticity [50]. A simplified isotropic version in real space is:

$$H \sim \frac{1}{2}\int d^d r \; c(\nabla \mathbf{u})^2. \tag{5.2}$$

In a real vortex lattice, there are three different elastic constants c_{11}, c_{66}, c_{44}, corresponding to the bulk, shear and tilt deformation processes [50]. Although the values of these material parameters can vary from system to system, this does not change the quadratic nature of the Hamiltonian.

To characterize the physics of the elastic system, two important quantities are usually calculated. The first is the relative displacement correlation function

$$B(r) = \frac{1}{2}\overline{\left\langle [\mathbf{u}(r) - \mathbf{u}(0)]^2 \right\rangle} \tag{5.3}$$

which measures the relative displacements of two points separated by distance r. Here $\langle\rangle$ averages over thermal fluctuation and $\overline{\cdots}$ averages over disorder. The growth of $B(r)$ along r is a measure of how fast the lattice is distorted. For thermal fluctuations alone in $d > 2$, $B(r)$ saturates at finite values, indicating the lattice order is preserved. In the presence of disorder, the perfect positional order could be destroyed and $B(r)$ would grow unbounded. $B(r)$ can be measured directly by imaging techniques [53].

Another important quantity is the structure factor of the lattice. It can be obtained by computing the Fourier transform of the density of object:

$$\rho(\mathbf{r}) = \sum_i \delta(\mathbf{r} - \mathbf{r}_i^0 - \mathbf{u}_i). \tag{5.4}$$

The structure factor $S(q) = \overline{\langle \rho(q)\rho(-q) \rangle}$ can be directly measured in diffraction experiments [53, 54]. For a perfect lattice, the diffraction pattern consists of δ-function Bragg peaks at the reciprocal vectors of the lattice. If some degree of short range order exists, the peaks will be broadened. The shape and width of any individual peak thus will measure the degree of translational order of the lattice. To measure that quantitatively, for any peak centered around a reciprocal vector G, a correlation function $C_G(r)$ can be obtained by Fourier transforming back to real space. This correlation function, usually referred to as the translational order

correlation function, can be written as:

$$C_G(r) = \overline{\langle e^{i\mathbf{G}\cdot(\mathbf{u}(r)-\mathbf{u}(0))}\rangle}. \tag{5.5}$$

It directly measures the degree of the translational order that remains in the system. For a perfect lattice and δ-function Bragg peak $C_G(r) = 1$. For thermal fluctuations alone, $C_G(r \to \infty) =$ constant. The faster $C_G(r)$ decreases, the broader the peak, and the more disordered is the lattice. This quantity can also be extracted from imaging experiments. For Gaussian fluctuations such as thermal fluctuations,

$$C_G(r) = e^{-G^2 B(r)/2}. \tag{5.6}$$

However, this relation is not always true for systems with fluctuations other than thermal ones. It only holds qualitatively in general.

To incorporate the effects of disorder into the model, a simplification is usually made by coupling a random potential $V(\mathbf{r})$ directly to the density of vortices $\rho(\mathbf{r})$

$$H_{dis} = \int d^d r V(\mathbf{r})\rho(\mathbf{r}). \tag{5.7}$$

This model ignores the microscopic properties of the disorder and treat them as weak point-like pinning centers randomly distributed in the system. In high quality single crystals, point-like (uncorrelated) disorder dominates. For systems with extended defects (correlated disorder) such as one-dimensional screw dislocations or twin boundaries, a strong pinning model has to be employed [2]. In our low-T_c system with introduced point impurities, this weak-pinning-center approximation is an appropriate choice. The simplified random potential is $V(\mathbf{r}) = V\sum_i \delta(\mathbf{r} - \mathbf{r}_i)$ where $\mathbf{r}_i$ is the position of the impurities. For weak disorder, it is legitimate to

replace $V(\mathbf{r})$ by a simple Gaussian potential with a correlator [55]

$$\overline{V(\mathbf{r})V(\mathbf{r}')} = \Delta(\mathbf{r} - \mathbf{r}') \tag{5.8}$$

where Δ is a function with range r_f. In superconductors, one has $r_f \sim \xi$, the coherence length. Even with these simplifications, this is still a highly complicated problem to solve due to the non-linear nature of the δ-function in $\rho(\mathbf{r})$.

$H + H_{dis}$ describes the general elastic system coupled to disorder. The underlying competition between the elastic force from H (Eq. 5.1) that maintains the lattice order and the disorder effect from H_{dis} (Eq. 5.7) that distorts it leads to the complicated state of the system which shows interesting statics and dynamics.

5.2.1 Collective Pinning Theory

Larkin [56] made a further ground-breaking simplification about the disorder Hamiltonian: for small displacements, the coupling can be expanded and approximated as:

$$H_{Larkin} = \int d^d r \; f(\mathbf{r})u(\mathbf{r}). \tag{5.9}$$

Here $f(\mathbf{r})$ is a random force with Gaussian correlations acting on the vortices. This now exactly solvable linear model yields

$$B(r) = B_{thermal}(r) + \frac{\Delta}{c^2} r^{4-d} \tag{5.10}$$

$$C_G(r) = e^{-G^2 B(r)/2} \simeq e^{-r^{4-d}} \tag{5.11}$$

if the correlation is local $\overline{f(\mathbf{r})f(\mathbf{r}')} = \Delta\delta(\mathbf{r} - \mathbf{r}')$. Here c is the elastic constant in Eq. 5.2. A remarkable conclusion of this theory is that any weak disorder does

destroy long-range translational order for $d < 4$. The displacement will grow unbounded ($B(r) \sim r$ for $d = 3$) and the perfect order of the lattice will be lost at large scale.

The two important characteristic length scales in this model are: (i) R_c which is the distance at which the relative displacements of the lattice are of the order of the correlation length of the random potential r_f (ξ at low temperature), *i.e.*, $B(R_c) \sim \xi^2$; and (ii) R_a at which the relative displacement is of the order of the lattice constant, *i.e.* $B(R_a) \sim a_0^2$. The limitation of the Larkin model stems from the linearity of the approximation in Eq. 5.9. The translational symmetry $u \rightarrow u + a_0$ in Eq. 5.7 does not exist in this linear model. Since physically this global translation does not change the total energy, the total pinning force in this model is zero. The nonlinearities of the disorder term are thus necessary to properly describe the pinning. Also as the expansion depends on u and the result shows $B(r)$ will grow unbounded, the model can not be used to describe the system at large scales. In a masterful stroke of physical intuition [57], Larkin and Ovchinikov (LO) realized this model breaks down exactly at the length scale corresponding to the critical pinning force F_c. In the presence of an external force, LO argued that bundles of the vortices will be moved by the force and the larger the force, the smaller the size of the bundle. The Larkin model works when forces are larger than F_c so the motion is free and no pinning is involved. But below F_c, anomalous transport appears. The energy gained by the external force $\int d^d r \ F_{ext} u(\mathbf{r})$ equals the elastic energy plus the disorder energy in the bundle at the breakdown scale of the model. Any force smaller than F_c will involve a bundle larger than this which the model is not able to

describe. LO noticed that the expansion in displacements in the model breaks down when a vortex line moves by more than its width $\sim \xi$ [57]. Therefore the breakdown of the model happens at R_c instead of R_a. Using scaling analysis, LO showed that the balancing of energy gives the critical force density

$$F_c = \frac{c\xi}{R_c^2} \tag{5.12}$$

and thus the critical current density J_c. Equation 5.12 is the famous Larkin-Ovchinikov relation which calculates the critical dynamic quantity directly from the length scale of the static problem.

5.2.2 Bragg Glass Theory

To better understand the system beyond the Larkin length scale R_c, a quantitative theory which fully solves $H + H_{dis}$ is needed. The Bragg glass theory [58, 59] was formulated to address this problem. This model now includes the nonlinearity of the coupling and periodicity of the lattice system by decomposing the density, Eq. 5.4, into Fourier components according to the periodic perfect lattice R_i^0

$$\rho(\mathbf{r}) = \rho_0 - \rho_0 \nabla \cdot \mathbf{u}(\mathbf{r}) + \rho_0 \sum_{\mathbf{K}} e^{i\mathbf{K}(\mathbf{r}-\mathbf{u}(\mathbf{r}))} \tag{5.13}$$

and thus rewriting the H_{dis} as

$$H_{dis} = \rho_0 \sum_{\mathbf{K}} \int d^d r \; V(\mathbf{r}) e^{i\mathbf{K}(\mathbf{r}-\mathbf{u}(\mathbf{r}))} + \rho_0 \int d^d r \; V(\mathbf{r})(1 - \nabla \cdot \mathbf{u}(\mathbf{r})). \tag{5.14}$$

This is a very complicated problem. Giamarchi and Le Doussal [58, 59] used the replica method, the variational method, and the renormalization group method to

attack the problem. Here I only state the main results of the theory. The relative displacement correlation function $B(r)$ is found to develop over three different regimes. As illustrated in Fig. 5.2, the first regime below R_c is the Larkin regime in which $B(r) < \xi^2$ and it grows as r^{4-d}. The second regime is between R_c and R_a. The vortex line behaves much like the simplified model of a single line around pinning centers. This is called the random manifold regime. In this regime, $\xi^2 < B(r) < a_0^2$ and the growth is still algebraic but the exponent is different $B(r) \sim r^{2\nu}$ with $\nu \sim 1/6$. For $r > R_a$ the solution predicts a logarithmic growth for the correlation $B(r) \sim A_d \log(r)$ where A_d is a universal amplitude depending only on dimension. For Gaussian fluctuations, the translational correlation function given by Eq. 5.6 has a slow algebraic decay for $d > 2$, $C_G(r) \sim (1/r)^{A_d}$. This shows the quasi-long-range order persists. This third regime is the asymptotic regime.

This description of the disordered, periodic, elastic system applies to vortex matter in both low-T_c and high-T_c superconductors. The striking result is that instead of the positional order being destroyed by the weak disorder as in the collective pinning theory, a quasi-long range order is preserved in the system due to the periodicity. In this case, algebraically divergent Bragg peaks should be found in the structure factor $S(q)$ from diffraction experiments. This phase (which is nearly as ordered as a perfect solid) is actually a glass when the dynamic properties are considered. It has many metastable states separated from its ground state by divergent barriers and exhibits pinning and nonlinear dynamics such as creep motion, *etc.* Another important feature is that this solution is self-consistently stable without dislocation. This phase is thus called the Bragg glass phase which is a stable

glass phase with quasi-long range order. More experimental consequences from the theory can be found in [59, 60]. Experimental results such as [54] provide direct evidence of this phase in type II superconductors.

Other than the static results mentioned above, the theory also predicts a different phase diagram and dynamics for the vortex system. In what follows, I will introduce them without going into the details of the model.

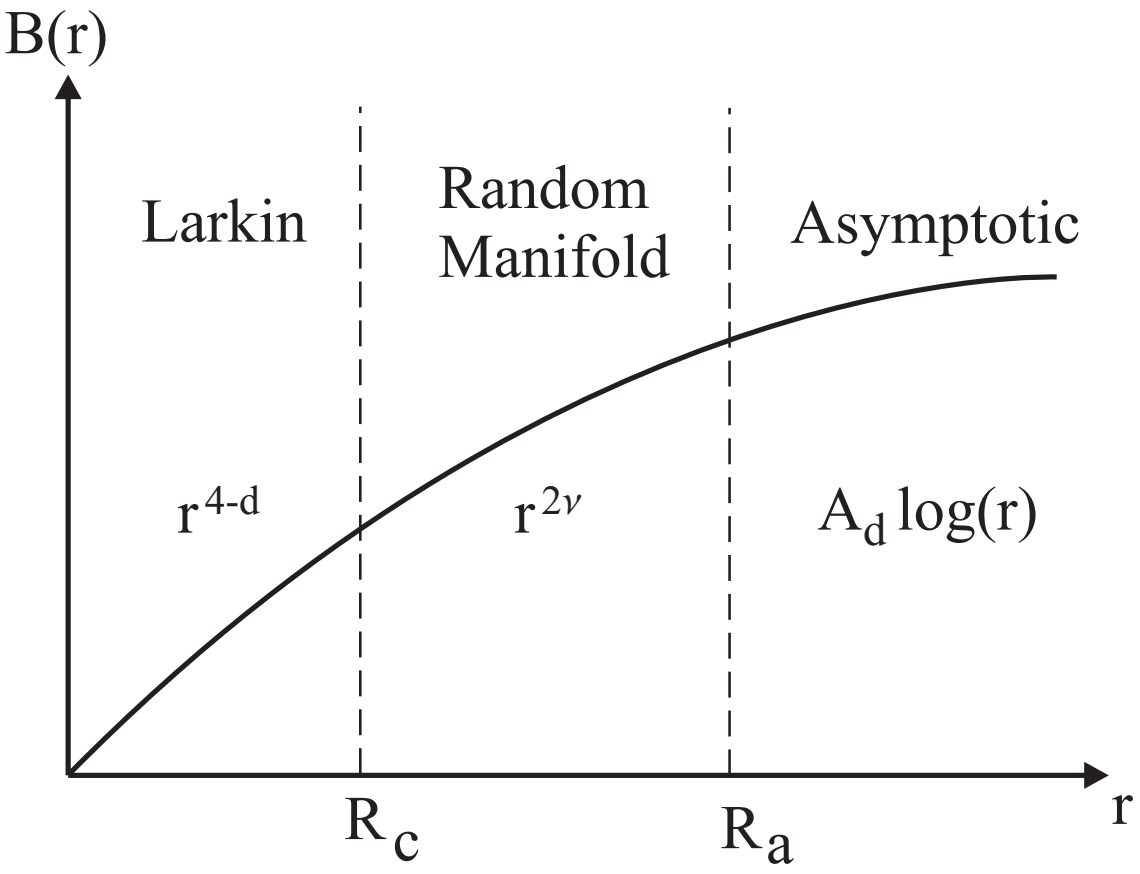

Figure 5.2: **The Relative Displacement Correlation Function in Bragg Glass Theory.** Three regimes with different behaviors are defined by the length-scales R_c and R_a: the Larkin regime, the random manifold regime, and the asymptotic regime.

5.2.3 Phase Diagram of the Vortex Phase of $NbSe_2$

The existence of the Bragg glass imposes a generic phase diagram for all type II superconductors as illustrated in Fig. 5.3 (a). The Bragg glass phase covers most of the mixed-state phase space when compared with Fig. 5.1 from the classical theory. New experimental evidence [61] confirmed this phase separation. Fig. 5.3 (b) shows a typical $H - T$ phase diagram of Fe-doped $NbSe_2$ measured by experiment.

The Bragg glass phase and the rest of the mixed state phase in which the vortex matter forms a disordered solid are separated by the H_p line determined by the peak effect in the DC critical current measurement. This line marks a first order "melting" phase transition from the ordered (Bragg) phase to the disordered phase.

Our samples include pristine $NbSe_2$ and Fe-doped $NbSe_2$. Transport measurement shows that the phase diagrams of these two samples are different in that there is no reentrance of the disordered phase at low fields for the pure $NbSe_2$ sample. All the imaging measurements using other techniques were carried out at very low field as marked in Fig. 5.3(b). Our STM experiments are all carried out in the Bragg glass phase as marked by the red arrow in Fig. 5.3 (b). Our measurements are much more relevant to the peak effect usually measured at high fields. It is definitely desirable to image the melting transition from the Bragg glass to disordered phase or vice versa at high fields by our STM, yet a defect in our setup currently limits our applicable magnetic field [1].

[1]The probe we first installed proved to be made of SS304 which is ferro-magnetic instead of non-magnetic SS316 to SS321 as we ordered. The high field operation will increase the chance of failure of the system due to the possible mechanical stress in the probe.

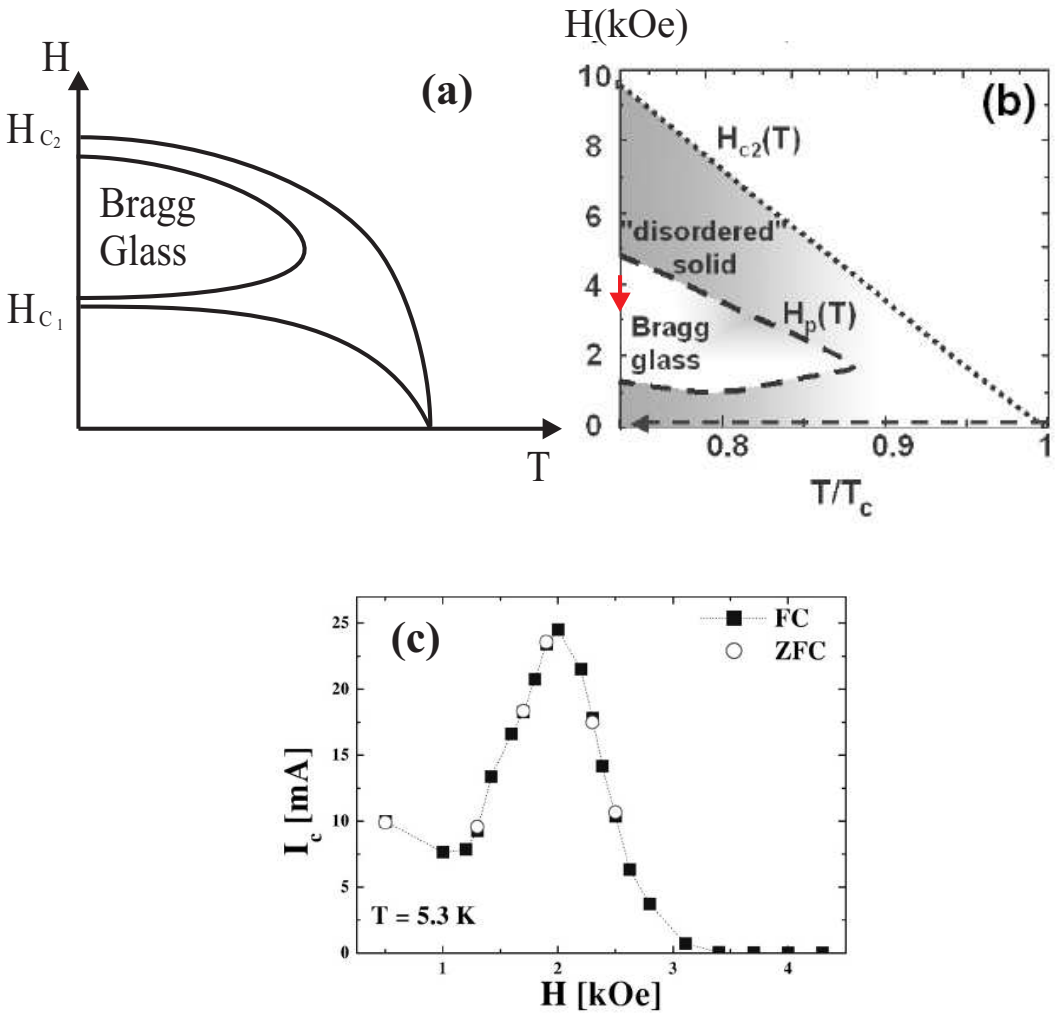

Figure 5.3: **New Phase Diagram for Type II Superconductors.** (a) resembles the universal phase diagram for type II superconductors in Bragg glass theory. A new section in the mixed phase is the ordered Bragg glass phase. The Bragg glass can "melt" to a disordered phase. (b) shows the typical phase diagram of $NbSe_2$ measured in experiments. The black dashed arrow indicates the typical path of a magnetic decoration experiment. The red arrow shows the path we took in STS imaging experiments. Data taken from [61]. Figure borrowed from [53] (c) shows a experimental observation of the peak effect in a Fe doped $NbSe_2$ sample. Figure borrowed from [62].

5.2.4 Dynamics of a Moving Bragg Glass

The dynamic properties of the Bragg glass phase are critical to our understanding of this system due to their fundamental and technological importance. The competition between the elasticity and the disorder not only determines the interesting static properties of the stable state, it also has dramatic consequences on the dynamics. The main focus of previous theoretical studies is on the average velocity which is proportional to the voltage in the transport measurement, versus driving force, usually the current in experiment. The equation of motion of the vortices with a driving force $\mathbf{f}$ and a thermal noise ζ reads

$$\eta \frac{d\mathbf{r}}{dt} = -\frac{\delta H}{\delta \mathbf{r}} + \mathbf{f} + \zeta. \tag{5.15}$$

Since the average velocity $\mathbf{v} \equiv \overline{\langle d\mathbf{r_0}/dt \rangle}$ is the parameter of interest, it is advantageous to consider v as prescribed and obtain $\mathbf{f} = \mathbf{f}(\mathbf{v})$ required to maintain the given v. The equation of motion of the displacement is usually taken as a basis for analysis:

$$\eta \frac{d\mathbf{u}}{dt} = -\frac{\delta H}{\delta \mathbf{u}} + \mathbf{f} - \eta \mathbf{v} + \zeta. \tag{5.16}$$

This is again a very complicated problem to attack and many questions arises concerning both the static properties in the moving frame and the dynamical properties. Here I'll only concentrate on the results that are of interest to our system. More information can be found in [1, 55] and the references therein.

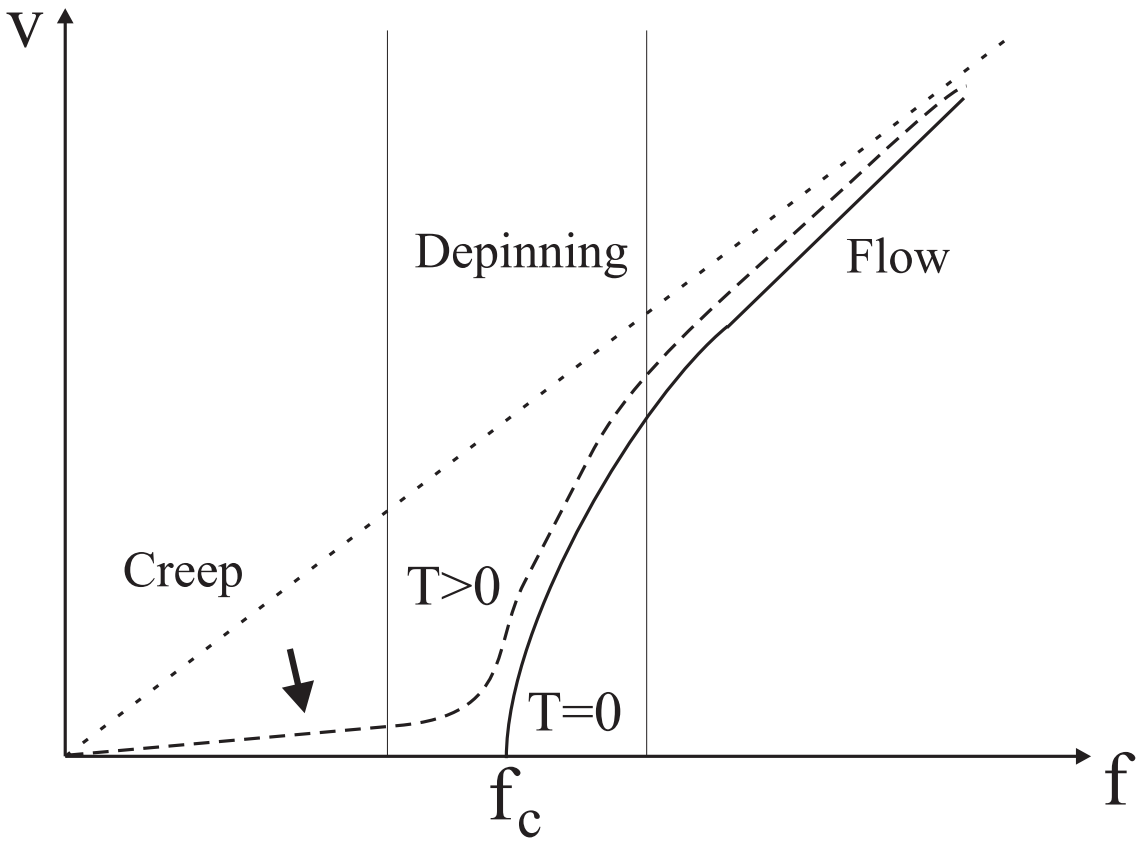

Figure 5.4: **Typical Velocity-Force Characteristics.** The typical response of velocity v in response to an external force f for a vortex system. At $T = 0$ the systems is pinned below the critical force f_c. However, at finite temperature, motion can occur even for $f < f_c$. Especially at $f \ll f_c$ the system's creep motion is a signature of a Bragg glass. For large driving forces, the system flows as if there is no disorder.

Fig. 5.4 shows the three regions of the $v - f$ characterics from the Bragg glass theory [63, 64]: the flux creep region with very small driving force, the flux depinning region around the critical force, and the flux flow region with high moving velocity. The arrow shows the region of our interest (see Sec. 5.4.2). At $T > 0$, the motion of the vortex system occurs at any driving force.

For low temperatures and very small driving force $f \ll f_c$, the motion is expected to be very slow. The response was thought to be linear in the Thermally Assisted Flux Flow (TAFF) [65] model. The idea is depicted in Fig. 5.5(a). The moving units in the system are flux bundles [65]. The pinned bundle of the system has to move in an energy landscape with constant barrier heights U. The effect of the external force f is to tilt the landscape to be washboard-like, allowing the bundle to move. The bundle can move until it is trapped at one of the local minima in the energy landscape and it will spend more time in that configuration or meta-stable state. An Arrhenius law was used to describe the thermal activation process of the system to overcome the barriers. Assuming a constant U and that all the minima are separated by the lattice constant a_0, in TAFF the velocity is calculated as $v \propto e^{-\beta(U - fa_0/2)} - e^{-\beta(U + fa_0/2)} \sim e^{-\beta U} f$ with $\beta = 1/k_B T$.

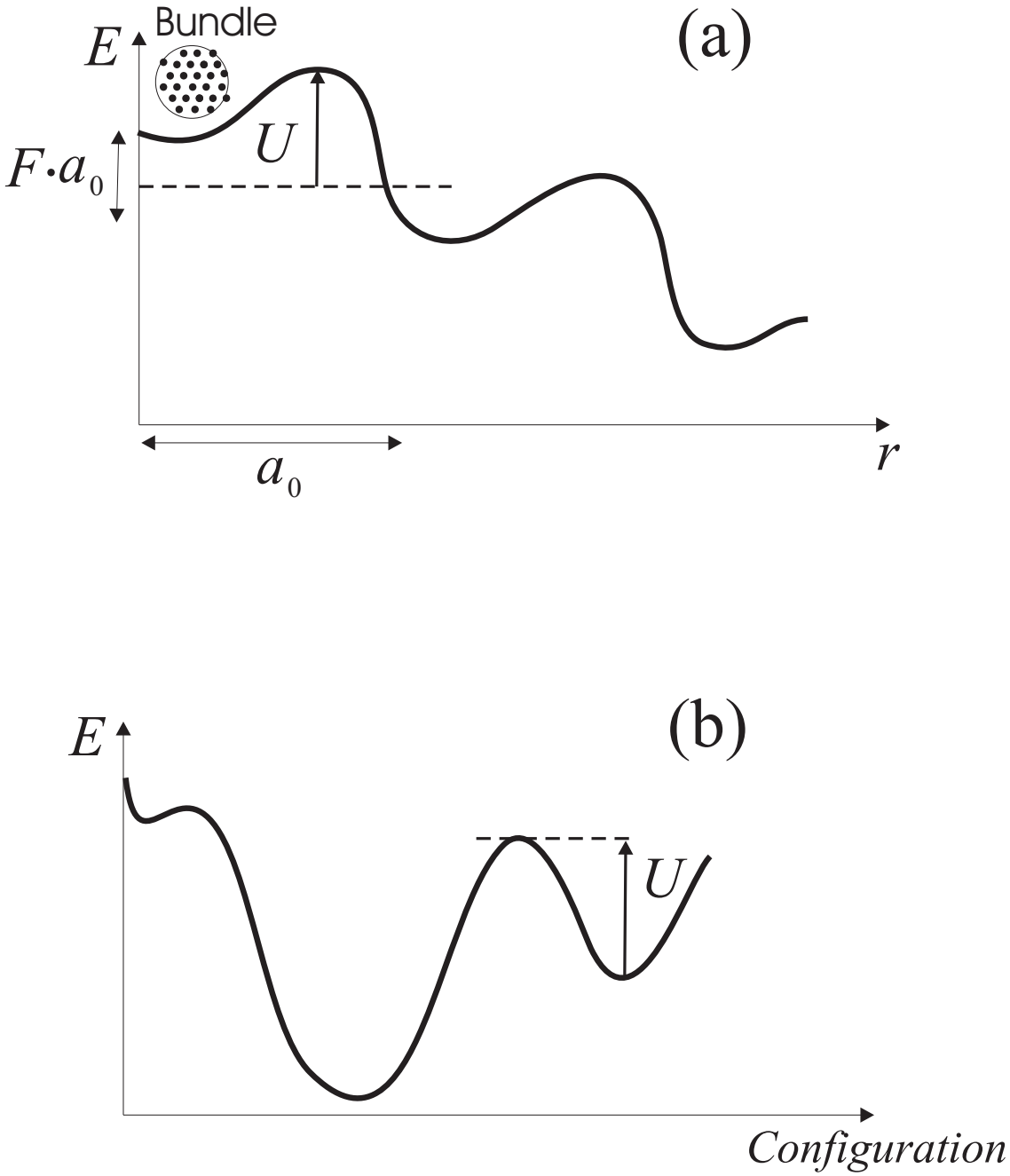

Figure 5.5: **Energy Landscape.** (a). In the TAFF model the energy landscape, characterized by the barrier U, is tilted by an external force f. (b) shows the energy landscape in the collective creeping theory where the potential U is different for different configurations.

However, this simple picture does not hold for a glass system in which barrier heights vary and the barrier heights are expected to diverge as one gets closer to the ground state. There are many metastable states in the elastic description of the glass system. As depicted in Fig. 5.5(b), the energy will depend on the configuration of the elastic system and the barrier distribution will be far from constant. The external force will change the metastable solutions. This makes the barrier height dependent on the force and the dependence is highly nonlinear for the glass system. The hopping between the neighboring states separated by the energy barriers when $f \ll f_c$ determines the characteristics of the creep motion.

To accommodate this complication, a new model called the collective creep model [66] was proposed by Feigel'man *et al.* A scaling approach was used based on two basic assumptions, i) the motion is slow so the static description can be used at any time; ii) the scaling of barrier height is the same as the scaling of the minimum energy from static results. As a bundle of size R move to the next metastable state by distance $u \sim R^{\nu}$, the energy of the metastable state scales as $E \sim R^{d-2+2\nu}$ and the energy gained from the external force $E_F = \int d^d x f u(x) \sim f R^{d+\nu}$. The moving condition $E_F > E$ gives the minimum size of the bundles that move to the next state $R_{\min} \sim \left(\frac{1}{f}\right)^{1/(2-\nu)}$. This indicates the size of the moving bundle increases as the force decreases. Thus the minimum energy barrier between metastable states now scales as $U(f) \sim R_{\min}^{d-2+2\nu} \sim \left(\frac{1}{f}\right)^{\mu}$ with $\mu = \frac{d-2+2\nu}{2-\nu}$. The average velocity $v \propto e^{-\beta(U(f))}$ is now nonlinear. $U(f)$ can be written as $U_c \left(\frac{f_c}{f}\right)^{\mu}$ where U_c is the barrier of a bundle with scale R_c and f_c is the critical force.

Experimentally, transport [67] and magnetic relaxation [68] measurements

agree well with the scaling argument [69]. Further theoretical works such as [63, 64] were carried out to obtained more precise characteristic $v(f)$. However, other than the average velocity, the nature of the creep motion itself is largely unclear. In [70] Vinokur *et al.* studied the distribution of the energy barrier for a given f in the vortex system. Combining extreme statistics and the coarse graining method, they recovered the collective pinning result from the scaling approach. For a 1D vortex string with a length L their result shows the distribution density of the potential wells:

$$p_L(U) \approx \frac{1}{U_c}\frac{L}{L_c}\exp\left(-\frac{U}{U_c}\right)\exp\left(-\frac{L}{L_c}\exp\left(-\frac{U}{U_c}\right)\right) \tag{5.17}$$

where U_c, L_c can be calculated from the static exponents and length scales [69]. Here we make a natural extension of the above result to the velocity distribution of the motion. Using an Arrhenius law, the waiting time at the minima or lifetime of the metastable state $\tau \propto \exp(\beta U)$, we write the velocity of the motion as $v = v_0 e^{-\beta U}$ assuming the displacement of each motion is uniform. Thus the distribution density of the creep velocity

$$p_L(v) \approx \frac{1}{\beta U_c}\frac{L}{L_c}\frac{1}{v_0}\left(\frac{v}{v_0}\right)^{\frac{1}{\beta U_c}-1}\exp\left(-\frac{L}{L_c}\left(\frac{v}{v_0}\right)^{\frac{1}{\beta U_c}}\right). \tag{5.18}$$

This distribution when integrated over the length L will result in an exponential distribution of the barriers globally and lead to the recovery of the collective creep results [70]. In Sec. 5.4.2 it will be applied to our 2D result and we will discuss the details therein. Other results about the structure of the energy landscape [71] can also be compared to our results qualitatively.

Almost all of the previous imaging measurements studying the dynamics fo-

cused on the large velocity region, *i.e.* the flux flow regime [72]. One of the interesting observations is the channel effect of the moving glass phase. At sufficiently large velocity the glass phase will regain its periodic order and move along elastic channels. The vortices will follow roughly the same trajectory when in motion. Our results show that this is not the same for the slow motion. The elastic channels change seemingly randomly when the vortices move from one deep minimum point to another. Also the trajectory can deviate far from a straight line. Sliding does happen when the deviation is larger than the vortex lattice constant a_0. This is another feature that separates creep from flow. In Sec. 5.4.2 I will discuss the details of our direct observation.

5.3 Experimental Method

5.3.1 Imaging a Moving Vortex Lattice

In order to directly image the vortices in $NbSe_2$, we set the STM to STS imaging mode. As I explained in Chapter 3 the vortex cores are imaged as dark disks with radii of ξ in the STS images. This is a relatively fast imaging mode (see Sec. 2.4.5). When we set out to image the vortex lattice, we used the STS mapping mode and the scanning speed was much slower. Due to this slow speed we accidentally observed the slow moving vortex lattice. Fig. 5.6(a) shows the image we first acquired. The vortices are the white elliptical disks because, in this mode, the energy was set at 0 meV (*i.e.*, E_F) where the LDOS of the vortex cores are higher than the superconducting area as explained in Chapter 3. The stretched vortices

indicate a slow moving instead of static vortex lattice usually observed by STM [73]. Switching to STS image mode to gain scan speed, we were able to capture images of the vortex lattice frame by frame. This time each vortex was shown symmetrically round. Compiling the frames together as a movie, it is obvious that the vortex lattice is moving. The speed is as slow as ~ 1 pm/s (see Fig. 5.6 and Sec. 5.4.2). The driving source of this motion was later found to be the decaying magnetic field due to a defect of the magnet in our dewar [16].

The data in this section has previously been reported in my colleague Jonghee Lee's Ph.D. thesis [16]. Here I want to emphasize the data acquisition is of a collaborative nature.

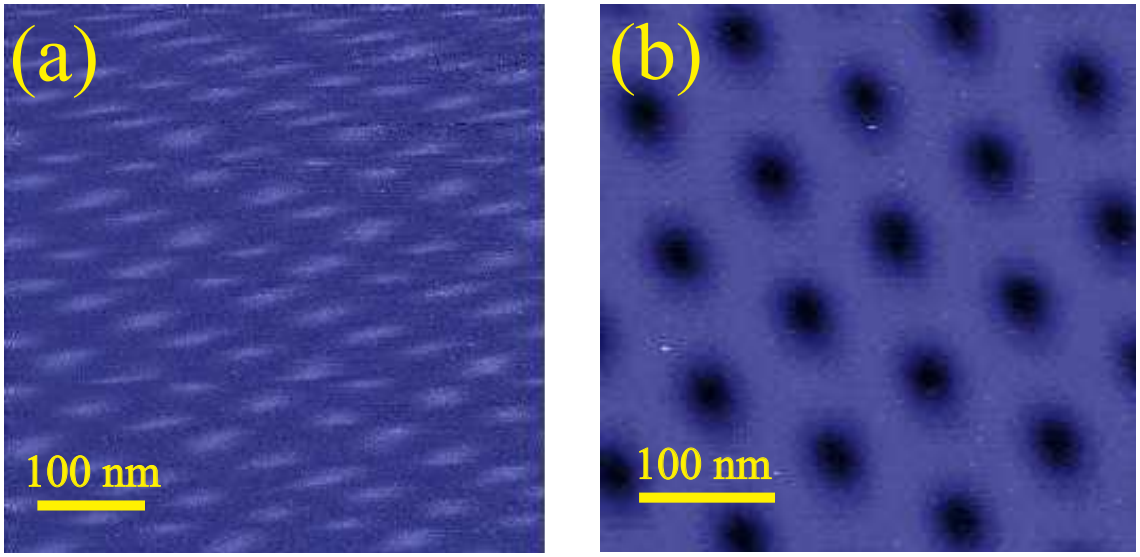

Figure 5.6: **Initial Evidence of Moving Vortices.** In (a) the image of each vortex is stretched when the scan time is long. This image is one layer with energy E = -0.5 meV from a differential conductance map which it took about 3 days to finish. Scan parameters: I = 0.1 nA, V = 5 mV, B = 0.25 T, T = 4.2 K. When we scan fast, the vortex form becomes normal in (b). This image is taken in the STS single layer imaging mode. The acquisition time is about 30 minutes. Scan parameters: I = 0.1 nA, V = 1 mV, B = 0.25 T, $T \approx$ 2 K. This shows the vortices are moving.

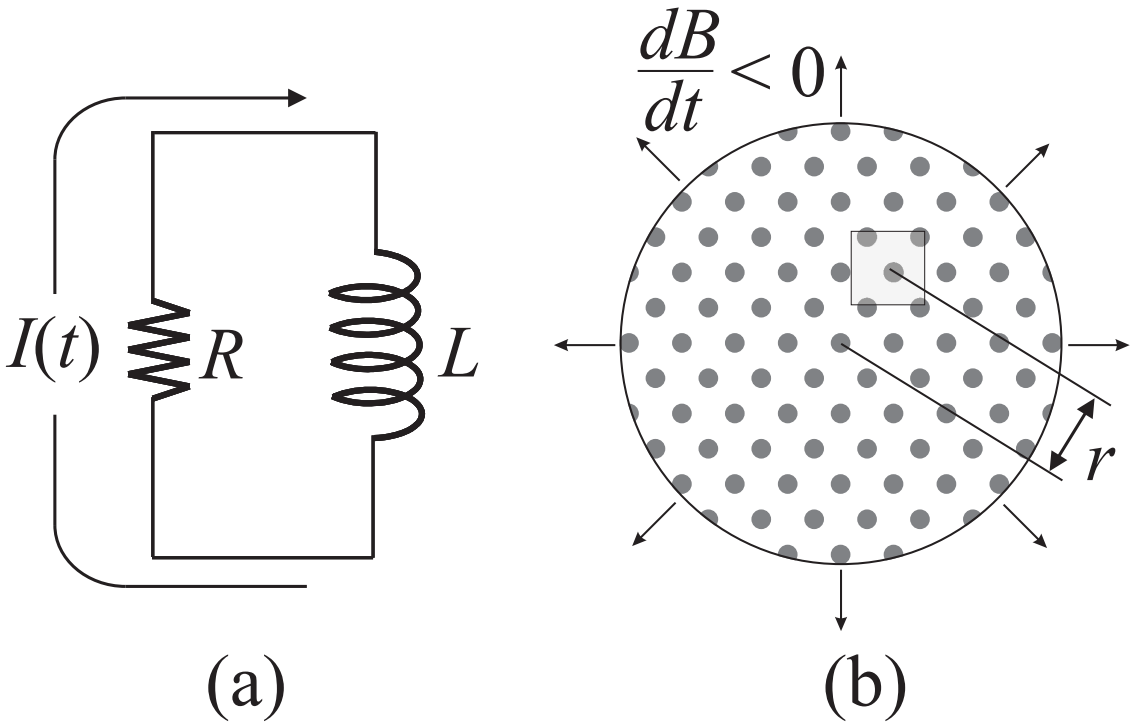

Figure 5.7: **Field Decay as the Reason of Motion.** Schematic diagrams of our magnet with a defect in (a) and the moving vortices under the influence of a decaying magnetic field in (b). As described in the text, a vortex at a distance r from the center moves at an average speed $\frac{1}{2}\frac{r}{\tau}$ with $\tau = L/R$.

Fig. 5.7(a) shows the circuit of the superconducting magnet with a residual resistance from spot-welded joints of the superconducting wire in the magnet. The current is then decaying as $I(t) = I(0)e^{-t/\tau}$ with the time constant $\tau = L/R$. The corresponding magnetic field in the magnet core decays as $B(t) = B(0)e^{-t/\tau}$. Using the model depicted in Fig. 5.7 (b), we can calculate the vortex speed by assuming our tip or our field of view is at a distance r from the center of the sample. Since the field is decaying, vortices are slowly leaving the sample. If we assume the motion is homogeneous and quasi-static, the motion of each vortex can be derived from the expansion of the lattice constant $a = \sqrt{\frac{2}{\sqrt{3}}}\sqrt{\frac{\Phi_0}{B}}$. For the vortex at r, we have

$$\begin{aligned} \frac{dr}{r} &= \frac{da}{a} = d\ln a = -\frac{1}{2}d\ln B = -\frac{1}{2}\frac{dB}{B} \\ v &= v_r = \frac{dr}{dt} = -\frac{1}{2}r\frac{d\ln B}{dt} = \frac{1}{2}\frac{r}{\tau}. \end{aligned} \tag{5.19}$$

This model proved reasonable by checking the real values of the parameters. The field decay is recorded by the magnet control unit[2]. When set to match the field stored in the magnet by turning on the persistent switch, the unit can calculate the targeted field from the matched current value. After a long experiment of 21 days and 17 hours, we were able to see the drop of the field from 0.500 T to 0.491 T. This amounts to an average decay rate $\frac{\Delta B}{\Delta t} \approx -4.2$ nT/s (≈ 0.36 mT/day). The time constant τ is then calculated to be 1.02×10^8 s (≈ 3.2 years). Given the inductance of the magnet coil $L = 12.4\ H$, we have the residual resistance $R \approx 0.1\ \mu\Omega$ which is still reasonable for the multiple joints in the coil. Assuming the tip is at $r = 1$ mm away from the center, I estimated the speed of vortex motion $v \approx 5$ pm/s by Eq.

[2]Model 420 and Model 4Q05100PS by American Magnetics, Inc.

5.19. This speed has the right order of magnitude of the observed value as we will see in Sec. 5.4.2.

Another piece of evidence to show that the decaying field is source of the motion is that we were able to stop the motion by holding the current and thereby the field constant. As illustrated in Fig. 5.8(a), if we continue to supply current to the coil even after we turn off the heat switch, the field-matching mechanism of the controller will keep feeding the current and thus the field stays as assigned[3]. A 2 day observation of the same area with vortices that were moving at $\sim$ 4 pm/s showed the vortices became stationary after the current feeding was switched on. Fig. 5.8(b) shows the stationary vortices and their tracks.

The direct imaging of slowly moving vortex lattice was made possible because of the fast scan speed and the clean sample surface. The upper bound of our scan speed is about 0.8 μm/s. It is limited by the feedback loop and the acquisition time of the lock-in amplifier. The scan time for one 400×400 frame of the STS movie is $\sim$ 4 min at this speed. The net displacement of a vortex between two frames is then $\sim$ 2 nm. Another feature of our experiment is the long duration time of continuous recording. The longest record with the magnetic field on is 4 days and 12 hours. This is much longer than any known previous imaging experiments on the vortex system and one of the longest of the STS measurements to the best of our knowledge. The stability of the whole system and the low thermal conduction design both contributed to this long measurement duration without interruptions from LHe refilling.

[3]Douglas Osheroff, Private communication, 2006

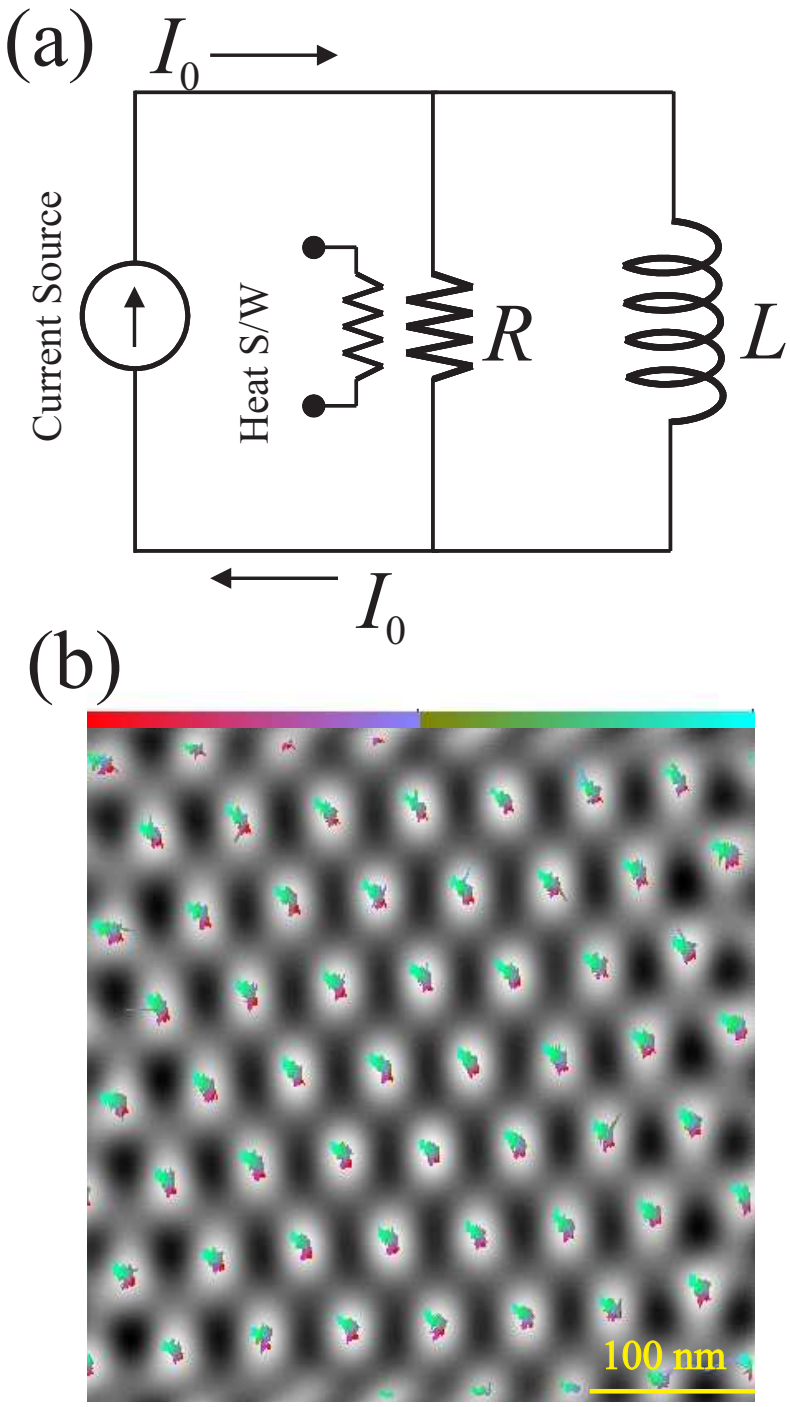

Figure 5.8: **Method to Halt the Field Decay.** (a) shows circuit schematics of how to stop the field decay. See text for details. (b) is the stationary vortex system after the field decay is halted. The color-coded tracks of the vortices (see Sec. 5.4.2) are plotted to show the system is not moving. Time is represented from red to green in the code: red means earlier time; green later.

5.3.2 Image Analysis Method

Fig. 5.9 shows the image processing procedure of the STS images using a center-of-mass method. First the image is processed by background subtraction and Fourier filtering. The Fourier filtering was usually done by setting a high pass and a low pass Butterworth filter interactively for a particular image. Then the filter is applied to the whole series. Afterwards the image is inverted to show the vortices as bright buttons. Later, a single threshold height is used to create a binary image in which the vortex areas are coded as 1 (shown white in the image). This image is used to identify each vortex and its occupied area. The center of the vortex is then calculated as the weighted sum of the coordinates (*i.e.* center of mass, mass being the height) in the inverted image over the vortex area. The recording time of the vortex can be derived from the position of the center and the scan speed. At last, a vortex lattice is constructed within frame with coordinates (x_i, y_i, t_i) (every vortex recorded has its index number i).

Another method to find the center of the imaged vortices is similar to the one we used in Chapter 4. After appropriate Fourier filtering, we take the highest point in the vortex disk as the center. The comparison of the data shows the two methods give almost identical results for the vortices that are normally shaped in the image. For the vortices that are connected to an impurity or split in the image because a jump of speed happened during the scan, this new method provides better information than the previous one.

With the vortex lattice information of each frame, the track of motion of each

vortex is revealed by identifying the vortex in the current frame closest to the i^{th} vortex in the previous frame. Each track contains the time series information of $(x(t), y(t))$ of a particular vortex from moving into till out of the field of view. These tracks and lattices are the acquired data for further analysis. The study of the statics and dynamics of the vortex lattice will be based on the information we extracted after analyzing them. In Sec. 5.4.1 and Sec. 5.4.2 I will discuss these studies respectively. In each section, I will include the study on the pure sample without introduced pinning centers and the study of the vortex matter around the pinning centers.

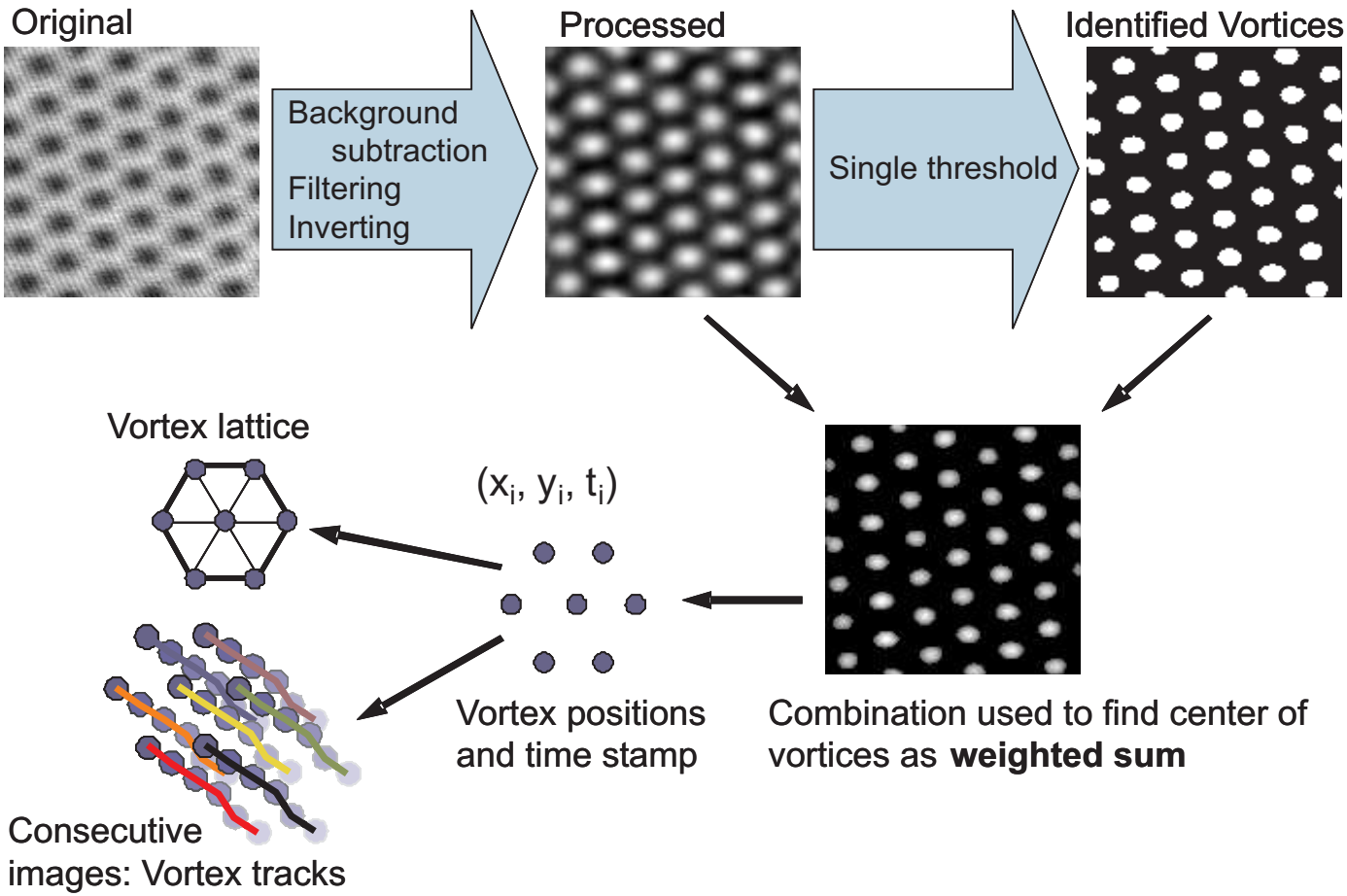

Figure 5.9: **Image Analysis Method.** STS images are processed through different image processing techniques. The center positions and capturing time of each vortex on every frame are recorded for final analysis.

5.4 Results

5.4.1 Statics

To calculate the displacement field within each frame, we first construct a perfect triangular lattice using the averaged lattice parameters, *i.e.* the angle and the lattice constant which can determine a primitive vector. The original lattice from the raw data contains distortions from two main sources. One is the natural displacement field caused by pinning centers in the sample and the other is the hysteresis of the STM scanner. The first distortion is mainly local and the second one is global. In order to remove the global distortions, we fit the original lattice to the perfect one by mean-square minimization of a polynomial transformation. Usually a second order transformation is good enough. The displacement at each point on the perfect lattice is then calculated by subtracting the perfect coordinates from the transformed coordinates of the original lattice using the parameters from the fit. The displacement field is finally resolved as $\mathbf{u}(\mathbf{r}_i^0)$, $\mathbf{r}_i^0$ is the position of the perfect lattice point. There is a third source of distortion that is worth mentioning here: the distortion result from vortex motion during the scan. We assume in this case the motion is uniform or at a very low frequency. The distortion is then global and can be removed by the transformation. After comparing the result with the data when the field is held constant, we conclude that this type of distortion is small because the speed is very low and at a low frequency as can be seen from the dynamic results (see Sec. 5.4.2).

We treat the vortices appearing within one frame of the movie, which actually

are acquired at different times, as captured in a snapshot like the images in a Bitter decoration experiment or a Lorentz imaging experiment [53]. This approximation is only possible because of the slow motion. Averages over displacement configurations in different frames are taken as a thermal average in the theory. This way we can overcome the limited size of the field of view and the number of vortices to take a statistical average. I also want to mention here that by holding the field and stopping the motion of vortices, we can acquire a snapshot of the static lattice. But this has limitations in the vortex number per image or the time of the experiment if we take multiple snapshots by turning on and off the decaying of the field. Future STMs with larger field-of-views and higher scan speeds maybe overcome this and image large number of vortices within one frame.

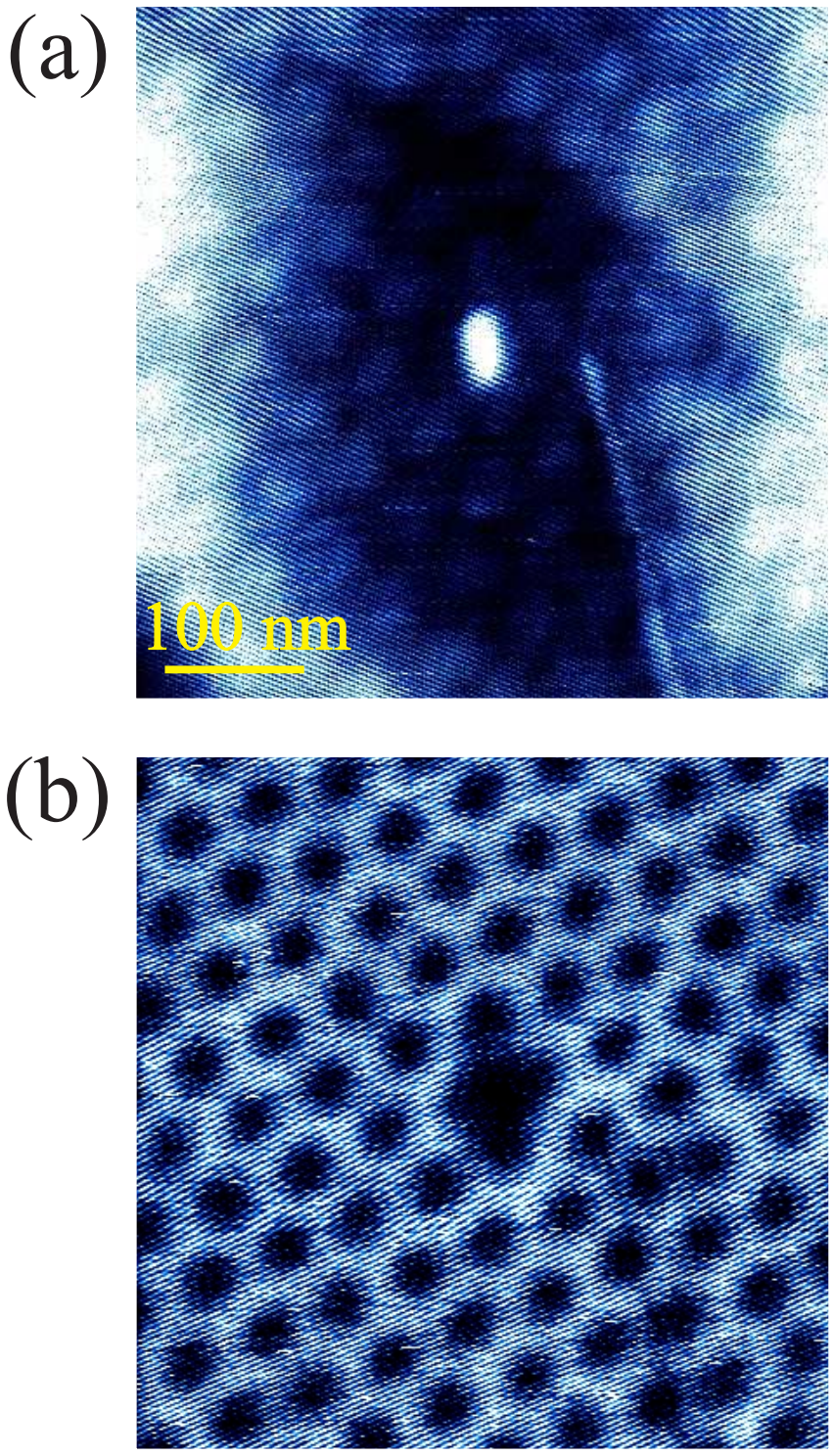

Figure 5.10: **Impurity and Vortices.** Topography image (a) shows the center impurity and a flat surface. Tunneling parameters $V = 100$ mV, $I = 0.1$ nA, $T = 4.2$ K. Magnetic field $B = 0.75$ T. (b) is one of the STS images with vortices to be processed. The impurity now is shown as a dark disk at the center surrounded by four vortices. Tunneling parameters $V = 3$ mV, $I = 0.1$ nA, $T = 4.2$ K. Magnetic field $B = 0.75$ T.

The sample we use for this study is a 2H-$NbSe_2$ crystal doped slightly with Fe (impurity concentration 200 ppm). As shown in Fig. 5.10 the images were taken around a Fe atom cluster with a diameter $\sim$ 20 nm (50 nm in the long direction). The sample is zero field cooled (ZFC). A 0.75 T magnetic field was initially applied then allowed to decay. The average number of vortices per frame is $\sim$ 87. 496 frames in total are recorded for the analysis. When processing the images, we subtracted the area close to the impurity with the averaged image to remove the contribution from the impurity to the DOS difference. After inverting and filtering, the centers of the vortices on each frame are measured. Fig. 5.11(a) shows the processed image and the raw data of the lattice structure. Using these data, I then removed the distortion due to the STM and calculated the perfect lattice and the displacement field. Part of the final image and lattice structure are shown in Fig. 5.11(b).

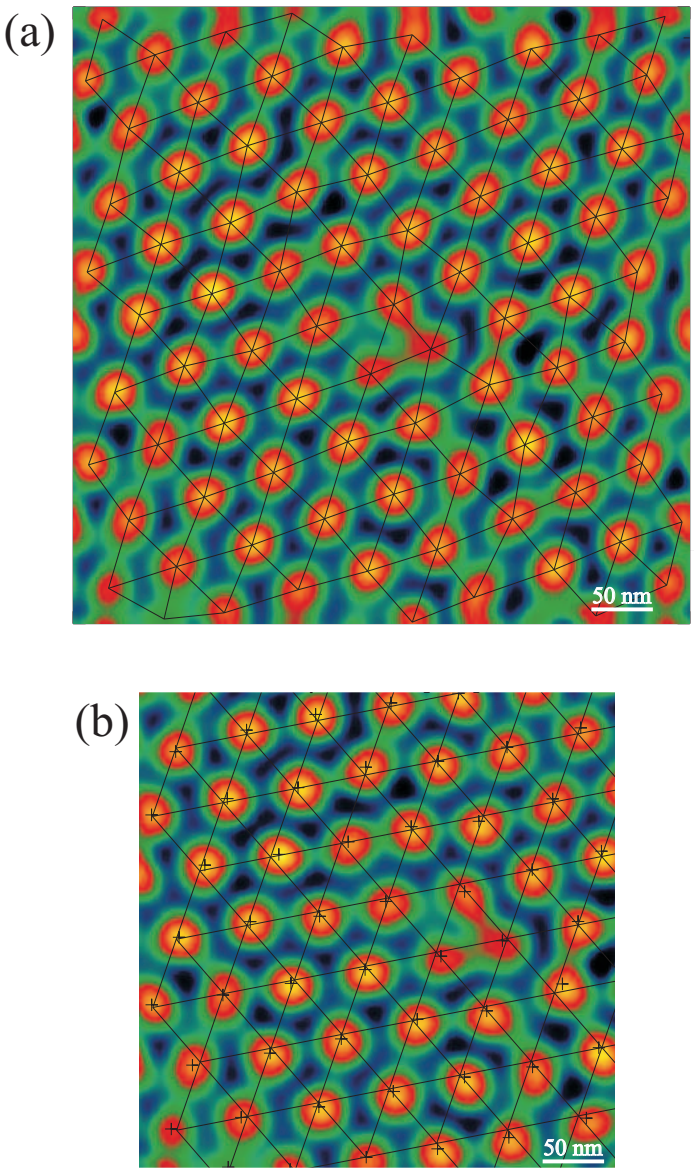

Figure 5.11: **Processed Images.** Processed image with the centers plotted as a lattice in (a). (b) shows part of the image with the global distortion removed. The perfect lattice is plotted with lattice points connected and the real lattice points are plotted as crosses to show the distortion. Both images are transformed from gray scale images. Red color means higher values in the inverted STS image; green means lower.

Finally the displacement correlator $B(r)$ and translational correlation function $C_k(r)$ are calculated and plotted in Fig. 5.12. The value $B(r)$ is much smaller than ξ^2 ($\xi^2/a_0^2 \approx 0.04$). According to the theory, this belongs to the Larkin regime. Our data show an initial increase until $r = 2a_0$ then an almost flat region from $2a_0$ to $5a_0$. After $r = 5a_0$ the growth of $B(r)$ becomes linearly increasing which agrees with the theoretical result of Eq. 5.10. In Fig. 5.12(a) a linear fit (red) from $5a_0$ to $12a_0$ shows

$$B(r)/a_0^2 = 0.00024r/a_0 + 0.0025. \tag{5.20}$$

According to Eq. 5.10, $B_{thermal} = 0.0025a_0^2$ and $\Delta/c^2 = 0.00024a_0$. Extrapolation indicates a Larkin length $R_c \approx 78a_0 \approx 4.7$ μm. The critical current can be estimated as $j_c = cF_c/B \approx 1.2 \times 10^6$ A/m^2 [2]. These results are consistent with the measurements from other experiments [74, 75]. The thermal part can also be compared with the theoretical estimation ((4.85) in [2] and [76]) which gives $B_{thermal} = 0.00004a_0^2$. Our result is much larger, I believe this indicates other types of uncorrelated noise are included such as the error from detecting the center by the algorithm. As I mentioned before, the short range correlation with $r < 5a_0$ doesn't follow this formula in the plot. I believe this is because we are measuring the function around the impurity. The large distortions from the vortices close to the impurity contribute more to the short range values compared to a region with no impurity. Further studies from regions away from impurities would be desirable to verify this argument. After $12a_0$ most of the contributions to $B(r)$ comes from

the vortices at the edges of the image and the error becomes intolerable. There are two reasons for the volatile behavior: first vortices at edges may be only partially recorded by our STM and the center coordinate values can be affected by the Fourier filtering; second, the number of vortices taking part in the average drops sharply when r is almost the image size. Thus increasing the size of the field of view is crucial for this technique to observe the growth of $B(r)$ at longer range. Nevertheless, our data show linear growth at $r > 5a_0$ which is promising for further measurements using improved setup.

Another interesting result is the translational correlation function $C_k(r)$. As shown in Fig. 5.12(b) it fits well with the Gaussian approximation but with a new factor $C_G(r) \sim e^{-G^2B(r)/2.5}$ instead of $e^{-G^2B(r)/2}$. The Gaussian approximation in theory is a convenient choice for the calculation. There is no theory currently available to explain this factor. I hope further experiments can give us more insights in the future.

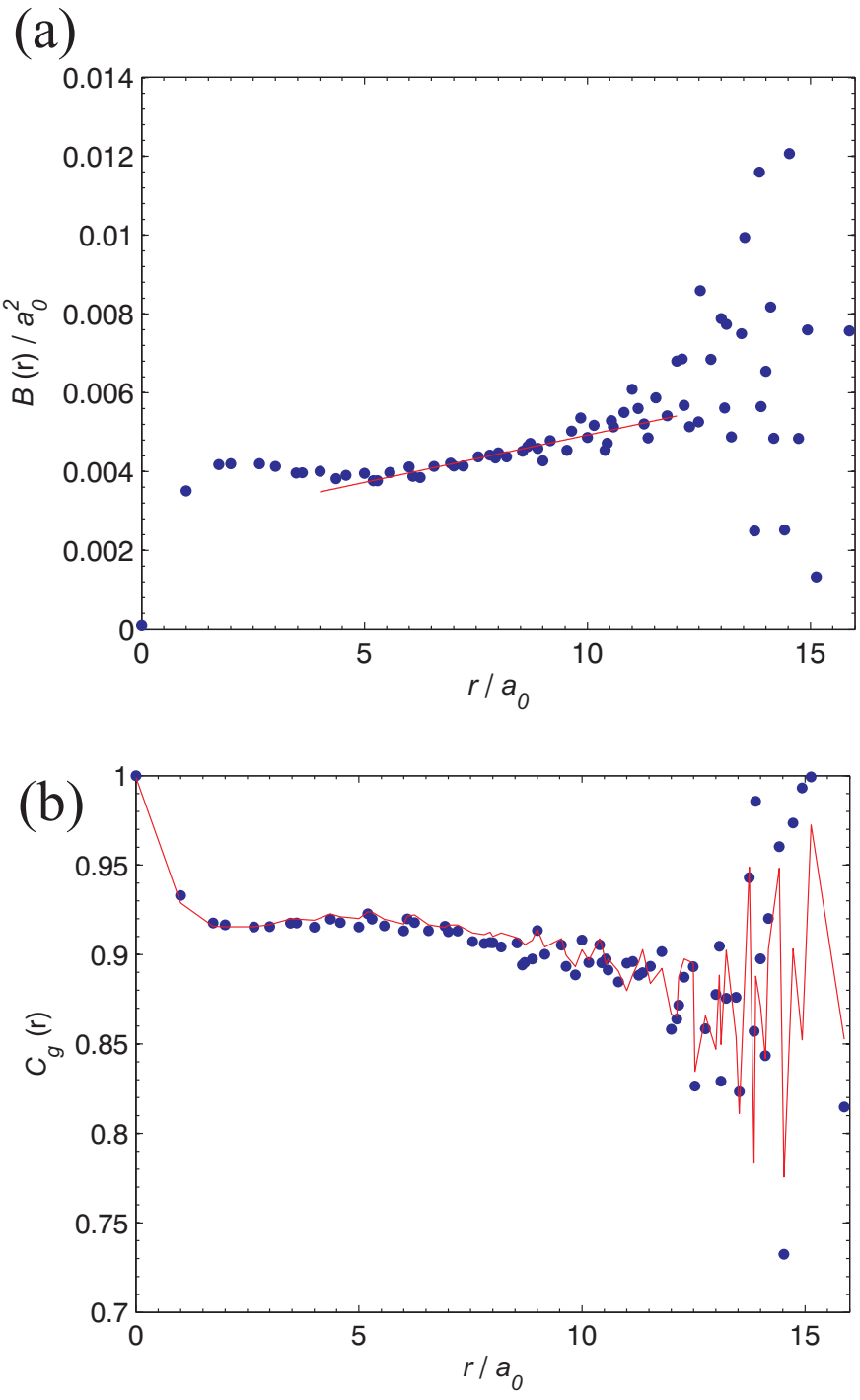

Figure 5.12: **Static Results.** (a) shows the relative displacement correlation function $B(r)$. The red line shows the fitting of the linear section from $5a_0$ to $12a_0$ (Eq. 5.20). (b) shows the positional correlation function $C_G(r)$ (Eq. 5.5). The red line plots the Gaussian approximation result $e^{-G^2B(r)/2.5}$.

5.4.2 Dynamics

As mentioned in Sec. 5.2, slow dynamic behavior of the vortex lattice is much less well studied in this slow motion regime. In this section, I will use data from the pristine sample without introduced impurities. I chose this because we have the longest observation time on this sample and the motion is extremely slow.

Fig. 5.13 (a) shows the first image of the movie series. The gray scale image is Fourier filtered. On top of it, the tracks of four vortices $(x(t), y(t))$ are displayed as examples with a color code representing time. In this run, the sample is zero field cooled (ZFC) and the magnetic field was then raised to 0.5 T. The data was taken 10 days after the initial increase so the magnetic relaxation was complete (the relaxation time constant was shown to be $\sim$ 5 min for $NbSe_2$ in [72]). The total time for this continuous acquisition is 6 days 17 hours 35 minutes and 40 seconds. It contains 2560 frames. This is so far the longest one we have tried. The average number of vortices per frame is 39. The averaged lattice constance is 68.3 nm while the calculation shows $a = \sqrt{2\Phi_0/\sqrt{3}B} = 68$ nm. After image analysis, the velocities are extracted from the track information by $(v_x(t), v_y(t)) = (\frac{\Delta x(t)}{\Delta t}, \frac{\Delta y(t)}{\Delta t})$. The arithmetic average speed of all the vortices at all times is 2.28 pm/s. Thus the induced electric field $E = vB = 1.14 \times 10^{-12}\ Vm^{-1}$. This is 8 orders of magnitude smaller than the commonly used voltage criterion defining the critical current density j_c. I believe this very slow speed obviously puts the motion in the flux creep region. To the best of our knowledge, this is the slowest motion ever measured or imaged. The closest previous record was the work by Troyanovski *et. al.* [49] where the speed

was ~ 1 nm/s. However, there was no explanation of the source of motion in their paper. Since they started imaging only 20 min after the field change, it is highly possible it was still in the relaxation regime of the field. The total recording time was only 30 min. It is therefore unlikely to capture the feature of creep motion. Our data contain much richer information about the creep regime in the moving glass system.

The data in this section has also been reported by my colleague Jonghee Lee in his Ph.D. thesis [16]. Here I present my analysis based on Bragg glass theory and collective creep model.

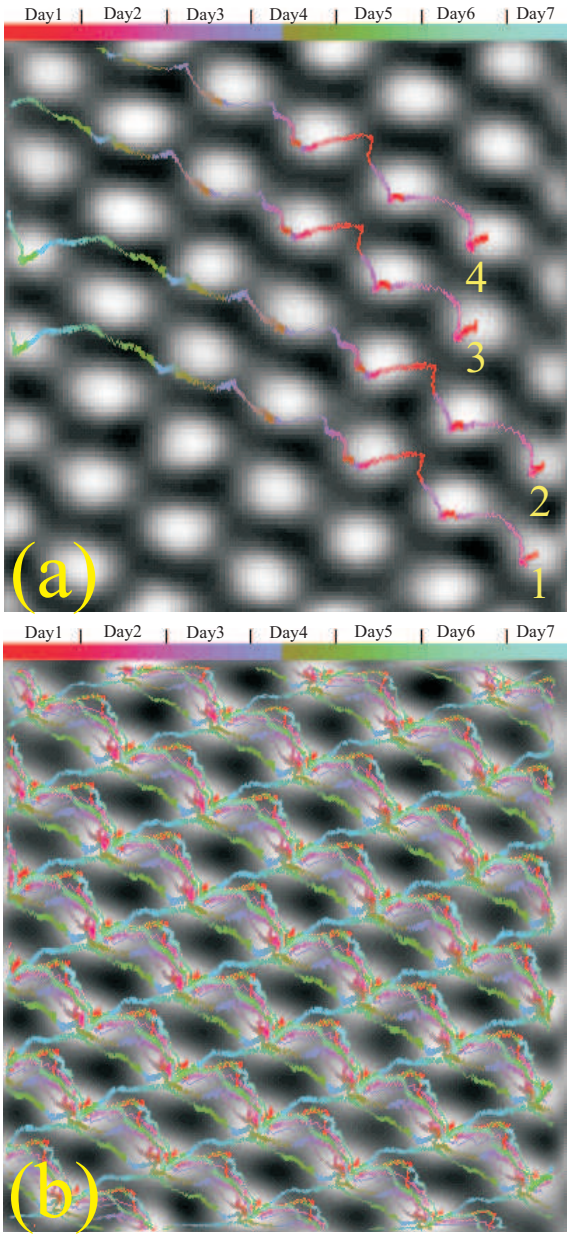

Figure 5.13: **Tracks of Vortices.** (a) shows the tracks of 4 vortices on the background gray-scaled image of the first frame in the series. (b) complies all the tracks together with a color code of time. The time begins at red and ends at green from day 1 to day 7 as indicated by the color bar in (a) and (b).

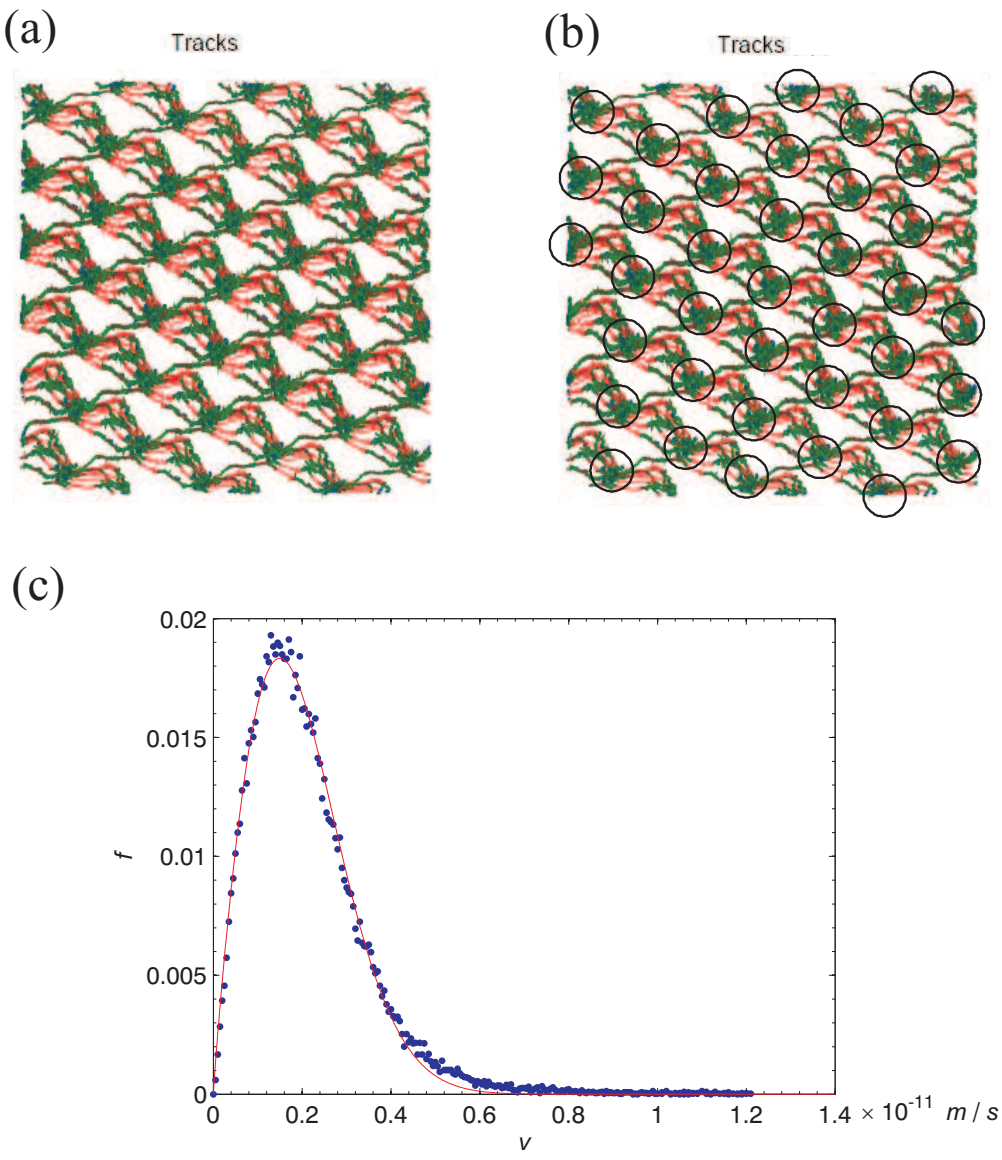

Figure 5.14: **Tracks Color-coded with Velocity.** (a) shows the track of all the vortices with a color code of velocity. The lower end of the velocity is coded green and the higher end red. In (b) the positions where vortices spend more time are circled. (c) shows the distribution of all the velocities. The red curve is the fitting result $f = av^{c-1}e^{-bv^c}$ with $a = 0.165$, $b = 17.73$, $c = 1.91$. Here f is the probability density and v is the absolute value of velocity (see Eq. 5.21 and the text below).

In Fig. 5.14(a) all the tracks of the vortices are compiled together with a color code of time to illustrate the whole creep process. These tracks provided unique characteristics of the nature of a creeping Bragg glass phase as we described in Sec. 5.2. First, we notice that the vortices move collectively and the order is preserved. In this case the assumption (I) of the collective pinning theory is confirmed. Second, the vortices do not always move along one direction as suggested by the TAFF model. The random meandering along the route is obvious. Third, there are certain points the vortices are more likely to visit and stay longer, as shown by the circles in Fig. 5.14(b). Those can be explained as the configuration points with deeper potential well (or "major minima" versus "minor minima" as in [71]) in the energy landscape. This is consistent with the picture of the creep motion in which the potential U is not uniform but varies from configuration to configuration. Fourth, unlike the moving glass at high velocity [55], the vortices do not follow each other exactly along the same channel. Since the average velocity remains almost constant as shown in the speed vs time plot in Fig. 5.15, and the driving force should be very small to have such a small response, it is reasonable to assume that the driving force can be considered constant throughout the process. Thus the velocity distribution in Eq. 5.18 for a constant force can be applied here.

Fig. 5.14(c) shows the distribution of velocities of all the vortices and the fitting (red) function $f = av_s^{c-1}e^{-bv_s^c}$ with $v_s = v \times 10^{11}$ in the plot. I obtained parameters: $a = 0.165$, $b = 17.73$, $c = 1.91$. If we assume that the displacement of each motion is constant or the variations are small, by an Arrhenius law we have $v = v_0 e^{-\beta U}$. A simple extension of the 1D vortex string result of Eq. 5.18 to our

case reads,

$$f(v) = \frac{1}{\beta U_c}\frac{R}{R_c}\frac{1}{v_0}\left(\frac{v}{v_0}\right)^{\frac{1}{\beta U_c}-1}\exp\left(-\frac{R}{R_c}\left(\frac{v}{v_0}\right)^{\frac{1}{\beta U_c}}\right). \tag{5.21}$$

Here R is the bundle size, R_c is the Larkin length which is the size of the smallest bundle movable by the force. In the theory [70], U_c is the minimum energy barrier between neighboring metastable positions of a pinned bundle with a Larkin length R_c. Our fitting of parameter c gives a characteristic energy $U_c = 0.52k_BT$ ($T =$ 4.2 K). However, the parameter b/a indicates $U_c = 107.5k_BT$ ($\sim$ 430 K). Typical experimental values for U_c are of the order of 10^2 to 10^3 K (p1151 in [2], [77]). In [49] using the collective creep model, a $U_c \sim 48$ K was deduced for $NbSe_2$.

The conflicting results shows the distribution model can not fully explain our data. Models for 2D bundle motion are required to explicitly examine the slow creep motion we observed. The extension from the 1D to 2D motion is nontrivial as noted in [70]. The scaling procedure to reproduce the mean velocity formula of the collective creep model will be different and hence the interpretation of the characteristic energy U_c. I hope further theoretical studies can clarify this issue. Nevertheless, I believe that this result shows that fine structure of the energy landscape does exist in this system and is inconsistent with the picture of uniform potential wells from TAFF theory.

On the other hand, our result showed the Weibull-type distribution of the velocity, if integrated over size R as in [70], will result in an exponential form of the global distribution density of U. It is this exponential distribution that leads to the nonlinear characteristics in the collective creep model. To the best of my knowledge

our experiment is the first microscopic measurement of the distribution of the creep motion of a single bundle.

Other than the statistical properties, the velocity field also reveals the spatial distribution of the energy landscape. Although the motion has certain randomness, the energy landscape itself is rather ordered as can be seen from the track compilation using a color code of speed. Since the speed is monotonically related to the potential height, this plot actually shows the energy landscape $U(\mathbf{r}, t)$ that is probed by the creep motion process. Note that ($\mathbf{r}$,t) here denote a configuration that is detected at time t with one vortex at $\mathbf{r}$. U is definitely a function of magnetic field $\mathbf{B}$ and current $\mathbf{j}$ as posited in the collective creep model. Time t here can be viewed as parameterized by these two quantities $t(\mathbf{B}, \mathbf{j})$. If we assume that these two quantities do not vary enough to have an observable consequence on U, then the plot can be viewed as the spatial distribution of the landscape with an exponential scale since $v \propto e^{\beta U}$. Certain features are noticeable in this plot. The periodicity of the distribution coincides with the periodicity of the lattice. This is quite apparent since the elastic and disorder energy would not change if the vortex bundle move to a symmetric position. Also, this is assumed in the TAFF and the collective creep theory. Unlike in the TAFF model, we did not observe the washboard frequency which is $f_w = \langle v \rangle / a_0$ as in [49]. The reason is that even the landscape has a spatial modulation a_0, and the transition from one major minimum to another is rather random in the very slow creep region. Therefore, the time of the transition depends on the random path instead of a constant t_w which would contribute to a peak $f_w = 1/t_w$ in the Fourier transform of the longitudinal velocity vs. time plot

in Fig. 5.15. The physical picture of creep is far from the tilted washboard model in TAFF because the rich 2D energy landscape with many metastable states give rise to the random hopping through the available states much like a water droplet moving down a slightly tilted surface. These metastable states and the creep motion are signatures of the Bragg glass system.

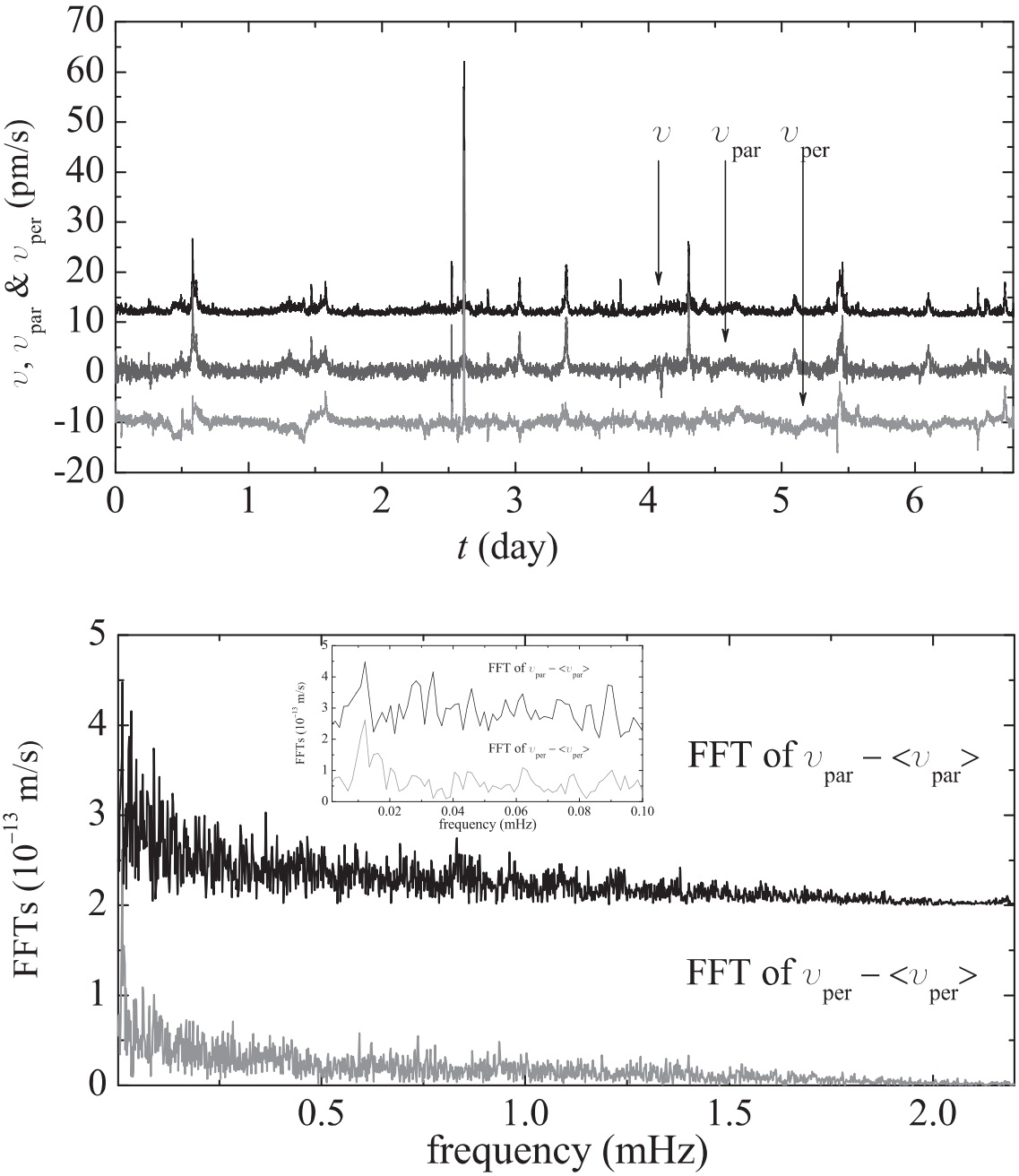

Figure 5.15: **Velocities.** Velocities parallel and perpendicular to the moving direction are plotted as a function of time in (a) and frequency in (b). No prominent peak found in (b) at the washboard frequency $f_w = \langle v \rangle / a_0 = 2.28$ (pm/s)/68.3 (nm) ~ 0.03 mHz. The insert in (b) shows the data around 0.03 mHz.

In conclusion, we directly imaged the creep motion of the Bragg glass by LTSTM. The results confirmed the collective creep picture with an energy landscape by direct evidence for the first time. Our data also revealed features of the energy landscape in detail, providing a new incentive and input for theoretical modeling to go beyond the $v-f$ characteristics and study the nature of the moving glass system.

5.4.3 Imaging the Interaction with Disorder

In the theoretical modeling, the quenched disorder in the Bragg glass is simplified as point impurities with Gaussian correlations. This mathematical convenience does not cost much in determining the general properties of the vortex system as the models could predict much of the behavior of the statics and dynamics. However, the disorder and the details of the interaction cannot be ignored. For example, one has to refer to strong pinning theory to address the problem with extended or correlated disorder such as twin boundaries [2].

As a powerful microscopic instrument, STM is an undisputable choice to look into the details of the interaction. This is based on the advantage of the LTSTM system which uniquely images the core of the vortex and thus has a much higher spatial resolution than other probes. Its strength was first demonstrated by Troyanovski *et al.* [49] on the plastic motion of the vortex with strong pinning centers. Here I show some of the work we have carried out on the direct imaging of interaction of a moving vortex system with a variety of local impurities.

The first impurity is the Fe atom clusters as we discussed in Sec. 5.4.1. Fig. 5.16

shows 4 of the consecutive frames of the movie. As pointed out by the short arrow, one of the vortices was as if pulling away from the impurity at the center of the image while the majority of them remain in position relative to the impurity and the structural defect indicated by the long arrows. Also noticeable is that the vortices along the line of the structural defect are distorted toward it.

The second impurity is the pit we created in Ch. 4. The interaction of the vortex system with this impurity is illustrated in Fig. 5.17. The 4 consecutive images are Fourier filtered and inverted so the vortices are now displayed as white disks. The arrow at the top points out the interface of a sliding plane. The slip happened at (c) along the lattice axes. It is interesting to notice that the bundle at the upper right corner slid as a whole. This is consistent with the moving glass theory in which vortex system moves bundle by bundle [55]. To the best of our knowledge this is the first time the abrupt sliding interface has been directly imaged.

The third type of defect is the extended structural defects such as folding layers or twin boundaries we found on the surface that can induce more distortion in the lattice structure than the two weak pinning centers I mentioned above. In Fig. 5.18 (a) the topographic image shows structural defects all across the field of view. Fig. 5.18 (b) to (c) are 3 consecutive frames of the movie showing the vortices moving across the area. The yellow arrow points to an area where the distortion is developing in frame (c).

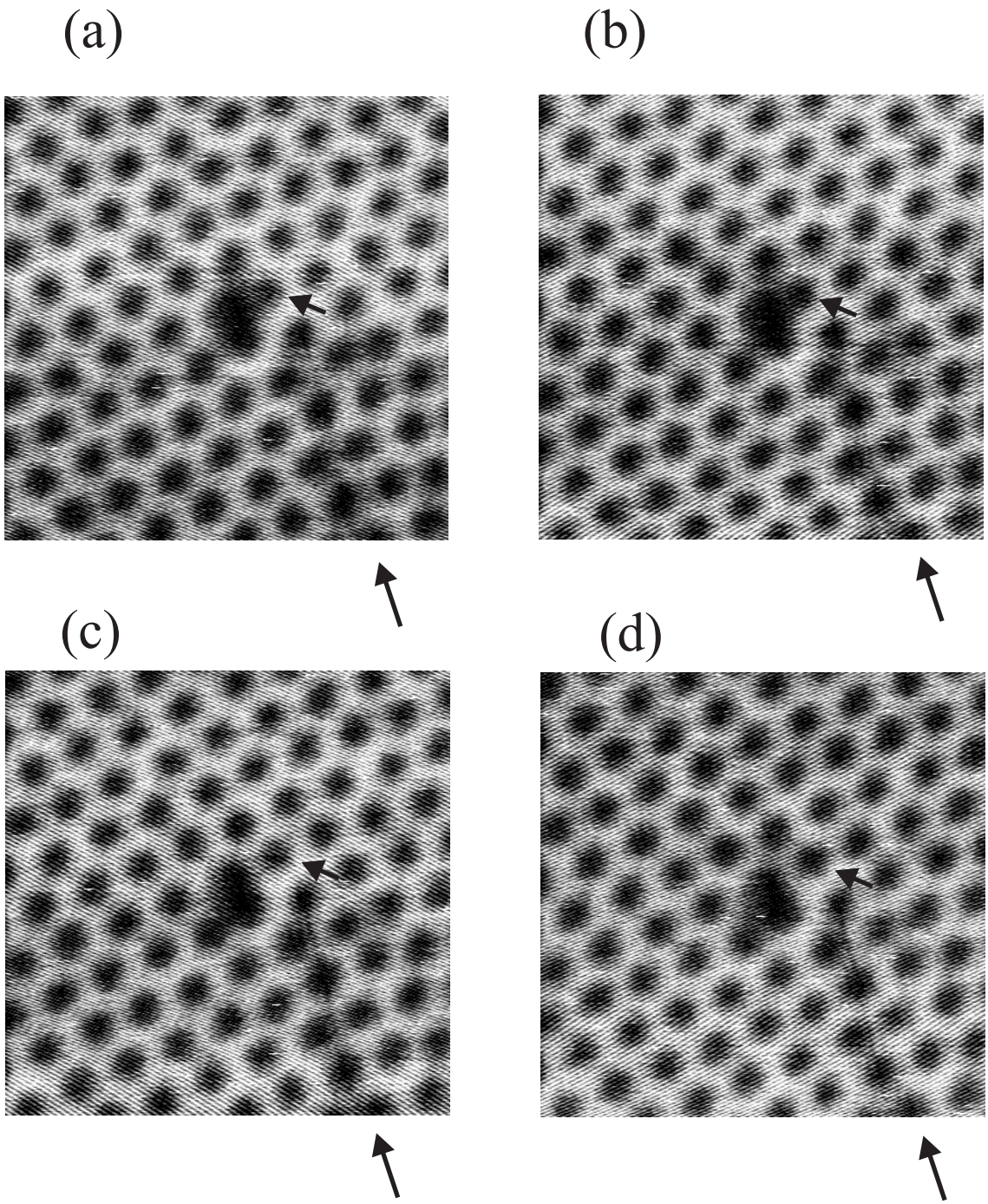

Figure 5.16: **Interaction With Impurity (I).** (a)-(d) are four consecutive frames from a movie series of vortex motion around an Fe impurity at the center. Arrows points to a moving vortex close to the impurity and the stationary vortices. Image size 500 nm $\times$ 500 nm.

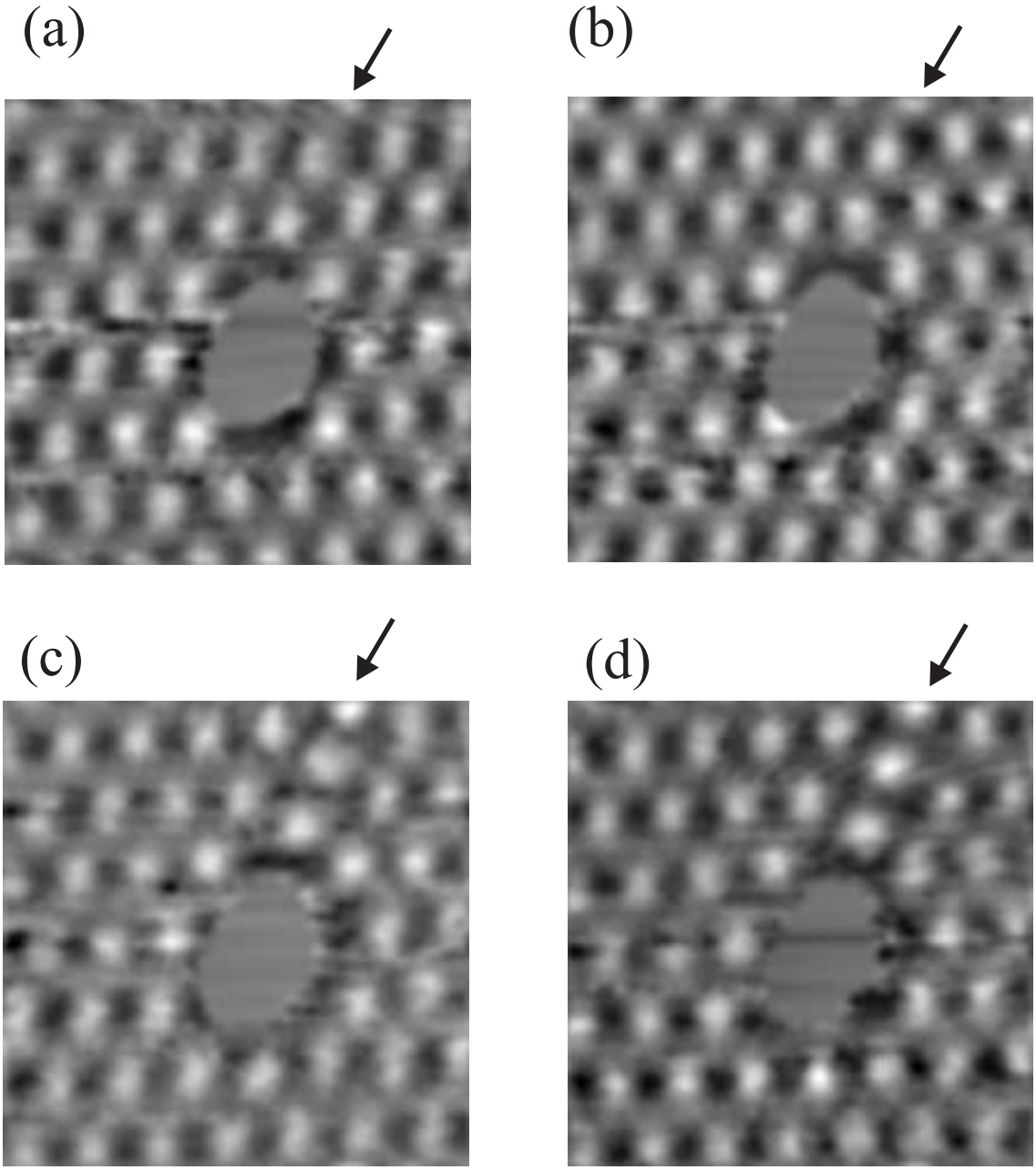

Figure 5.17: **Interaction With Impurity (II).** (a)-(d) are four consecutive frames from a movie series of vortex motion around a structure defect at the center. Arrows points to a sliding surface. Image size 400 nm × 400 nm.

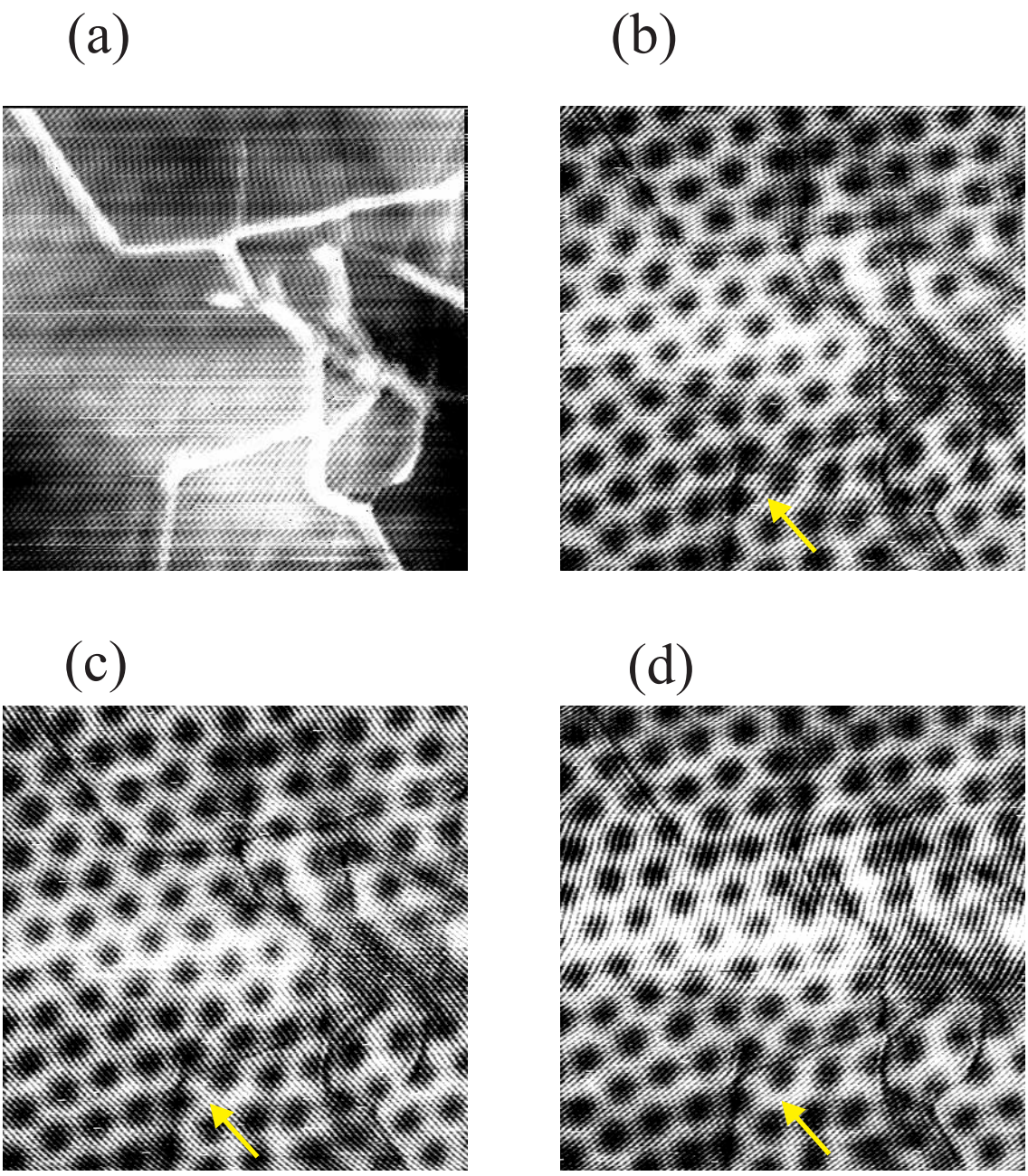

Figure 5.18: **Interaction With Impurity (III).** (a) shows the topography image of the area. (b)-(d) are 3 consecutive frames from a movie series of vortex motion around extended defects on the surface. Arrows point to an area where the distortion is developing. Image size 500 nm × 500 nm.

As illustrated above, the interaction between the vortex system and the disorder can be directly imaged in detail with great precision. For studies of the microscopic theory about vortex interactions with the landscape, including defects, this technique provides a unique chance to directly visualize the force field and the potential profile. Also it is useful in checking some of the assumptions in the elastic model as I discussed in Sec. 5.2. Here I leave the further discussion of this work to later publications.

5.5 Conclusion and Future Work

In this Chapter I demonstrated the use of LTSTM as a new weapon to attack the problems in the vortex system. It has many advantages over other probes in resolution and applicable magnetic field strength. The primary limitation is the field of view in our current system. The study of the statics and dynamics of the vortex matter in the low-T_c, type II superconductor $NbSe_2$ provides for the first time direct evidence of the Bragg glass phase in the creep motion mode. Our most important result is the revelation of the energy landscape of the dynamic creep phase of the moving glass. The evidence strongly supports a collective creep picture with a Weibull-type distribution of the potential heights in the landscape for a single bundle. Also the spatial distribution of the landscape is directly mapped out in the field of view. Further application of this technique includes a study of the interaction microscopically which will benefit more detailed modeling about the interaction and the macroscopic model.

There are many extension of the current work possible. One of the most interesting measurements would be to visualize the melting of the Bragg glass phase to the disordered solid through the peak effect line $H_p(T)$ in the phase space. Also the creep motion in the disordered phase could be compared with the current study. Both of these require a higher magnetic field than we can currently provide. So further improvement of the instrument in the applicable field strength is crucial to advance our studies in these areas. The future design of the STM system should be geared toward continuously enlarging the field of view and increasing the scan speed to improve both the static and dynamic measurements.

Another important challenge is to establish controllable driving sources from magnetic fields or applied currents. A direct measurement of the field profile in the current setup would make possible the calculation of the current distribution in the sample. To meet these challenges an extension or partial modification of our LTSTM system is required. On the other hand, a rather straightforward extension of our work would be to study the Bragg glass phase in HTSC samples.

Bibliography

[1] T. Giamarchi and S. Bhattacharya, cond-mat/0111052 (2002).

[2] G. Blatter, M. V. Feigel'man, V. B. Geshkenbein, A. I. Larkin, and V. M. Vinokur, Rev. Mod. Phys. **66**, 1125 (1994).

[3] R. Wiesendanger, *Scanning Probe Microscopy and Spectroscopy: Methods and Application*, Cambridge University Press, 1st edition, 1994.

[4] G. Binnig, H. Rohrer, C. Gerber, and E. Weibel, Phys. Rev. Lett. **50**, 120 (1983).

[5] J. Bardeen, Phys. Rev. Lett. **6**, 57 (1961).

[6] G. Binnig and H. Rohrer, Reviews of Modern Physics **59**, 615 (1987).

[7] M. H. Cohen, L. M. Falicov, and J. C. Phillips, Phys. Rev. Lett. **8**, 316 (1962).

[8] G. D. Mahan, *Many-Particle Physics*, Plenum Press, 2st edition, 1990.

[9] A. L. Fetter and J. D. Walecka, *Quantum Theory of Many Particle Systems*, McGraw-Hill, 1st edition, 1971.

[10] J. Tersoff and D. R. Hamann, Phys. Rev. Lett. **50**, 1998 (1983).

[11] J. Tersoff and D. R. Hamann, Phys. Rev. B **31**, 805 (1985).

[12] L. Hedin and S. Lundqvist, *Solid State Physics: Advanced in Research and Applications*, volume 23, Academic, New York, 1969.

[13] B. D. Josephson, *Superconductivity*, volume 1, Dekker, New York, 1969.

[14] N. Garcia, IBM J. Res. Develop. **30** (1986).

[15] J. H. Coombs and J. B. Pethica, IBM J. Res. Develop. **30** (1986).

[16] J. Lee, *Low Temperature Scanning Tunneling Microcope Development: Investigations of Au(111) and Ultra-low Vortex Dynamics of $NbSe_2$*, PhD thesis, University of Maryland, College Park, 2007.

[17] S. H. Pan, International Patent Publication Number WO 93/19494 (International Bureau, World Intellectual Property Organization), 1993.

[18] S. H. Pan, E. W. Hudson, and J. C. Davis, Rev. Sci. Instrum. **70**, 1459 (1999).

[19] R. E. Peierls, *Quantum Theory of Solids*, Oxford University Press, New York/London, 1955.

[20] G. Grüner, Rev. Mod. Phys. **60**, 1129 (1988).

[21] J. A. Wilson, F. J. Di Salvo, and S. Mahajan, Adv. Phys. **24**, 117 (1975).

[22] M. D. Johannes, I. I. Mazin, and C. A. Howells, Phys. Rev. B **73**, 205102 (2006).

[23] L. A. Angurel, F. Amin, M. Polichetti, J. Aarts, and P. H. Kes, Phys. Rev. B **56**, 3425 (1997).

[24] U. Essmanna and H. Träuble, Phys. Lett. A **24**, 526 (1967).

[25] K. Harada et al., Nature **360**, 51 (1992).

[26] P. E. Goa et al., Supercond. Sci. Technol. **14**, 729 (2001).

[27] S. Ohshima, K. Tanabe, T. Morishita, and M. Tonouchi, *Vortex Electronics and SQUIDs*, chapter Observation of Vortices, pages 53–102, Springer Berlin, Heidelberg, 2003.

[28] G. Grüner, *Density Waves in Solids*, Addison-Wesley, Reading, MA, 1994.

[29] R. V. Coleman et al., Adv. Phys. **37**, 559 (1988).

[30] B. Koslowski, W. Xu, B. Blackford, and M. H. Jericho, Phys. Rev. B **54**, 11706 (1996).

[31] N. Ramšak et al., Phys. Rev. B **60**, 4513 (1999).

[32] F. Komori, T. Iwaki, K. Hattori, O. Shiino, and T. Hasegawa, J. Phys. Soc. Jpn. **66**, 298 (1997).

[33] B. Giambattista, C. G. Slough, W. W. McNairy, and R. V. Coleman, Phys. Rev. B **41**, 10082 (1990).

[34] J. Zhang, J. Liu, J. L. Huang, P. Kim, and C. M. Lieber, Science **274**, 757 (1996).

[35] K. T. Andrews, L. Guessous, S. Nassar, S. V. Putta, and M. Shillor, J. Appl. Math. **2006**, 1 (2006).

[36] A. Kikuchi and S. Tsuneyuki, Surf. Sci. **409**, 458 (1998).

[37] B. E. Brown and D. J. Beerntsen, Acta Cryst. **18**, 31 (1965).

[38] F. Kadijk and F. Jellinek, J. Less-Common Metals **23**, 437 (1971).

[39] Y. Z. Li, L. Vazquez, R. Piner, R. P. Andres, and R. Reifenberger, Appl. Phys. Lett. **54**, 1424 (1989).

[40] F. Flores, P. M. Echenique, and R. H. Ritchie, Phys. Rev. B **34**, 2899 (1986).

[41] S. Kondo, S. Heike, M. Lutwyche, and Y. Wada, J. App. Phys. **78**, 155 (1995).

[42] R. E. Thomson, B. Burk, A. Zettl, and J. Clarke, Phys. Rev. B **49**, 16899 (1994).

[43] W. L. McMillan, Phys. Rev. B **16**, 643 (1977).

[44] R. V. Lapshin, Rev. Sci. Instrum. **69**, 3268 (1998).

[45] N. V. Smith, S. D. Kevan, and F. J. Di Salvo, J. Phys. C **18**, 3175 (1985).

[46] W. L. McMillan, Phys. Rev. B **14**, 1496 (1976).

[47] J. A. Wilson, Phys. Rev. B **17**, 3880 (1978).

[48] A. A. Abrikosov, Sov. Phys. JETP. **5**, 1174 (1957).

[49] A. M. Troyanovski, J. Aarts, and P. H. Kes, Nature **399**, 665 (1999).

[50] E. H. Brandt, Phys. Rev. B **34**, 6514 (1986).

[51] M. Tinkham, *Introduction to Superconductivity*, McGraw-Hill, New York, 2nd edition, 1996.

[52] J. G. Bednorz and K. A. Müller, Z. Physik, B **64**, 189 (1986).

[53] Y. Fasano and M. Menghini, Supercond. Sci. Technol. **21**, 023001 (2008).

[54] T. Klein et al., Nature **413**, 404 (2001).

[55] T. Giamarchi and P. Le Doussal, cond-mat 9705096 (1997).

[56] Larkin, A. I., Sov. Phys. JETP **31** (1970).

[57] A. I. Larkin and Y. N. Ovchinnikov, J. Low Temp. Phys. **34**, 409 (1979).

[58] T. Giamarchi and P. Le Doussal, Phys. Rev. Lett. **72**, 1530 (1994).

[59] T. Giamarchi and P. Le Doussal, Phys. Rev. B **52**, 1242 (1995).

[60] T. Giamarchi and P. Le Doussal, Phys. Rev. B **55**, 6577 (1997).

[61] Y. Paltiel et al., Phys. Rev. Lett. **85**, 3712 (2000).

[62] M. Menghini, Y. Fasano, and F. de La Cruz, Phys. Rev. B **65**, 064510 (2002).

[63] P. Chauve, T. Giamarchi, and P. LeDoussal, Europhys. Lett. **44**, 110 (1998).

[64] P. Chauve, T. Giamarchi, and P. Le Doussal, Phys. Rev. B **62**, 6241 (2000).

[65] P. W. Anderson and Y. B. Kim, Rev. Mod. Phys. **36**, 39 (1964).

[66] M. V. Feigel'Man, V. B. Geshkenbein, A. I. Larkin, and V. M. Vinokur, Phys. Rev. Lett. **63**, 2303 (1989).

[67] D. T. Fuchs et al., Phys. Rev. Lett. **80**, 4971 (1998).

[68] C. J. van der Beek et al., cond-mat/9912282 (1999).

[69] T. Nattermann and S. Scheidl, Adv. Phys. **49**, 607 (2000).

[70] V. M. Vinokur, M. Cristina Marchetti, and L.-W. Chen, Phys. Rev. Lett. **77**, 1845 (1996).

[71] L. Balents, J.-P. Bouchaud, and M. Mézard, Journal de Physique I **6**, 1007 (1996).

[72] F. Pardo, F. de la Cruz, P. L. Gammel, E. Bucher, and D. J. Bishop, Nature **396**, 348 (1998).

[73] H. F. Hess, R. B. Robinson, R. C. Dynes, J. M. Valles, and J. V. Waszczak, Phys. Rev. Lett. **62**, 214 (1989).

[74] L. A. Angurel, F. Amin, M. Polichetti, J. Aarts, and P. H. Kes, Phys. Rev. B **56**, 3425 (1997).

[75] S. Bhattacharya and M. J. Higgins, Phys. Rev. Lett. **70**, 2617 (1993).

[76] A. Houghton, R. A. Pelcovits, and A. Sudbø, Phys. Rev. B **42**, 906 (1990).

[77] Y. Yeshurun, A. P. Malozemoff, and A. Shaulov, Rev. Mod. Phys. **68**, 911 (1996).